MESSENGER Investigations of the Plasma Environment at Mercury

by

Jimmie M. Raines

A dissertation submitted in partial fulfillment
of the requirements for the degree of
Doctor of Philosophy
(Atmospheric, Oceanic and Space Sciences)
in The University of Michigan
2013

Doctoral Committee:

Professor Thomas H. Zurbuchen, Co-Chair
Professor James A. Slavin, Co-Chair
Professor Mark Kushner
Associate Professor Michael W. Liemohn

ACKNOWLEDGEMENTS

I want to thank Mark Kushner and Mike Liemohn for taking the time to serve on my committee.

I am grateful to the Solar and Heliospheric Group members (past and present). You have been an excellent group of people with which to work. In particular, I want to thank Jon Thomas for sorting out the mess of FIPS processing code and making an efficient reliable tool. Thanks to Mark Stakhiv for help with FIPS engineering and some occasional distractions. Jon and Mark helped me focus on research. Thanks to Shannon Curry for her support, especially on big days. I want to thank to Sue Lepri for always making time to talk. That really helped. I am very grateful to Gina DiBraccio and Julie Feldt. Without them, I probably would not have studied well enough to pass the qualifying exams. Gina continues to improve my understanding of magnetospheres through our discussions as well as being a good friend. Finally, I am very grateful to Dan Gershman for adding to my understanding of plasma instruments and making me think of things that did not occur to me, as well as being an excellent sounding board and my ardent supporter.

Without the support of these next people, I really would not have done this:

I am very grateful to Jim Slavin for very patiently teaching me magnetospheric physics and really spending time advising me, even before he came to Michigan. His constant encouragement kept going. I am very grateful to Thomas Zurbuchen who taught me about the solar wind, plasma instruments and data analysis. He trusted me to do things that I didn't know I could do and gave me credit when I did them. He showed me that pushing hard – while sometimes pretty uncomfortable – can lead to a very satisfying sense of accomplishment. Thanks to my kids, Connor and Spencer, for reminding me how cool it is to work with NASA studying stuff in space and for understanding when I really couldn't give them the attention they deserved. I want to thank my mother-in-law Judy, who really helped out with things at home so that I could worry less about neglecting responsibilities there while working long hours. I am very grateful to my mom, Shelby, for believing in me from the start and making me think I could do anything.

Finally, I am exceptionally grateful to my wife, Stacey, who was essential to this effort. She helped me keep perspective when things didn't go so well, and reminded me to take time to relax sometimes. She picked up more of the load at home, which at times was basically the entire load. She even did some typing. Most importantly, Stacey encouraged me to take the plunge into graduate school (again!) and supported me in yet another career change.

TABLE OF CONTENTS

LIST OF FIGURES

LIST OF TABLES

LIST OF APPENDICES

ABSTRACT

We report on the first observations of plasma ions at Mercury, from the Fast Imaging Plasma Spectrometer (FIPS). These observations were made by the MESSENGER spacecraft during two flybys of Mercury and while in orbit from March 2011 through May 2012. We found: 1) Bulk plasma ion measurements confirm that Mercury's magnetosphere is morphologically similar to Earth: There is hot, dense plasma in the magnetosheath. Plasma ions are concentrated at the cusps and in the central plasma sheet, where solar wind protons and alpha particles usually dominate and with densities and temperatures consistent with expectations from Earth. 2) Planetary ions are distributed throughout Mercury's magnetosphere, confirming the exosphere as a source of magnetospheric ions. These ions show some density enhancements in common with their parent neutral populations, particularly in the cusp and near the dawn equator. He+ are distributed more uniformly than other planetary ions, which may result from substantially different source regions or processes. Planetary ions have much larger *e*-folding heights than neutrals across the dayside, indicating significant influence from magnetospheric electric and magnetic fields. 3) These studies have shed light on the dynamics of planetary ions in Mercury's magnetosphere, the first step in understanding their role in the system. First, the asymmetric enhancement of large-gyroradius Na^+ ions

in the pre-midnight central plasma sheet may indicate non-adiabatic motion within this region and in transit to it. This behavior could have wide-reaching implications in the surface-exosphere-magnetosphere system. In particular, non-adiabatic motion could alter locations and energies of planetary ions precipitating onto the surface, and the resultant creation of new ions and neutrals from surface constituents. Since Na+-group ions can at times provide up to 25% of total plasma ion pressure in the central plasma sheet, these ions may, at times, share the role of determining magnetospheric dynamics with ions of solar wind origin. Finally, we have shown that planetary Na+-group ions, observed in Mercury's northern cusp, are swept in to the cusp rather than flowing out, as at Earth. Often correlated with dayside reconnection, this novel behavior serves to energize planetary ions in Mercury's active magnetosphere.

Chapter 1

Introduction

Mercury's space environment is one of extremes. Its similarities and differences with Earth and other planets test our understanding of planetary magnetospheres. Furthermore, its space environment is very tightly coupled to its thin atmosphere and surface, and is strongly influenced by large-scale features such as Mercury's orbit around the Sun, its spin rate and quite possibly its internal structure. This makes Mercury's space environment unique in the solar system. The purpose of this introduction is to provide an overview of these other aspects, and to set the stage for main body of this work, the first plasma ion measurements ever made at Mercury.

1.1 MESSENGER

Only two spacecraft have visited Mercury. The first was Mariner 10, which flew by Mercury three times in 1974-75. The second was MESSENGER, MErcury Surface Space Environment GEochemistry and Ranging [*Solomon et al.*, 2007], which first flew by Mercury on 14 January 2008 (M1). MESSENGER went on to fly by Mercury two more times on 6 October 2008 (M2) and 29 September 2009 (M3), before going into orbit on March 18, 2011. Successfully sending a spacecraft to orbit Mercury is not easy. The biggest problem is flying a spacecraft so deep into the Sun's gravity well then

slowing it sufficiently for capture into Mercury orbit. In fact, there was no practical trajectory design for a Mercury orbiter until 1985, when a trajectory was discovered which made use of many planetary gravity assist maneuvers to reduce fuel needs [*Wallace et al.*, 1985]. Following this trajectory, a spacecraft requires almost 7 years to get into Mercury orbit and 6 flybys, one of Earth, two of Venus and three of Mercury itself. Even with a mission-optimized version of this trajectory [McAdams et al., 2007], a very low mass, large propellant spacecraft was required: At launch, MESSENGER had a mass of just 1100 kg, over half of which was propellant. Orbiting Mercury also presents a tremendous thermal challenge. In direct sun, spacecraft components could quickly reach over 300° C, which far exceeds almost all operational limits. MESSENGER is protected from this intense solar radiation by a ceramic-cloth sunshade, which keeps most spacecraft components below 65° C. The second part of the thermal protection system is sophisticated attitude control autonomy. This system ensures that MESSENGER is always kept in the protective shadow of the sunshade, even when out of contact with Earth. Of course, MESSENGER is fitted with a full complement of scientific instruments. These are discussed briefly as part of the science discussion below [*Leary et al*, 2007].

Figure 1.1: MESSENGER during testing. From *Leary et al*. [2007].

One instrument aboard MESSENGER is the particular focus of this work: The Fast Imaging Plasma Spectrometer (FIPS), designed and built at University of Michigan [*Zurbuchen et al.*, 1998; *Andrews et al.*, 2007]. Its primary role is to measure ions of planetary origin, from elements H – Fe. FIPS is a time-of-flight (TOF) plasma mass spectrometer that measures ions with energy per charge (E/q) of 0.046 – 13.3 keV/e and with mass per charge ratios (m/q) of 1-60. It also measures the incident angle of ions as they enter its wide (1.4π steradian) instantaneous field-of-view (FOV). These measurements allow separation of planetary ions by m/q as well as characterization of their velocity distribution functions (described below). FIPS is a miniaturized instrument, with a mass of only 1.41 kg and using only 1.9 W of power (average), as

required by tight mass and power restrictions on MESSENGER. Figure 1.2 shows photographs of FIPS alone and after integration onto the MESSENGER spacecraft.

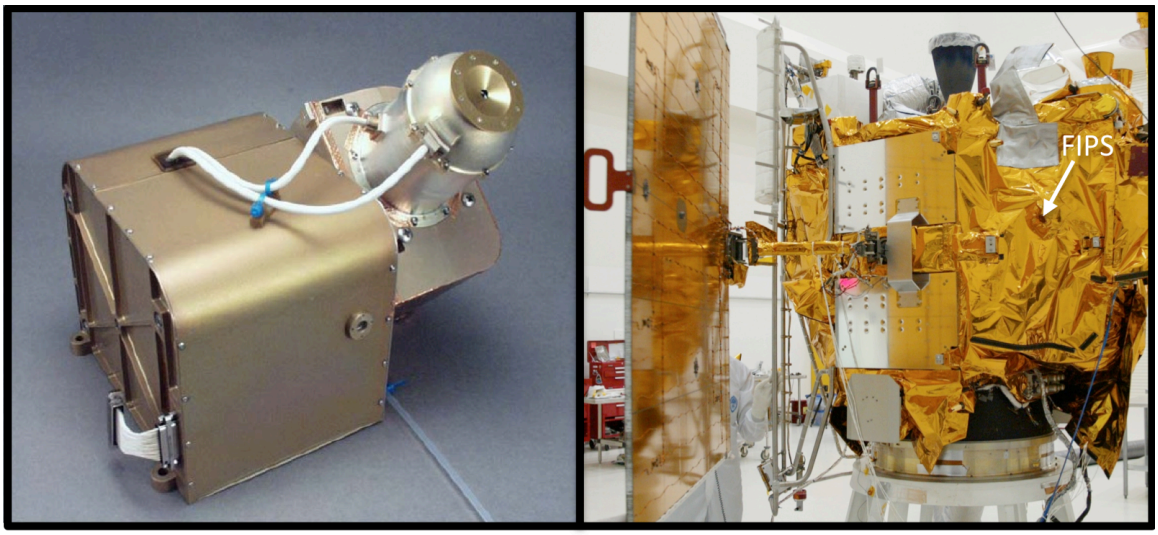

Figure 1.2: Photographs of the Fast Imaging Plasma Spectrometer (FIPS) before (left) and after (right) integration onto the MESSENGER spacecraft. The FIPS aperture is shown (white arrow) surrounded by gold thermal blanket during MESSENGER spacecraft assembly (right). Image credits: Adapted from *Andrews et al.*, 2007 (left); Jeff Kelley (right).

Figure 1.3 shows a simplified diagram of FIPS operation as well as a cut-away view of the 3D CAD model showing the same sections for reference. FIPS has three main operational units: electrostatic analyzer (ESA), post-acceleration region (PAV) and TOF telescope. The ESA uses a voltage applied to interior curved plates to select ions on the basis of their *E/q*. Ions must fall within ~3% of the target *E/q* in order to pass through the ESA without hitting the walls. As configured for the measurements in this work, the ESA voltage was stepped from 35 V to 10 kV logarithmically over 60 steps, admitting ions from 0.046 keV/e to 13.3 keV/e over the full energy scan. Besides *E/q* filtering, the complex geometry of the ESA serves to keep out UV light that would cause extra noise in FIPS detectors. Ions that successfully pass through the ESA gain energy through the post-acceleration region according to their *m/q*. This voltage was fixed at 10.5 kV for

this work. Ions then impact a thin layer of elemental carbon, known as a *carbon foil*. Ions experience some angular scattering and energy loss (1-5 keV, depending on mass) while passing through the foil, which is partially mitigated by the energy gained in post-acceleration.

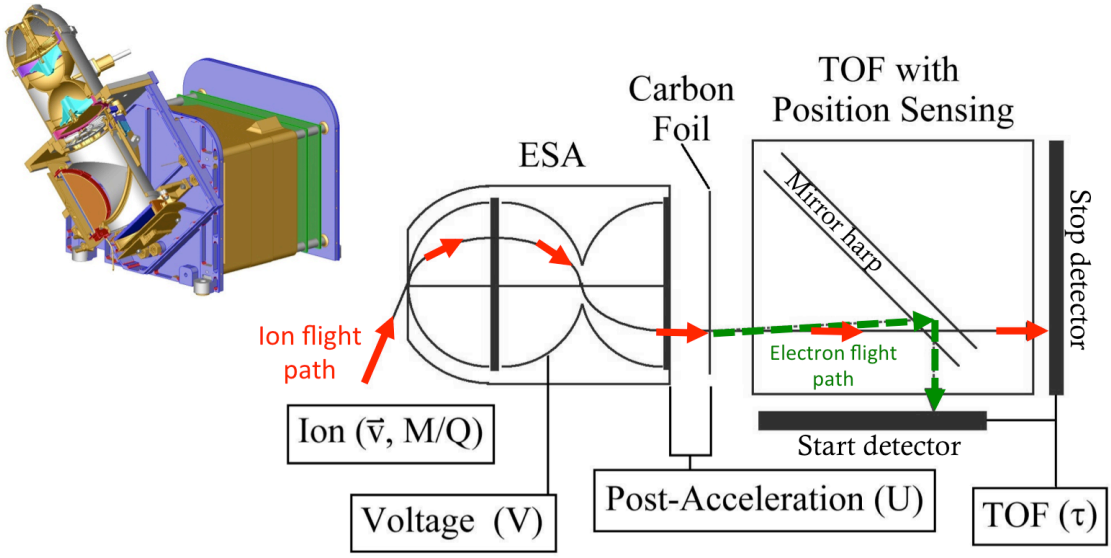

Figure 1.3: FIPS sensor operation (right) and cut-away view (left). The ion flight path is shown in red, while that of the electrons (emitted from the carbon foil) are shown in green. See text for details. Image credits: Robert A. Lundgren (left); Adapted from *Koehn* [2003] (right).

Upon exiting the carbon foil, ions enter the TOF telescope. The process of exiting the carbon foil frees 1-10 electrons from the foil (Figure 1.3 green dashed line). These electrons are directed onto the start micro channel plate (MCP) detector by an electrostatic mirror, a grid of fine wires called a mirror harp. When the electron(s) impact, the MCP creates a cascade of electrons that amplifies the signal to electronically measurable levels and starts the TOF timer. The impact location on the MCP is governed by the incident angle of the original ion into FIPS aperture. This mapping is most easily understood in a polar coordinate system on the MCP where the radius is related to the zenith angle of the ion in FIPS FOV and the azimuthal angle on the MCP is the same is the azimuthal angle of the ion in FIPS FOV. The ions, too massive to be deflected by the

mirror harp, continue on a straight trajectory to hit the stop MCP detector. This impact causes an electron cascade within the MCP that stops the TOF timer and causes the event to be processed by FIPS electronics. The net result is the measurement of both incident angles, *E/q* and TOF for individual ions.

1.2 Planet

Mercury is the smallest planet in the solar system, closest to the Sun, and experiences the most extreme solar environment among the terrestrial planets. It has a radius of 2440 km (R_M), much smaller than Earth's 6378 km, and correspondingly smaller gravity of 0.38g. Mercury's highly eccentric orbit varies from 0.31 Astronomical Units (AU) at periapsis to 0.47 AU at apoapsis over its roughly 88 Earth-day year. These orbital characteristics create a wide range in Mercury's orbital speed, 38-58 km/s, resulting in a very high average speed of ~48 km/s. A Mercury day is about 58 Earth days, making it the only planet in the solar system to have a 3:2 spin-orbit resonance. The orbit and rotation also manifest their effects on the surface of the planet by producing a temperature that varies between 700K at local noon to 100 K at local midnight. Compared to the Earth at 1 AU, Mercury at perihelion experiences solar radiation and solar wind density up to 10 times more intense.

Like Earth, Mercury has a solid silicate crust and mantle surrounding an iron-rich liquid middle core and a solid inner core (Figure 1.4). There are, however, many differences: Mercury's gravity field indicates that its internal structure is much different than the other terrestrial planets. A solid iron sulfide layer may separate the mantle and the liquid middle core and may account for Mercury's extraordinarily high density – the highest of the planets. The liquid middle core appears to be thicker than at other

terrestrial planets and much closer to the surface, within 400 km [*Smith et al.*, 2012; *Hauck et al.*, 2013]. This Fe-rich liquid middle core gives rise to an intrinsic magnetic field with a magnetic moment of 195 ± 10 nT-R_M^3, about 100 times weaker than that of the Earth [*Anderson et al.*, 2008, 2010]. The dipole field is nearly aligned to the axis of rotation, however magnetic field data show a clear northward offset of 484 ± 11 km from the planetary equator [*Anderson et al.*, 2011]. The proximity of the liquid middle core to the surface may have significant implications for Mercury's space environment (explained below).

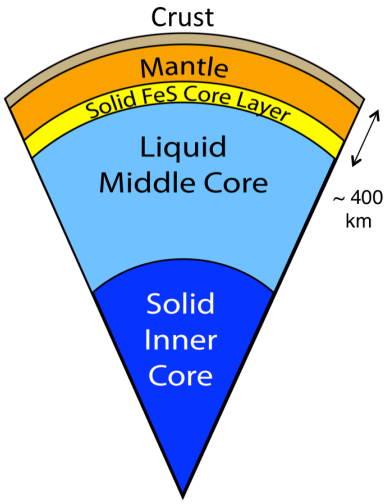

Figure 1.4: Mercury's internal structure. Image adapted from *Hauck et al.* [2012].

1.3 Surface

Mercury's surface composition was deduced from a combination of gamma ray, X-ray, and neutron spectroscopy. Evans et al. [2012] analyzed data from the Gamma Ray Spectrometer (GRS) [*Goldsten et al.*, 2007] and reported the following abundances for major surface components, in weight percent (Table 1.1). These abundances fit well with

those derived from measurements by the X-Ray Spectrometer (XRS) [*Schlemm et al.*, 2007; *Nittler et al.*, 2011] where the same elements were measured.

Si	Ca	S	Fe	Na	Al
24.6%	5.9±1.3%	2.3±0.4%	1.9±0.3%	2.9±0.1%	7.1+0.4/-0.9%.

Table 1.1: Abundances for major surface components, in weight percent [*Evans et al.*, 2012].

The surface of Mercury visually resembles the Moon: It is a grey expanse marked with plains, craters, ridges, and plateaus. MESSENGER has imaged 100% of the surface with the Mercury Dual Imaging System (MDIS) [*Hawkins et al.*, 2007], most in color and under different lighting conditions. Many interesting surface features have been discovered and several of these have implications that stretch into the exosphere and magnetosphere.

Most importantly, Mercury has been shaped by volcanism. A large fraction of the surface in the northern latitudes is covered with smooth plains, amounting to 6% of the full planet surface. These plains show several flow features, such as partially covered craters (called "embayed" craters), channels and flow fronts, which indicate that these plains were created by lava flows from erupting volcanoes. This discovery ended a debate about volcanism on Mercury, which had been ongoing since the Mariner 10 flybys and required the higher resolution MESSENGER images to settle. This lava should have a different mineral and elemental composition than the surface regolith [*Head et al.*, 2008; *Head et al.*, 2011]. Given the size of the smooth plains, expected difference in surface composition may be reflected in exospheric neutrals and ions, and possibly even be roughly localized to northern latitudes.

Over 20 years ago, ground based observations revealed the presence of radar-bright regions around Mercury's poles [*Slade et al.*, 1992; *Butler et al.*, 1993; *Harmon and Slade*, 1992]. One of the driving science questions of the MESSENGER mission is to explain these observations and determine the composition of this material. This goal has been accomplished during the orbital phase with data from a combination of three instruments. First, MDIS images were used to determine that all of the radar bright features are within craters with floors at least partially in permanent shadow [*Chabot et al.*, 2012]. Then, data from the MESSENGER Neutron Spectrometer (NS) [*Goldsten et al.*, 2007] taken from the North pole region was found to be consistent with water ice [*Lawrence et al.*, 2012]. Neutrons measured by NS come from the nuclear reactions that result from the interaction of cosmic rays with surface atoms. By comparison with forward modeled counts of epithermal and high-energy neutrals as a function of latitude, those authors showed that observed neutrons were consistent with a hydrogen-rich surface layer (tens of centimeters thick) only at high latitudes. Differences between the epithermal and high-energy neutrons indicate that this hydrogen-rich layer is buried under 10-30 cm of material that is less rich in hydrogen. Finally, the Mercury Laser Altimeter (MLA) was used to characterize surface reflectance in these craters. Thermal models of the observed reflectance are consistent with the presence of water ice. Furthermore, the MLA analysis showed that the overlying layer is likely to be complex organics. Both of these substances are believed to be due to impacts of comets or asteroids [*Neumann et al.*, 2012; *Paige et al.*, 2012]. Since they appear to be trapped rather than constantly replenished, it is difficult to speculate on the presence of signatures of these substances in the exosphere.

One of the most unexpected discoveries on the surface of Mercury has been the so-called hollows – shallow, irregular depressions with high-reflectance interiors. These hollows are found to be surrounded by bright, diffuse halos (Figure 1.5). Their interiors are typically smooth and flat, though some have hills or mesa. Hollows range in size from tens of meters to several kilometers. They are found within impact craters of varying sizes, as well as crater floors, walls and rims. It is hypothesized that hollows formed by loss of volatiles, possibly due to sublimation or space weathering. They do not appear to be directly related to observed volcanic vents, but given their spatial association, may be related to crater formation. If this is true, they add evidence to the argument that Mercury is not as depleted in volatiles as expected [*Blewett et al.*, 2011]. If formed by volatile loss, evidence of their composition should be present in the exosphere and magnetosphere.

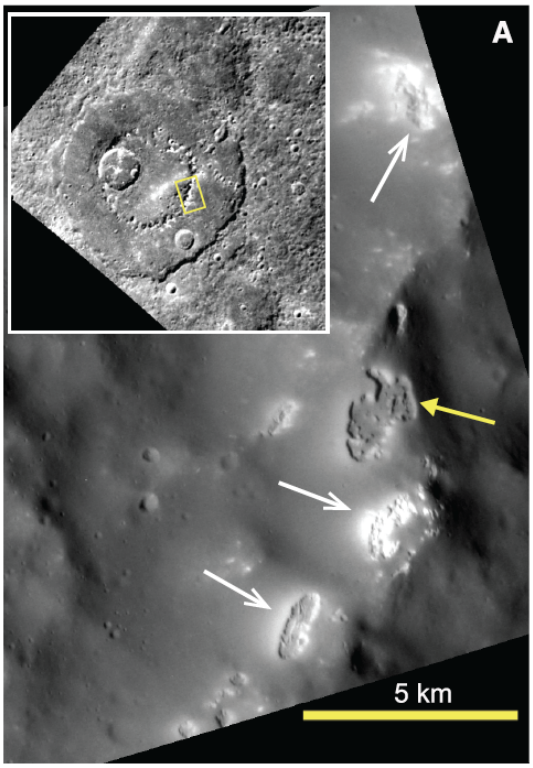

Figure 1.5. Examples of hollows on Mercury, characterized by irregular rimless depressions and associated high-reflectance materials. (**A**) Portion of a peak ring of a 170-km-diameter impact basin (inset). White arrows indicate depressions with high-reflectance interiors and halos. The floor of the hollow indicated by the yellow arrow has a reflectance similar to the surroundings. Image EN0213851669M, 15 m/pixel, centered at 34.4° N, 282.0° E. Adapted from *Blewett et al.* [2011].

1.4 Exosphere

Mariner 10 discovered Mercury's thin atmosphere with UV spectroscopy in 1974 [*Broadfoot et al.*, 1974]. Helium was detected, and upper limits were placed on H, C, O, Ne, and Xe. From column density estimates, the total surface pressure of the atmosphere was estimated at 2×10^{-7} Pa, the first indication that Mercury's atmosphere is a collisionless exosphere. Potter and Morgan [1985] discovered Na in the exosphere by ground observations from Earth, soon followed by K [*Potter and Morgan*, 1986]. Bida et al. [2000] first observed Ca from the ground. Sodium was observed stretching out >16 $\underline{R}_M$ behind the planet in a neutral tail, somewhat like a comet [*Potter et al.*, 2002]. This exosphere is formed by release of neutral atoms from various surface processes (Figure 1.6), making the surface and exosphere tightly coupled [*Domingue et al.* 2007]. These processes, explained below, include thermal desorption, photon-stimulated desorption, electron-stimulated desorption, solar wind sputtering, and micrometeroid vaporization. Estimates of fluxes from each of these processes vary considerably and can be quite controversial, so they are not included here. Many of the processes create ions as well, though in much smaller proportions (<10%). The exact fraction of ions created varies and still an active topic of research. The neutral atoms created by these processes form the seed populations for ions in Mercury's space environment.

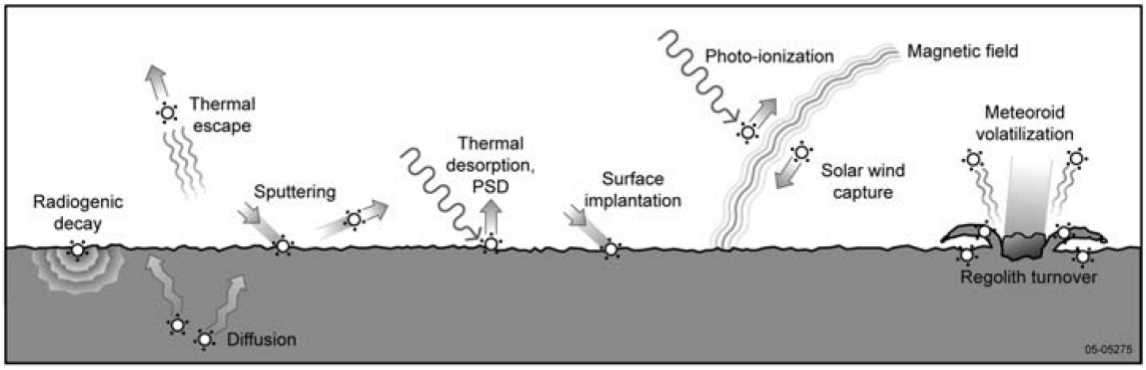

Figure 1.6. The sources, sinks, and processes within the exosphere, surface, and magnetopause of Mercury. From *Domingue et al.* [2007].

In the simplest case, atoms can be effectively baked off the surface in a process called thermal desorption. The free atoms produced are relatively low in energy, <1 eV. In the lab, bombardment with He^+ (1 keV) raised the temperature for peak desorption from 700K to ~950K [*Madey et al.*, 1998]. Mercury's surface is likely continually bombarded with He^{2+} from the solar wind so the peak thermal desorption temperature may be higher than expected from regolith composition alone. A variable fraction of desorbed atoms can achieve Mercury escape velocity, 4.3 km/s at the surface, and escape gravity, in a process called thermal escape [*Hunten et al.*, 1988].

Solar photons in the ultraviolet (UV) band can also cause the release of neutrals and ions via electronic excitation in Photon-Stimulated Desorption (PSD). This process depends linearly on UV photon flux and an element-dependent PSD cross-section factor. The cross-section is determined from laboratory measurements of materials selected to mimic Mercury's regolith. For example, to measure the PSD cross-section for Na on Mercury, Na is deposited on solid SiO_2, a material known to be similar to lunar regolith. These measurements yield accurate cross-sections, but depend strongly on photon energy, temperature and regolith composition, leaving many free parameters involved in

understanding PSD from the actual Mercury surface. Neutral atoms released from PSD have mean energies of 0.1 eV (Figure 1.7), with a very small fraction reaching 0.3 eV [Yakshinsky et al., 1999]. In a similar fashion to PSD, Electron-stimulated desorption (ESD) causes the release of material upon impact of electrons. Cross-sections for ESD are considerably larger than for PSD, by as much as 10 times, and increase with incident electron energy. ESD is otherwise subject to the same dependencies as PSD while additionally requiring conditions that allow electrons with energies > 2-4 eV to directly access the surface [*Yakshinskiy and Madey*, 1999]. Possible electron sources include precipitation due to magnetospheric circulation and direct impact by the solar wind [e.g. *Schriver et al.*, 2011]. Neutral atoms released by ESD are more energetic than those from most other processes, reaching energies of 10 eV [*McLean et al.*, 2011].

Of course, if solar wind electrons can impact the surface, solar wind ions can as well. When this happens, neutrals and ions can be released in a process called solar wind sputtering. The solar wind is mostly protons (H^+) and alpha particles (He^{2+}) with mean energies in the 1-2 keV range. The flux of particles sputtered off depends, of course, on the incident ion energy and flux, but also on the energy deposition properties of those ions into the surface regolith and the binding energy of ejected elements in the regolith minerals. As a result, sputtering flux depends on strongly on the surface composition [*Lammer et al.*, 2003]. The incident energy and flux of ions are not only determined by the upstream solar wind conditions but also by magnetospheric dynamics (discussed below), such as dayside magnetic reconnection, which control the area of the magnetospheric cusp open to solar wind impingement [*Masseti et al,* 2003; *Sarantos et*

al., 2007; *Potter and Morgan*, 1990]. Neutrals and ions released by this mechanism have energies in the 0.001-1.0 eV range, which is 0.3-3 km/s for Na [*Cassidy et al.*, 2005].

The last exosphere-forming process of importance comes from outside the planet: Mercury is continually bombarded with micrometeoriods, with impact rates depending on size. Those less than 100 μm in diameter basically impact continuously, while larger micrometeoriods, with diameters of ~1 cm, impact every few minutes. Micrometeroids in the 1-10 cm diameter range are thought to make the most important contributions to the steady-state exosphere. Impacting with speeds averaging 20-30 km/s (depending on size), micrometeroids vaporize themselves and surface minerals into a cloud of gas up to 5000 K at the impact location [*Killen et al.* 2007]. This temperature does not represent enough energy, ~0.4 eV, to overcome the first ionization energy of most surface elements, which is typically 5-25 eV, so that the majority of the ejecta remain neutral atoms. Furthermore, a study modeling vaporization on the Moon asserts that temperature of the ejected material should be less than the temperature of the vapor cloud [*Smyth and Marconi*, 1995]. There is little data on the energies of ejected atoms, however, at the moon, ejected Na atoms were found to have energies in the range of 0.53- 0.69 eV (2.1-2.4 km/s) [*Wilson et al.*, 1999]. Like other terrestrial planets, Mercury is occasionally hit by larger meteoroids (>10 cm) and bodies from the Main Asteroid Belt. While these events certainly cause substantial contributions to the exosphere, their effects are short term and their rarity makes them unimportant for the steady state [*Killen et al.,* 2007, and references therein].

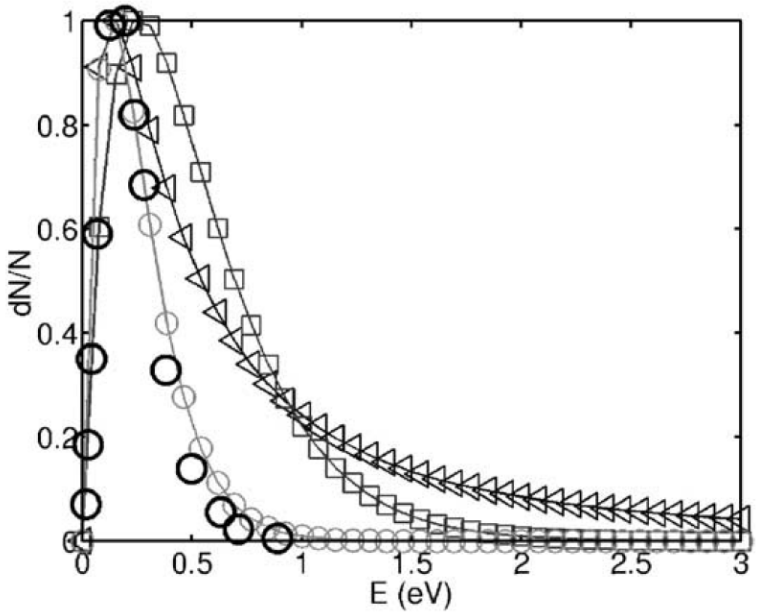

Figure 1.7: Energy distribution of sodium atoms ejected from Mercury's surface normalized by its maximum. Square line: micro-meteoroid vaporization. Triangle line: solar wind sputtering. Circle line: photon stimulated desorption. Dark circle symbols: measurements of *Yakshinskiy and Madey* (1999). From *LeBlanc et al.* [2003].

Once free of the surface, neutral atom trajectories are controlled mainly by gravity and radiation pressure, and depend on the energy with which they escaped the surface. On the dayside, the high temperatures cause most atoms to hop around the planet on ballistic trajectories, with a relatively small probability of sticking on any given hop. On the nightside, sticking becomes much more important, reaching fractions up 50%, so that the nightside can act as a cold trap for many atoms [*Yakshinskiy et al.*, 2000]. Aside from escape and sticking to the surface, the main loss process from the exosphere is photoionization. In this process, the energy of a solar UV photon striking a neutral atom causes an electron be ejected, forming an ion. On the energy scales of the exosphere and magnetosphere, this process is essentially energy neutral, so the product ion retains the energy of the neutral atom from which it formed. Photoionization rates are dependent on solar photon flux and the first ionization energy of the neutral atoms. Solar photon flux

increases as $1/R^2$, where R is the Mercury-Sun distance, so it is roughly 10 times higher at Mercury periapsis than at Earth. Ionization energies depend on the detailed atomic orbital structure of the neutral atoms, with those of Group I alkali metals (e.g. Na and K) being among the lowest and Noble gases (e.g. He) among the highest. Since photoionization rates are small, the photoionization lifetime is a more intuitive quantity to compare. This is just the inverse of the ionization rate and represents an average time that a particular atom can exist in the system without becoming ionized. Estimates vary, but the Na photoionization lifetime is probably 5500-14,000 s [*Huebner et al.*, 1992; *Millilo et al.*, 2005].

These processes have been modeled in detail with high-resolution global numerical models [e.g. *Burger et al.*, 2012; *Leblanc and Johnson,* 2003; *Leblanc and Johnson*, 2010; *Mura et al.*, 2005; *Sarantos et al.,* 2011; *Wurz et al.*, 2010]. These models have provided a very effective means of hypothesis testing, where very small subsets of free parameters can be varied to selectively study individual processes or effects. However, Mercury modeling has yet to reach its ultimate goal, to determine the relative contribution of each source and sink process to the whole exosphere because the models are severely under-constrained. There are a very large number of free parameters and there is either little information or little consensus on their values. Laboratory measurements are accurate but depend critically on the actual surface composition and environment. Remote sensing typically measure a convolution of many parameters that have not been successfully separated, e.g. temperature distributions, sticking coefficients, surface composition, and many, many more. And, of course, *in situ* data is taken one narrow orbital slice at a time, making interpretation in a global context at a single time

challenging. Part of the solution to this problem is clearly more data from Mercury, which is beginning to be provided by MESSENGER.

Mercury's highly eccentric orbit combined with its 3:2 spin orbit coupling causes substantial impact on its exosphere, collectively referred to as seasonal effects. In the most basic sense, the photon flux on the surface varies like $1/R^2$. This amounts to a factor of 2.2 increase in photon flux at Mercury's periapsis (0.31 AU) compared to apoapsis (0.46 AU). Secondly, the solar wind density varies in the same fashion while the speed stays constant with R (at these distances), causing the same $1/R^2$ dependence in the solar wind flux (the produce of density and speed). These two factors drive the largest seasonal changes to the exosphere, through the mechanisms described above. There is a third effect, which has less impact but is not negligible. As Mercury moves between periapsis and apoapsis, Mercury's radial velocity (with respect to the Sun) changes from -10.06 km/s to 10.06 km/s, altering the Doppler shift of the Sun's EUV spectrum (in Mercury's frame). This causes exospheric neutrals to experience different radiation acceleration, changing their velocity along the Mercury-Sun line and making observable changes to the exospheric distribution [*Potter et al.*, 2007]. Radiation acceleration is not a factor once the planet reaches periapsis or apoapsis, only during the transition between them.

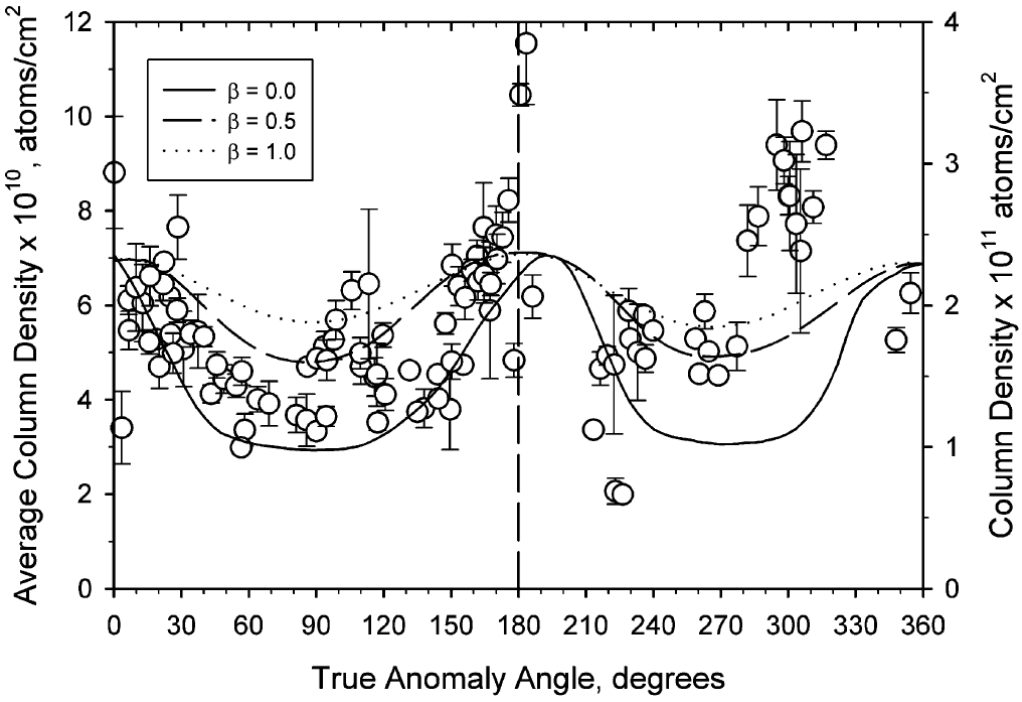

Figure 1.8: Average column density data computed from the acceleration-corrected data of Fig. 8 is compared with predictions of *Smyth and Marconi* [1995]. There are three overlays on this plot, taken from Fig. 15 of the *Smyth and Marconi* [1995] paper, in which they took into account radiation acceleration and the interaction of the sodium atoms with the surface. A value of $\beta = 0$ implies that there is no interaction with the surface, $\beta = 1$ implies that all the energy of the atom is lost upon contact with the surface, and $\beta = 0.5$ is an intermediate case. For true anomaly angles less than 180°, most of the data follow the $\beta = 0$ line, except for a region just past the point of maximum radiation acceleration, implying little energy exchange with the surface. For true anomaly angles greater than 180°, the observations fall closer to the $\beta = 0.5$ line, except for the region near the point of maximum radiation acceleration, where there is a large jump. From *Potter et al.* [2007].

These seasonal variations have been examined by ground-based observations. Potter et al. [2007] observed Mercury Na over a large range of Mercury True Anomaly Angle (TAA) from 1997 to 2003. (TAA defines the position of Mercury in its orbit, starting with periapsis TAA 0°.) After correcting for radiation acceleration effects, they found several peaks in Na emission on the planet's disk at TAA 180° (apoapsis) and 310°, with smaller peaks at TAA 15° and 105° (Figure 1.8). Schmidt et al. [2012] measured emission from Mercury's tail over several different TAA, also taking radiation acceleration into account. They found that exospheric escape was enhanced during

periods of large radiation acceleration, which were coincident with periods of low column density reported by Potter et al. [2007]. Interpreting a collection of observations taken throughout a Mercury year is complicated by the fact that solar wind conditions also play a large role in the exosphere. Those conditions change rapidly and are independent of the Mercury season. Furthermore, before MESSENGER, there was no way to measure these conditions *in situ*. Some indications of solar wind conditions were deduced from heliospheric radial tomography [*Killen et al.,* 2001], but this is difficult to do at the time resolution necessary to really capture solar wind variations.

Despite the limitations described above, the best understanding of seasonal changes thus far has come from global exosphere modeling, due to the ability to precisely dictate which parameters change while holding the others constant. *Ip* [1986] studied the effects of radiation acceleration on neutral Na escape, as well as the effect of recirculation of Na^+ on maintaining the Na exosphere. *Lammer et al.* [2003] developed a comprehensive UV model to assess the expected seasonal variations in Mercury's exosphere due to PSD changes throughout Mercury's orbit. They paid particular attention to the choice of parameters in the PSD governing equations and considered a wide range of atoms (O, Na, K, and Ca). They also studied the seasonal variation of solar wind sputtering, in conjunction with a model of surface area open to solar wind impingement in Mercury's magnetospheric cusps [*Massetti et al.*, 2003]. The authors found that together these two processes, under quiet solar wind conditions, may produce the same order of magnitude of exospheric particles as micrometeoroid vaporization.

Leblanc and co-authors adapted a 3D Monte Carlo exospheric model from Europa to Mercury and used it to study the seasonal variation of the Na exosphere, as well as the

relative contributions from each of the source processes [*Leblanc and Johnson*, 2003]. This model included all the processes described above (except ESD), with parameters chosen mostly *a priori* from laboratory measurements. It also includes surface trapping of ions and neutrals and keeps track of the surface reservoir to model depletion of Na from the surface. They found a significantly different Na distribution on the day and night sides of the planet, which they attribute to trapping on the cold night side of the planet. They also found an asymmetry between dawn (rotating into the Sun) and dusk (rotating out of the Sun), which varies with Mercury season. Na column density on the morning side was always greater than that of the dusk side, the ratio reaching a maximum of 10 in the TAA 140°-230° range.

The same authors updated the model in response to the availability of new ground-based measurements [*Leblanc and Johnson*, 2010] from Potter et al. [2007]. These new measurements included the clear observation of an enhancement of dawn Na column density over the dusk value, which added weight the earlier assertion [*Leblanc and Johnson*, 2003] that dayside to nightside migration of Na is an important process in Mercury's Na exosphere. In updated model, they refined their model of Mercury's surface by including two populations of Na, the physically adsorbed (physisorbed) on to the surface and a second population chemically adsorbed (chemisorbed) within the surface mineral grains. They also improved their model of solar wind sputtering by modeling the interplanetary magnetic field (IMF) following statistics taken from the Helios mission [*Potter et al.*, 2006; *Sarantos et al.*, 2007]. They compared these results with the new ground-based measurements of Na emission and confirmed strong season dependence of the Na exosphere. Their principle conclusion is that no single ejection

mechanism dominates over an entire Mercury year. Instead, they find that Na emission features at certain TAA are the result of one process becoming temporarily dominant. They found that the Na content of the exosphere was at a maximum for TAA 0° and 180° and about 3 times lower at the minimum, TAA 70° and 140°.

Several of the main exospheric constituents have been measured directly by the UltraViolet and Visible Spectrometer (UVVS), part of the Mercury Atmospheric and Surface Composition Spectrometer [*McClintock and Lankton*, 2007]. UVVS measures one species at a time via one narrow frequency range and integrates emission in that range collected with its small (125 mm focal length) telescope along its entire line of sight (LOS). The instrument is mounted with most of the instruments in the MESSENGER adaptor ring and is pointed by spacecraft rotations, because it does not have a gimbal (to save mass). It must therefore share pointing control time with the rest of the MESSENGER instruments. During the M1 flyby, Na, Ca and H were detected, with Mg detection added during the M2 flyby [*McClintock et al.*, 2008; 2009]. In the orbital mission, UVVS is able to observe Na, Mg and Ca on a daily basis in the exosphere. These three atoms have some of the largest solar photon scattering probabilities (g-values) of the species of interest at Mercury [*Killen et al.*, 2009], and therefore produce the most intense signal. Oxygen and Ca^+ ions (M3) have also been detected. The measurements have shown that Na, Mg and Ca have different spatial distributions in Mercury's neutral tail. Na shows peaks at high latitudes, consistent with solar wind sputtering from the cusp, and appears as a combination two distributions, each with a distinct temperature [*Vervack et al.*, 2010]. Altitude profiles of Mg indicate that species to be in a very hot Maxwellian distribution of 10,000-50,000 K. The fact that Mg

is observed in the neutral tail despite its nearly-negligible radiation pressure is evidence that its temperature is in the upper portion of that range [*Killen et al.*, 2010].

The UVVS instrument must take LOS measurements from many different angles through the same region of space in order to reconstruct a 3D distribution of the observed species around the planet. As such, forward modeling of the exospheric emissions is a more practical approach. Burger et al. [2012] did this by comparing a small set of UVVS altitude profiles to a 3D Monte Carlo model of Mercury's Ca exosphere. This modeling showed that an isotropic distribution about the planet does not fit the data well. In fact, the best results came from placing a single hot source of Ca at the dawn equator, reproducing the observed enhancement there. Calcium temperatures of 20,000-50,000K fit the data equally well within 0.5 R_M, but with measurements from > 3 R_M indicate a temperature on the higher end (though poorly constrained).

1.5 Magnetosphere

The Mercury magnetosphere is much like the Earth's: It results from deflection of solar wind around the intrinsic planetary dipole field. Mercury's intrinsic field was first discovered in Mariner 10 data from the first flyby of the planet in 1974 [*Ness et al.*, 1974]. The observations also provided evidence of a detached bow shock and a magnetsheath region of high magnetic field variations, surrounding a magnetospere dominated by the planetary field. Mariner 10 carried plasma ion and electron instruments, though the ion instrument failed to operate [*Ogilvie et al.*, 1974]. The electron data showed a decrease in flow velocity and increase in electron flux and temperature, upon crossing the bow shock from the solar wind into the magnetosheath. The spacecraft then crossed a thin boundary of high electron flux, the magnetpause,

before passing into a region of very low electron flux, Mercury's magnetosphere. Before the first Mariner 10 flyby, Mercury was generally considered to interact with the solar wind weakly, like our own Moon. The combination of the magnetic field and electron measurements from Mariner 10 showed clearly that Mercury has a strong interaction with the solar wind, forming a magnetosphere that appeared to be morphologically similar to that of the Earth (Figure 1.9).

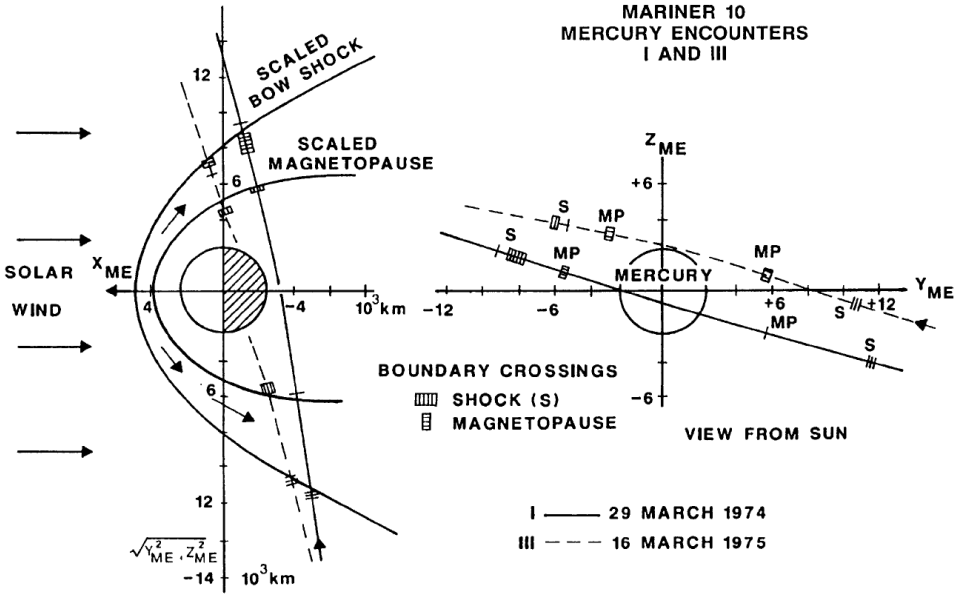

Figure 1.9: The Mariner 10 trajectories during the first, MI, and third, MIII, encounters. From *Slavin* [2004].

Despite similarities between the magnetospheres of Mercury and Earth, there are many differences. First, the solar wind at Mercury is hotter and more 5-10 times more dense (depending on radial distance from the Sun), than at Earth. This results in a 5-10 fold increase in dynamic pressure applied at the magnetopause. Second, Mercury's intrinsic magnetic field is about 100 times weaker than that of the Earth. The weak intrinsic magnetic field coupled with increased pressure shrinks the magnetosphere relative to the size of the planet, so that the Mercury takes up a much larger volume in its

magnetosphere than the Earth. This difference is indicated from the average magnetopause standoff distances of 1.5 R_M [*Slavin et al.*, 2010; *Winslow et al.*, 2012] and 10 R_E [*Fairfield*, 1971] for Mercury and Earth, respectively. As a general rule, spatial scales on Mercury are about 1/8 that of Earth. Third, Mercury's northward dipole offset of 0.2 R_M generates an asymmetry in the magnetosphere, causing the southern magnetospheric cusp to be larger in area, exposing more of the planetary surface, than the northern, among other things. Fourth, Mercury's very slow rotation rate, ~58 days, greatly reduces the importance of plasma populations co-rotating with the planet, if they exist. Finally, and possibly the most important difference, Mercury has no collisional ionosphere through which to close magnetospheric currents [*Slavin*, 2004].

Analysis of MESSENGER Magnetometer [*Anderson et al.*, 2007] data has confirmed that Mercury's magnetosphere is highly dynamic and extreme. *Slavin et al.* [2009a] estimated that the Dungey cycle [*Dungey* 1961] time for magnetospheric convection is about 30 times faster at Mercury (~2 min) than the Earth (~60 min). *DiBraccio et al.* [2013] completed an extensive study of MESSENGER magnetopause crossing identification and the occurrence of magnetic reconnection at this boundary. Those authors estimated the reconnection rate at the magnetopause boundary by calculating the average ratio of the normal magnetic field component to the magnitude of the field inside the magnetosphere, adjacent to the magnetopause. They found that the reconnection rate at Mercury is about 3 times larger than at Earth, with a value of ~0.15. Furthermore, they found that the reconnection rate was essentially independent of magnetic field shear angle – a direct result of the low plasma β environment in Mercury's magnetosheath. This

means that reconnection at Mercury is possible for essentially all IMF orientations, not just the antiparallel, southward IMF B_Z configuration, as at Earth.

One manifestation of (localized) reconnection is the presence of Flux Transfer Events (FTEs). These are isolated magnetic flux tubes that get connected to the IMF by reconnection, then pulled from the dayside into the (nightside) magnetotail by the (anti-sunward) solar wind flow. FTEs often have a flux rope topology, with magnetic field wound in a helical pattern around a central core field [*Borg et al.*, 2012; *Slavin et al.*, 2010]. FTEs at Mercury are extreme in both size and frequency. Slavin et al. [2010] reported FTEs that were about 1 R_M (2440 km) in diameter. Relative to the size of the planet, this is about 20 times the size typically found at Earth. An FTE of this size would have increased the area of the surface exposed to the solar wind by 10-20% and may have increased the cross-polar cap potential by up to 30 kV [*Slavin et al.*, 2010a]. The latter could substantially increase centrifugal acceleration of ions which are pulled out of the cusp and into the magnetotail [*Delcourt et al.*, 2012]. This can lead to both increased loss of cusp plasma to the solar wind and increased energy of those ions that do make it into the magnetotail.

In fact, the FTEs resulting from reconnection at the dayside magnetopause can erode a large fraction of the dayside magnetosphere and load the magnetotail with magnetic flux. This sort of tail loading powers magnetospheric substorms at Earth. The larger tail loading, ~10 times flux increase Earth, could mean that substorms at Mercury are much more intense [*Slavin et al.*, 2010b]. In addition, the erosion of flux from the dayside will decrease the magnetopause subsolar standoff distance and may eventually expose more of the planetary surface to solar wind impact. Recent results suggest an additional effect:

as the magnetopause becomes eroded toward the surface, the reduced magnetopause standoff distance may induce currents in Mercury's liquid core, which in turn, produces induced magnetic field that act to resist further reduction [*Slavin et al.*, 2013]. If verified, this represents a novel situation on Mercury where conditions in the space environment, driven by the solar wind, couple into the very core of the planet.

Other dynamical features have been observed in Mercury's magnetosphere. FTEs can come with very high frequencies, over 50 times more frequent that at Earth. These individual 2-3 s duration FTE events can repeat every 8-10 s, forming an "FTE shower", versus Earth where FTEs are typically observed to repeat every 8 min. Unlike the extreme FTEs described above, the FTE shower flux ropes have typical diameters of 0.15 R_M, and appear to be quite common. These high repeat rates, coupled with the very short Dungey cycle time (~2 min) indicate that FTEs may be the primary drivers for magnetospheric convection [*Slavin et al.*, 2012]. *Sundberg et al.* [2010] observed multiple crossings of the magnetopause which they identified as Kelvin-Helmholtz waves along the boundary. These waves, resembling a series of just-breaking ocean waves, could cause significant mixing of plasma between the magnetosheath and magnetosphere.

1.6 Guiding Science Questions

The studies in this work were guided by three over-arching science questions, which have broad implications in the Mercury space environment. These questions are as follows:

1. Are the spatial distributions and kinetic properties of plasma ions consistent with a Mercury magnetosphere that is morphologically similar to that of Earth?

Mariner 10 magnetic field and plasma electron measurements gave strong indications that Mercury's magnetosphere is morphologically similar to that of Earth [*Bame et al.*, 1974; *Ogilvie et al.*, 1974]. However, due to a failure of the plasma ion instrument, there were no ion measurements returned during any part of the Mariner 10 mission. At Earth, the ions carry most of the plasma thermal pressure, and play a fundamental role in determining the overall properties and dynamics of the magnetosphere. Characterization of ion properties at Mercury is vital to confirm this suspected morphological relationship.

2. What is the nature of the coupling in the surface-exosphere-magnetosphere system?

As explained above, theory and simulations clearly predict a tight coupling between Mercury's surface, exosphere and magnetosphere. In situ ion composition measurements are the primary method for characterizing any coupling processes. This coupling can be addressed by investigated how strongly planetary ion behavior and abundances are dictated by their parent exospheric neutral populations, and how similar their properties are to those of solar wind origin.

We described above that many of the processes liberate neutral atoms from Mercury's surface generate ions as well. Mercury's exosphere is collisionless even at the surface, so ions generated there constitute a direct coupling between the surface and magnetosphere. Conversely, planetary ions themselves may generate neutral atoms or ions when they

impact the surface by precipitation along the planetary magnetic field. Is there evidence of this direct surface – magnetosphere coupling in planetary ion measurements?

3. What role do planetary ions play in Mercury's magnetosphere?

If heavy planetary ions (mass > 4 amu) are present in Mercury's magnetosphere, several models [*Delcourt et al.*, 2003; *Sarantos et al.*, 2007] suggest that they will behave differently in Mercury's miniature magnetosphere when compared with Earth. In particular, Na^+ ions, with their high mass to charge ratio (m/q=23), would have gyroradii on the order of Mercury's planetary radius, for energies of a few keV. This radius is a substantial fraction of Mercury's magnetotail, resulting in substantial magnetic field gradients over the course of a single ion gyration around its guiding center. It is expected that the guiding center approximation commonly applied to magnetospheric ions, will break down, and that these demagnetized particles will behave non-adiabatically. Composition and energy measurements provided by FIPS may confirm and characterize this behavior.

If planetary ions are present in Mercury's magnetosphere in sufficient numbers, they may have an effect on magnetospheric dynamics. Hot, massive planetary ions could contribute substantially to plasma thermal pressure or mass density even if they make up only a small fraction of the proton number density. If these massive ions are tightly coupled to magnetospheric convection in Mercury's magnetotail, the resultant mass loading may slow plasma flows. Alternatively, the effects of these heavy planetary ions may be dominated by the non-adiabatic behavior described above.

Only direct measurement of these ions with FIPS can resolve these questions. Here, we describe the data analysis studies used to address these questions in the following chapters. In Chapter 7, the results and conclusions from these studies are placed into the context of these guiding questions.

Chapter 2

MESSENGER Observations of the Composition of Mercury's Ionized Exosphere and Plasma Environment

This chapter is taken from Thomas H. Zurbuchen, Jim M. Raines, George Gloeckler, Stamatios M. Krimigis, James A. Slavin, Patrick L. Koehn, Rosemary M. Killen, Ann L. Sprague, Ralph L. McNutt, Jr., and Sean C. Solomon (2008), MESSENGER Observations of the Composition of Mercury's Ionized Exosphere and Plasma Environment, *Science, 321*, 90-92. I performed the data reduction which is represented in Figure 2, as well as substantial analysis that informed the science interpretation. I contributed to the text and manuscript preparation.

Abstract: The region around Mercury is filled with ions that originate from interactions of the solar wind with Mercury's space environment and through ionization of its exosphere. The MESSENGER spacecraft's observations of Mercury's ionized exosphere during its first flyby yielded Na^+, O^+, and K^+ abundances consistent with expectations from observations of neutral species. There are increases in ions at mass per charge (*m/q)* = 32 to 35, which we interpret to be S^+ and H_2S^+ with $(S^+ + H_2S^+)/(Na^+ + Mg^+) = 0.67 \pm 0.06$, and from water-group ions around $m/q = 18$, at an abundance of 0.20

± 0.03 relative to Na^+ plus Mg^+. The fluxes of Na^+, O^+, and heavier ions are largest near the planet, but these Mercury-derived ions fill the magnetosphere. Doubly ionized ions originating from Mercury imply that electrons with energies less than 1 kilo-electron volt are substantially energized in Mercury's magnetosphere.

Since the discovery of Mercury's internal magnetic field during the Mariner 10 flyby encounters in 1974—1975 [*Ness et al.*, 1974], there has been speculation about the nature of the interactions of the solar wind and electromagnetic fields with Mercury's surface and near-planetary exosphere [*Slavin et al.*, 2007]. These interactions were surmised from remote measurements of the neutral exosphere [*Potter and Morgan*, 1990] because Mariner 10 did not provide any direct observations of the ionized component or characterize Mercury's ion plasma environment. Because of the comparatively small size of Mercury's magnetic field, its tenuous atmosphere, and its close proximity to the Sun, Mercury's surface is subject to more direct space-weathering interactions than are those of other terrestrial planets. In addition to ejecting neutral particles that form Mercury's exosphere, surface-sputtering interactions can lead directly to ionized components. Such newly formed ions can also originate in the exosphere through ionization. In either case, these ions are created approximately at rest near the planet and then undergo energization by electromagnetic processes that dominate Mercury's space environment. The MESSENGER spacecraft measured a mass-per-charge (m/q) spectrum of ions in Mercury's exosphere during its first flyby on 14 January 2008 (Figure 2.1). These measurements were performed by the Fast Imaging Plasma Spectrometer (FIPS), the low-energy portion of the Energetic Particle and Plasma Spectrometer (EPPS) instrument [*Andrews et al.*, 2007] aboard MESSENGER.

Here, we focus on the relative abundances of ions in the *m/q* range between 4 and ~50 atomic mass units (amu) per unit of charge (e). Ions with a *m/q* <4 (H^+ and He^{++}) largely originate from the solar wind; ions with a *m/q*>10 are generally produced locally. Ions with *m/q* of 23 to 24 (Na^+ plus Mg^+) are clearly the most dominant heavy ions (Table 2.1). Neutral Na has been observed remotely from Earth [*Potter and Morgan*, 1990] and also during the MESSENGER flyby [*McClintock et al.*, 2008].

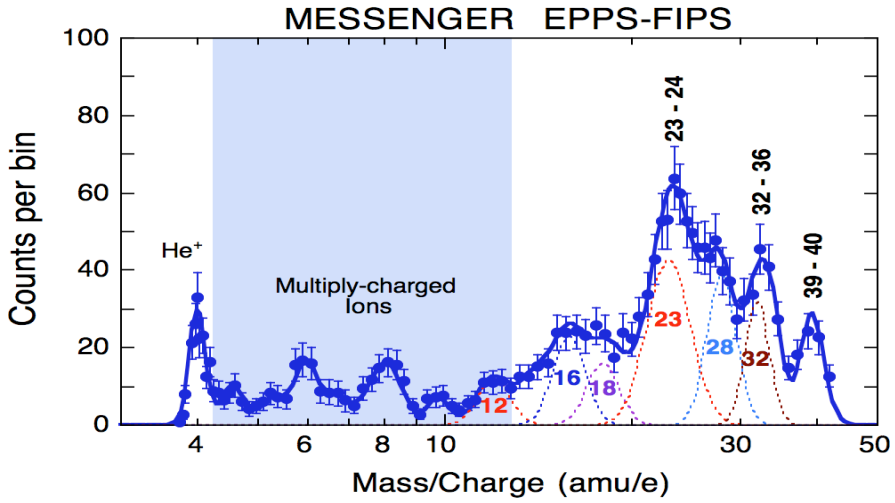

Figure 2.1. Counts from the FIPS sensor per *m/q* bin versus *m/q* of ions with 3.8 < *m/q* < 42 accumulated in Mercury's magnetosphere between 18:43 and 19:14 UTC during the flyby on 14 January 2008. Thin curves are Gaussian fits to several major peaks of the *m/q* histogram, and the thick curve is the sum of all Gaussian distributions. Multiply charged ions are observed primarily below *m/q* ≈ 12. FIPS measures the energy per charge (*E/q*) on an ion from 0.1 to 13.5 keV/e, its arrival direction with an angular resolution of ~15°, and the *m/q* ratio (derived from *E/q* and a time-of-flight measurement) determined to an accuracy σ (*m/q*) = Δ(*m/q*)/(*m/q*) that ranges from 0.04 to 0.08, depending on the mass of the ion. Because of limited counting statistics, we followed a minimum-least-squares procedure to estimate the relative abundance of an ion at a given allowed *m/q* using log-Gaussian distributions with σ (*m/q*) calculated from preflight calibrations.

Although Na^+ dominates, several secondary peaks (around *m/q* = 16 to 18, 32 to 36, 28, and 39 to 40) also stand out. We identified these peaks, respectively, as predominantly O^+ and water-group ionized molecules; S^+ and H_2S^+; and the surface-bound mineral components Si^+, K^+, and Ca^+. We cannot rule out additional contributions to ions in the

dominant peaks from nearby elements and various molecular species (some are listed in Table 2.1).

Table 2.1. Abundance ratios of possible ions and molecular ions relative to Na^+ plus Mg^+.

Mass/charge (amu/e)	Representative ion or molecular ion species	Aundance ratio*
23–24	Na^+, Mg^+	1.00
32–35	S^+, O_2^+, H_2S^+	0.67 ± 0.06
28	Si^+, Fe^{++}	0.53 ± 0.06
39–40	K^+, Ca^+	0.44 ± 0.05
17–19	H_2O^+, H_3O^+, OH^+	0.20 ± 0.03
4.67–11	Multiply charged ions	0.20 ± 0.03
16	O^+	0.20 ± 0.03
14	N^+, Si^{++}	0.09 ± 0.02
11–12	C^+, Na^{++}, Mg^{++}	0.08 ± 0.02
4	He^+	0.03 ± 0.01

*Abundance (relative to the sum of Na^+ and Mg^+) of the sum of ions and molecular ions listed in column 2. Uncertainties are dominated by limited counting statistics.

The abundances of Si and especially of Na and S relative to O in the solar wind [*von Steiger et al.*, 2000] are too low and their ionization states too high to account for the abundances of these ions. Their source is, therefore, either Mercury's surface or its exosphere.

When inbound, MESSENGER passed through the plasma sheet, the region between the two lobes of the magnetotail. This region is a natural magnetospheric reservoir for hot plasma with energies up to at least several thousand electron volts and densities of at least 1 cm^{-3} [*Mukai et al.*, 2004]. Plasma-sheet electrons are most likely the ionization source for the creation of multiply charged ions (such as O^{++}) observed by FIPS from corresponding singly ionized atoms (such as O^+). MESSENGER does not directly measure thermal and suprathermal electrons. However, our detection of multiply charged ions provides indirect evidence for the presence of a hot electron component near the planet

and supports the indirect detection of ~1 to 10-keV electrons in this region by MESSENGER's X-Ray Spectrometer [*Mazzotta et al.*, 1998; *J. A. Slavin et al.*, 2008].

The variation of the relative count rates of the key components of Mercury's plasma environment as sampled by MESSENGER can be correlated with the global structure of Mercury's magnetosphere [*Kabin et al.*, 2000; *Kabin et al.*, 2000] (Figure 2.2), including two crossings of the magnetospheric bow shock and two crossings of the magnetospheric bow shock and two crossings of the magnetopause (which separates solar wind from magnetospheric plasma). The maximum intensity of the heaviest ions occurred at the point of closest approach, 201.4 km above Mercury's surface (Figure 2. 2, top).

The energy distribution of protons originating from the solar wind substantially increased at the bow shock (Figure 2. 2A). Unperturbed solar wind was not directly measured by FIPS because of the sensor's location behind MESSENGER's sunshade. Within the magnetosphere, however, protons are easily measured because of a decrease in Mach number at the bow shock and deflections of the solar wind from the solar direction. Two distinct flux enhancements from 18:10 to 18:30 UTC were caused by spacecraft rotations about the solar direction. He^{++} ions, a direct indicator of solar-wind plasma (Figure 2. 2B), were found throughout the magnetospheric pass. The flux in the m/q range $3 < m/q < 10$ (Figure 2.2C) shows behavior in qualitative agreement with the spatial distribution of He^{++} ions, indicating in turn either a solar-wind source or direct coupling of the ions to such a solar-wind source through a charge exchange of Mercury-derived, singly charged ions with the solar wind. This connection includes multiply charged ions, such as O^{++} and C^{++}. A clear dominance of these contributions was found in the vicinity of the magnetopause, marked with blue dashed lines in Figure 2.2.

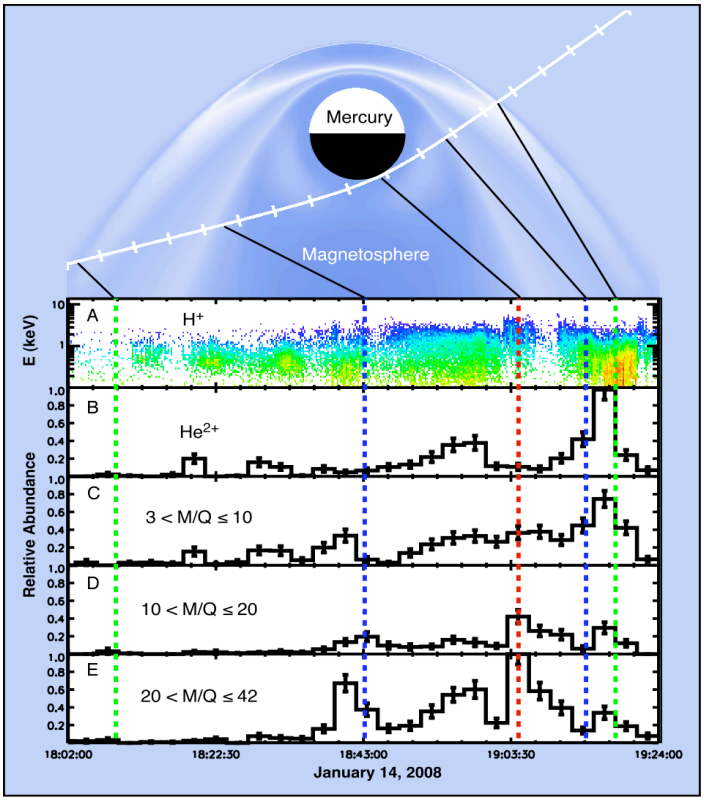

Fig. 2.2 Spatial distribution of key plasma components in relation to magnetospheric structure (*11*). (**Top**) Overview of magnetospheric geometry from a magnetohydrodynamic simulation (*10*) used to order the timeline of the MESSENGER flyby and the locations and encounter times of key components of the Mercury space environment. (**A** and **B**) Energy distribution of protons (at a resolution of 8 s, during which FIPS performs a complete *E/q* stepping sequence from 0.1 to 13 keV/e) and normalized He^{++} flux. Both species originate in the solar wind. Temporal variability of these components is associated with changes in plasma characteristics, as well as with temporal variability of the obstruction geometry, especially for solar wind protons. (**C**, **D**, and **E**) Normalized fluxes of ions in specified *m/q* ranges. All fluxes [(B) to (E)] are normalized to the peak flux in He^{++}. The fluxes of heavy ions with $10 < m/q < 42$ maximize near the planet but are also found throughout the magnetosphere. During the flyby, the spacecraft sunshade, one of the solar panels, and other spacecraft structures limit the field of view of FIPS to ~ p steradians. Vertical dashed lines denote the crossing of the bow shock (green), the magnetopause (blue), and the point of closest approach (red), based on magnetic field data (*9,11*).

The distribution of ions with $10 < m/q < 42$ is dominated by peaks at $m/q = 16$ to 18 and $m/q = 23$ to 24 (Figure 2.2, D and E). The large number of these ions implies that the ionized exosphere of Mercury extends throughout the magnetosphere and therefore must have an extended source.

For the heavy ions observed by FIPS that correspond to previously known neutral species Na, K, and Ca, their relative counts are consistent with photoionization, given known exospheric column abundances and photoionization rates [*Huebner et al.,* 1992]. Because most of the heavy ions were seen near the point of closest approach, where the spacecraft traversed the plasma sheet, electron-impact ionization of neutral species probably also contributes to the observed ion population. The apparent dawn-dusk asymmetry may be attributed to the flyby geometry: The spacecraft entered the magnetopause far down the dusk flank and exited the magnetosphere on the near-dawn dayside where the plasma density is expected to be greater (Figure 2.2, top). Some of the asymmetry may further be caused by ion gyroradius effects. The peaks at m/q =32 and 28 are consistent with O_2^+ and Si^+, respectively, which can be produced by dissociative ionization of silica. Another peak at m/q = 32 may be S^+, as earlier predicted [*Sprague et al.*, 1995]. The Mg^+ (m/q = 24) at Mercury's exosphere is consistent with the identification of Mg-rich pyroxene in Mercury surface materials [*Sprague and Roush*, 1998].

The spatial distribution of species within the ionized exosphere reflects the large-scale structure of Mercury's magnetosphere. Heavy ions (masses between 10 and 50 amu) are most abundant near Mercury's surface, between local midnight and dawn (Fig. 2). When ionized, they are quickly accelerated by electric fields expected near the planet toward the nightside surface [*Delcourt et al.*, 2003]. This process contributes to the recycling of exospheric constituents and to the dawn enhancement of Na and K in the exosphere and inhibits the loss of material to the interplanetary medium [*Sprague*, 1992]. Molecular ion species, such as H_2O^+ and H_2S^+ observed by FIPS, are probably associated with chemical sputtering of the surface [*Potter*, 1995] or sputtering of cold-trapped ices.

Acknowledgements: The MESSENGER project is supported by the NASA Discovery Program under contracts NAS5-97271 to the Johns Hopkins University Applied Physics Laboratory and NASW-00002 to the Carnegie Institution of Washington.

Chapter 3

MESSENGER Observations of the Plasma Environment Near Mercury

This chapter is taken from Jim M. Raines, James A. Slavin, Thomas H. Zurbuchen, George Gloeckler, Brian J. Anderson, Daniel N. Baker, Haje Korth, Stamatios M. Krimigis, Ralph L. McNutt, Jr. (2011), MESSENGER observations of the plasma environment near Mercury, *Planet. Space Sci.*, *59*, 2004-2015.

Abstract

The MESSENGER Fast Imaging Plasma Spectrometer (FIPS) measured the bulk plasma characteristics of Mercury's magnetosphere and solar wind environment during the spacecraft's first two flybys of the planet on 14 January 2008 (M1) and 6 October 2008 (M2), producing the first measurements of thermal ions in Mercury's magnetosphere. In this work, we identify major features of the Mercury magnetosphere in the FIPS proton data and describe the data analysis process used for recovery of proton density (n_p) and tempefrature (T_p) with a forward modeling technique, required because of limitations in measurement geometry. We focus on three regions where the magnetospheric flow speed is likely to be low and meets our criteria for the recovery process: the M1 plasma sheet and the M1 and M2 dayside and nightside boundary-layer regions. Interplanetary magnetic field (IMF) conditions were substantially different

between the two flybys, with intense reconnection signatures observed by the Magnetometer during M2 versus a relatively quiet magnetosphere during M1. The recovered ion density and temperature values for the M1 quiet-time plasma sheet yielded $n_p \sim$ 1-10 cm^{-3}, $T_p \sim 2 \times 10^6$ K, and plasma $\beta \sim 2$. The nightside boundary-layer proton densities during M1 and M2 were similar, at $n_p \sim$ 4-5 cm^{-3}, but the temperature during M1 ($T_p \sim$ 4-8 $\times 10^6$ K) was 50% less than during M2 ($T_p \sim 8 \times 10^6$ K), presumably due to reconnection in the tail. The dayside boundary layer observed during M1 had a density of ~16 cm^{-3} and temperature of 2×10^6 K, whereas during M2 this region was less dense and hotter ($n_p \sim 8$ cm^{-3} and $T_p \sim 10 \times 10^6$ K), again, most likely due to magnetopause reconnection. Overall, the southward interplanetary magnetic field during M2 clearly produced higher T_p in the dayside and nightside magnetosphere, as well as higher plasma β in the nightside boundary, ~20 during M2 compared with ~2 during M1. The proton plasma pressure accounts for only a fraction (24% for M1 and 64% for M2) of the drop in magnetic pressure upon entry into the dayside boundary layer. This result suggests that heavy ions of planetary origin, not considered in this analysis, may provide the "missing" pressure. If these planetary ions were hot due to "pickup" in the magnetosheath, the required density for pressure balance would be an ion density of ~ 1 cm^{-3} for an ion temperature of ~ 10^8 K.

3.1 Introduction

The Fast Imaging Plasma Spectrometer (FIPS) [*Zurbuchen et al.*, 1998; *Andrews et al.*, 2007] is part of the MErcury Surface, Space ENvironment, GEochemistry, and Ranging (MESSENGER) instrument payload [*Solomon et al.*, 2007]. Its purpose is to determine the plasma properties and abundances of elements in Mercury's space

environment, which have important implications for the composition of the planet's surface materials. Planetary ions are thought to be created primarily by the interaction of solar radiation and solar wind ions with Mercury's atmosphere and surface [*Zurbuchen et al.*, 2008]. The FIPS investigation has already reported the first measurements of planetary ion composition at Mercury taken during the first flyby of Mercury (M1) by MESSENGER on 14 January 2008 [*Zurbuchen et al.*, 2008]. FIPS also obtained on-board energy spectra and directional information for H^+ during the first and the second flybys, the latter of which (M2) took place on 6 October 2008. Detailed analysis of these H^+ energy spectra is complicated by the placement of the FIPS sensor relative to other elements of the spacecraft, including a sunshade, that collectively limit the instrument's field of view (FOV) to directions transverse to the Mercury–Sun axis. For this reason the FIPS FOV seldom includes the plasma flow direction as required by standard plasma moment computations. Here we report a new algorithm developed to derive bulk plasma parameters from these H^+ energy spectra, and we discuss their implications for the physical processes that govern Mercury's magnetosphere.

MESSENGER has confirmed and extended the earlier Mariner 10 measurements of Mercury's small, ~250 nT-R_M^3, intrinsic magnetic field, where R_M is Mercury's radius [*Anderson et al.*, 2008; 2010]. The resulting magnetosphere is much smaller than Earth's, by about a factor of 8, but qualitatively similar in terms of its overall structure [*Russell et al.*, 1988; *Slavin*, 2004; *Baumjohann et al.*, 2006; *Fujimoto et al.*, 2007]. Mercury's magnetosphere is immersed in the supersonic heliospheric plasma, which is up to ten times stronger and more variable than the solar wind at Earth, mostly due to Mercury's closer distance from the Sun [*Marsch et al.*, 1982]. These strong and variable

heliospheric flows, coupled with the relatively small size of the magnetosphere, cause some important and unexpected magnetospheric properties compared to their counterparts in Earth's magnetosphere.

In order to place the MESSENGER measurements into a broader context of solar and inner heliospheric conditions, the MESSENGER team has carried out an extensive set of modeling runs with the Wang-Sheeley-Arge (WSA) ENLIL model [*Baker et al.*, 2009; 2011; and references therein]. This three-dimensional magnetohydrodynamic code uses the Wang-Sheeley-Arge approximation for the corona and then propagates the solar wind out through the inner heliosphere. It has been used by to predict the plasma and interplanetary magnetic field properties near the MESSENGER spacecraft during the Mercury encounters. The forecasted average solar wind proton densities were the same during both M1 and M2, ~ 60 cm^{-3}. Bulk solar wind speeds were similar, 420 km/s during M1 and 380 km/s during M2, though the predicted temperature during M1, 1.2×10^5 K. was substantially lower than the 2.0×10^5 K forecast for M2 [*Baker et al.*, 2009; 2011].

The first MESSENGER flyby measurements showed that Mercury's magnetosphere is immersed in a cloud of planetary ions that extends beyond the dayside bowshock and revealed the existence of a "boundary layer" of indeterminate origin at the inner edge of the plasma sheet and just inside the dawn magnetopause [*Anderson et al.*, 2008; *Slavin et al.*, 2008a; *Zurbuchen et al.*, 2008]. The MESSENGER trajectory during both flybys, along with model bowshock and magnetopause positions, is shown in Figure 3.1. [The reader is referred to Figure 1 of *Slavin et al.* (2008a) for a more detailed diagram of Mercury's magnetospheric structure.] This boundary layer was identified on the basis of

sudden decreases in the magnetic field that are almost certainly diamagnetic in origin and, therefore, should be associated with commensurate increases in the plasma pressure, needed to maintain stress balance. The second flyby confirmed the existence of this dayside boundary layer as a stable feature of Mercury's magnetosphere [*Anderson et al.*, 2010; *Slavin et al.*, 2009a]. Further, the second flyby took place during a period of southward interplanetary magnetic field (IMF), in contrast to the steady northward IMF observed during M1. Consistent with these IMF conditions, M2 observations revealed very intense magnetic reconnection at the dayside magnetopause and in the magnetic tail [*Slavin et al.*, 2009a].

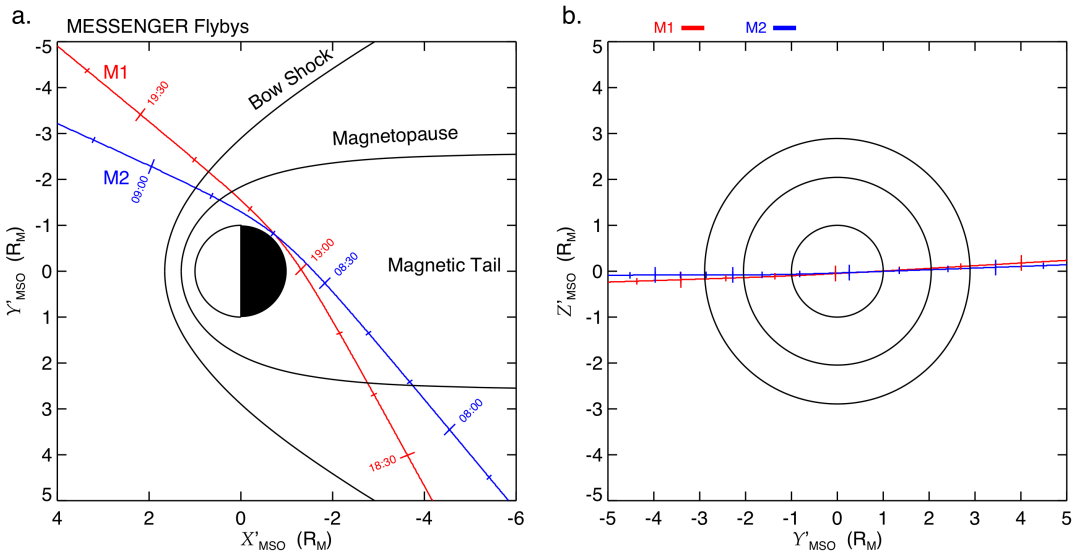

Figure 3.1. The MESSENGER trajectories during M1 and M2, as well as model positions of the bowshock and magnetopause. Coordinates shown are aberrated Mercury solar orbital (MSO) coordinates. This system is similar to MSO coordinates (see text) except that the X'_{MSO} and Y'_{MSO} coordinates are rotated clockwise by 7° from the solar direction to account for average aberration of the solar wind vector due to Mercury's orbital velocity. Details of the models can be found in *Slavin et al.*, (2009b).

A second region of sudden magnetic field decrease was identified in both flybys, in the inner magnetosphere directly behind the planet (as seen from the Sun) where the magnetic field is strongly northward [*Anderson et al.*, 2008, 2010; *Slavin et al.*, 2008a,

2009a]. One possible explanation of this nightside diamagnetic depression is that it was due to the presence of a flow-braking region, where flux tubes convecting toward the planet run into the planetary dipole magnetic field and slow to near stagnation. In this scenario, the flow slows (i.e., "brakes") due to the adiabatic compression and heating of the plasma-sheet plasma as the closed magnetic flux tubes decrease in volume during convection toward the planet [*Erikson and Wolf*, 1980]. At Earth, flow braking is typically observed where the magnetic field transitions from tail-like to dipolar in configuration, with an associated average increase in field strength of 6.7 nT [*Shiokawa et al.*, 1997]. We refer to this region hereafter as the nightside boundary layer.

To analyze the plasma properties of these regions, we developed a method for deriving H^+ bulk parameters from the FIPS energy spectra that relies on the assumption that the thermal speed (v_{th}) of the H^+ ions is large compared to the bulk flow speed (v_{bulk}). Such an assumption allows the computation of proton density (n_p) and temperature (T_p) from our observations, as long as a general shape of the plasma velocity distributions is assumed. Here, the velocity distribution functions (described below) are assumed to follow a simple convected Maxwellian distribution. We focus on times when the direction of the magnetic field is largely perpendicular to the Mercury–Sun line during which plasma convection speeds are often low and within the range of our assumptions. One such region is the central plasma sheet where the magnetic field is largely northward, the plasma is very hot (~10^6 – 10^7 K), and the velocity distribution functions (VDFs) are observed at Earth to be well modeled as convected Maxwellian distributions [*Raj et al.*, 2002; *Mukai et al.*, 2004]. Further, the magnetic field measurements from the first flyby indicate that MESSENGER entered the magnetosphere through the dusk

plasma sheet and that it remained in that region until it encountered strong dipolar magnetic fields closer to the nightside of the planet [*Slavin et al.*, 2008a]. The northward interplanetary magnetic field during the first flyby and resulting quiet magnetosphere also suggest that plasma convection speed within the equatorial magnetosphere should have been no more than a few tens of kilometers per second, under the assumption that the quiet-time magnetospheric electric potential is ~ 10% of the convection electric potential applied by the solar wind to the magnetosphere as a whole for predicted conditions [*Slavin et al.*, 2009b]. In contrast, the utility of the parameter determination approach described here is less applicable to the second flyby because MESSENGER entered the tail through the southern lobe [*Slavin et al.*, 2009a]. Here the magnetic field is largely parallel to the Mercury–Sun line and the tenuous plasma of the plasma mantle [*Rosenbauer et al.*, 1975] streams in the anti-sunward direction nearly parallel to the magnetic field and slowly drifts toward the plasma sheet, under the combined influence of the convective electric field **E** and the magnetic field **B**, as an $\mathbf{E} \times \mathbf{B}$ drift. As noted earlier, the IMF during M2 was southward and conducive to reconnection, increasing the likelihood of fast plasma convection speeds ($v_{bulk} \sim v_{th}$) in the equatorial magnetosphere [*Slavin et al.*, 2009a].

Our method for bulk parameter determination may also be applicable to the dayside and nightside boundary layers. If these regions of depressed magnetic field are due to the presence of slowly moving, hot plasma, as suggested by recent simulations [*Trávníček et al.*, 2009; *Benna et al.*, 2010], then the underlying assumptions of our forward model recovery should hold. Most importantly, the FIPS plasma parameters determined here

should account for the "missing" plasma pressure to bring the adjacent magnetospheric regions into pressure equilibrium [*Anderson et al.*, 2008; *Slavin et al.*, 2009a,b].

We first provide an overview of FIPS H^+ plasma measurements for the two flybys, and we identify macroscopic features of Mercury's plasma environment, including bow shock and magnetopause as well as the magnetotail plasma sheet and lobe. We outline the recovery of the physical parameters from the measured data; an Appendix describes in detail procedures devised to recover proton density (n_p) and temperature (T_p) through use of a software instrument model that includes the time-dependent instrument field of view, as well as spacecraft position and velocity. Finally, from this information we discuss the plasma parameters recovered from three regions and their implications for Mercury's magnetospheric structure and dynamics.

3.2 Description of Measurements

3.2.1 General characteristics

The FIPS sensor measures energy per change (*E/q*), time of flight, and incident angle for ions with *E/q* in the range 0.05–13 keV e^{-1} and with mass per charge (*m/q*) from 1 to 60 amu e^{-1}. As configured for both flybys, FIPS completed one scan over the full range of *E/q* values every 8 s. FIPS has a very large instantaneous and conical FOV of approximately 1.4π sr, with an approximate angular resolution of 15° throughout the entire FOV and two symmetric cutouts of 15° near the instrument's symmetry axis and also near the plane perpendicular to the symmetry axis. The incident direction of any particle is derived through a two-dimensional imaging process. Only energy-integrated angular distributions were obtained because of the specific operational mode used for M1 and M2 (a mode that has since been modified). FIPS was placed on the spacecraft to

maximize collection of heavy ions from the surface and space environment, within important thermal constraints. To protect the spacecraft from overheating, the Sun must be kept within a Sun keep-in zone. The spacecraft sunshade is therefore pointed at the Sun at all times, even in the shadow of the planet. This means that the FOV within 12° of the Sun-spacecraft vector is obstructed at all times. From a point of view on the spacecraft behind the sunshade, the FIPS boresight vector (FOV center) essentially points through the middle of the lower left octant of a three-dimensional coordinate system centered on the spacecraft (Figure 3.2A). The FOV extends from directly behind the sunshade to up to 45° to the rear. This orientation causes ~30% of the FIPS FOV to be obstructed by the MESSENGER sunshade at all times. An additional fraction of the FOV is obstructed by one of the two solar panels, which is subject to changes in orientation (Figure 3.2B). Neither the anti-sunward direction nor the sunward direction is ever directly within the FIPS FOV.

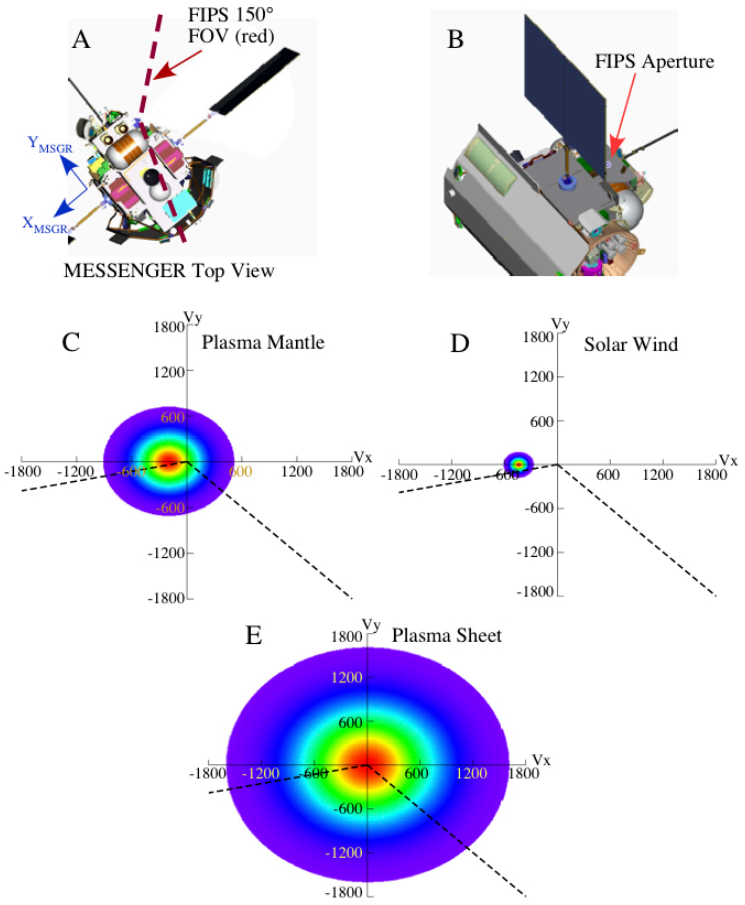

Figure 3.2. FIPS spacecraft placement, field of view, and obstructions. (A) A top-down view of the MESSENGER spacecraft, with the full 150° FOV shown by red dashed lines. The MESSENGER spacecraft axes, X_{MSGR} and Y_{MSGR}, are shown on the far left. (B) A view approximately down the FIPS boresight vector, the sensor symmetry axis, with various spacecraft structures evident. From these two views, the obstruction of the FIPS FOV by the spacecraft body, sunshade, and one solar panel is apparent. (C-E) Representations of the FIPS FOV in velocity space. The relative numbers of particles with a given set of velocity coordinates is shown by color, where red indicates the most particles and purple the least. The dark red core extends to approximately v_{th}. Hot, convecting plasma, representing the magnetospheric plasma mantle is shown in (C). A typical solar wind distribution (Mach = 8) is shown in (D). This panel shows graphically that a solar wind distribution, cold and with a large convection velocity, is not typically within the FIPS FOV while MESSENGER is in the solar wind. (E) Plasma sheet conditions; it is under these conditions that the recovery method presented in this paper is most applicable. Velocity coordinate axes follow the MSO coordinate system, described in the text.

FIPS uses a double coincidence technique for time-of-flight measurements, which very effectively reduces most spurious background noise [*Andrews et al.*, 2007]. However, low-level noise signals ("dark counts") persist in the data and have been analyzed during MESSENGER's heliospheric cruise phase. These background counts

occur at a rate of approximately 1 count per 10 s and can affect the interpretation of very low-flux ions, such as magnetospheric heavy ions [*Zurbuchen et al.*, 2008], but they do not substantially affect the proton observations described here, which have fluxes that exceed these backgrounds by several orders of magnitude. A detailed analysis of heavy ions during all three MESSENGER flybys of Mercury will be published elsewhere and is beyond the scope of this paper.

3.2.2 Data analysis process

The FIPS FOV limitations must be addressed in the context of the region of velocity space [*Gurnett and Bhatacharjee*, 2005] accessible to the instrument. Figures 3.2C-E show representations of three different plasma distributions in velocity space, with an example FIPS FOV overlaid. These velocity distributions show by color coding the relative numbers of particles with a given set of velocity coordinates. Velocity coordinates are oriented according to the Mercury solar orbital (MSO) coordinate system. In the MSO system, the X_{MSO} axis points from Mercury to the Sun and the Z_{MSO} axis points northward, orthogonal to Mercury's orbital plane. The Y_{MSO} axis is orthogonal to the other two and oriented according to a right-handed coordinate system. Because V_x is positive toward the Sun (like X_{MSO}), plasma flowing from the Sun or down the magnetotail (away from Mercury) has a negative velocity. In Figure 3.2C, a hot distribution is shown convecting along the V_x axis, which is representative of typical magnetospheric plasma. The fact that the core (center) of the distribution is not within the FOV makes the interpretation of measurements of such a distribution ambiguous. Figure 3.2E shows a distribution at higher temperature that is quasi-stagnant (i.e., $v_{th} >> v_{bulk}$) and thus centered close to the origin. In this case, a partial measurement of the

distribution can be interpreted in a straightforward fashion due to the symmetry of the problem. Plasma in this type of distribution is typical of that found throughout a magnetospheric central plasma sheet (CPS) under quiet conditions and at the inner edge of the CPS (where ion flow speed decreases and heating takes place) under most conditions. Finally, Figure 3.2D shows a representation of a supersonic and convecting plasma distribution, reminiscent of solar wind measurements by FIPS. Clearly, the 12° blockage noted previously has a major impact in this case and prevents complete measurements of such distributions under most conditions.

An overview of proton and magnetic field measurements during the first two Mercury flybys, as well as the respective FIPS orientations, is shown in Figure 3.3. MESSENGER's third Mercury flyby on 29 September 2009 did not yield observations through the entire encounter due to a spacecraft safe-hold event that terminated science instrument observations shortly before closest approach [*Slavin et al.*, 2010]. We do not consider FIPS M3 observations further in this paper.

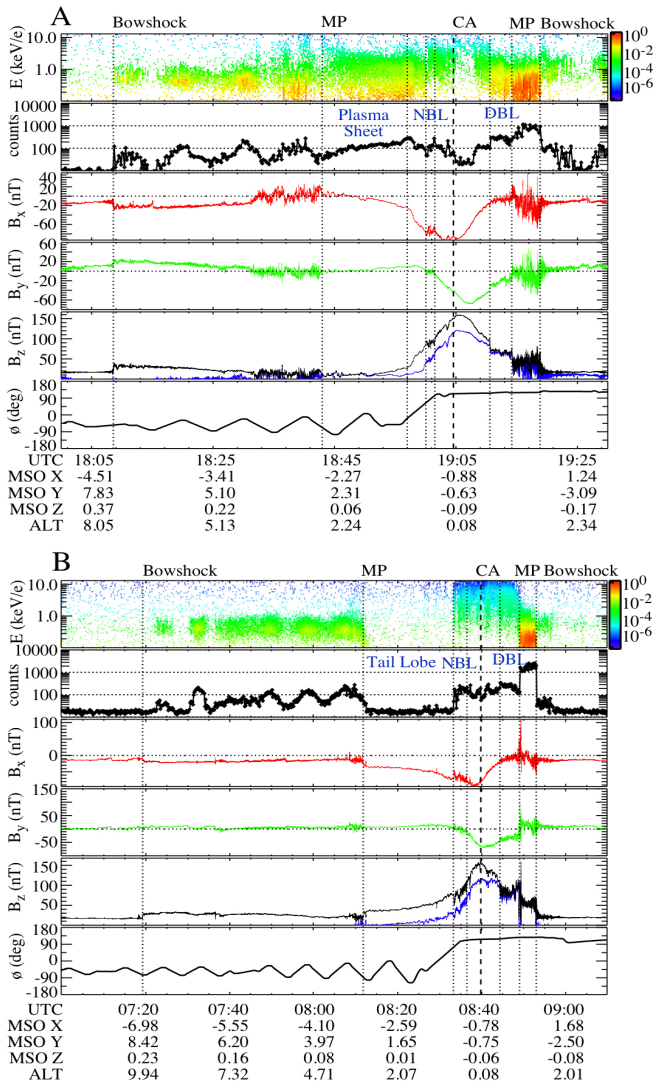

Figure 3.3. Data overview for (A) M1 and (B) M2. Each figure includes a proton energy spectrogram (top panel), total proton counts (second panel), three components of the magnetic field (red, green, and blue, panels three to five), and the total magnetic field (black, panel five). The color scales in the proton energy spectrograms are set to show detail in the respective measurements and are not the same for (A) and (B). Relative changes in intensity can be estimated from the total proton counts. Lines delimit the bowshock crossings, magnetopause (MP) crossings, and position of closest approach (CA). Nightside and dayside boundary layers are identified as NBL and DBL, respectively. Panel 6 gives the angle (φ) between the FIPS boresight vector and the Y_{MSO} axis. Time of the measurements (in UTC), spacecraft position in MSO coordinates, and spacecraft altitude (both in units of Mercury radii) are given on the horizontal axis. See text for description of MSO coordinate system and further details.

During M1, proton counts were low before crossing into the magnetosphere, due to the obstruction of the solar wind by the sunshade (as in Figure 3.2D). Once MESSENGER crossed the inbound bow shock, alternating regions of high and low

proton counts became evident. These correspond to partial rotations around one spacecraft axis, Y_{MSGR} (see Figure 3.2A for the spacecraft, or MSGR, coordinate system), which enabled the Ultraviolet and Visible Spectrometer sensor on the Mercury Atmospheric and Surface Composition Spectrometer instrument [*McClintock and Lankton*, 2007] to view the neutral sodium tail of the planet. The orientation of the spacecraft is indicated in the bottom panel, where the clock angle (φ) between the FIPS boresight vector (projected onto the $Y_{MSO} - Z_{MSO}$ plane) and the $-Y_{MSO}$ axis is plotted. FIPS counts peak when these vectors are aligned and thus the angle is nearest zero. These data are a good example of the pronounced FOV effects on plasma measurements of high-Mach-number magnetospheric flows (Figure 3.2C). Once the spacecraft crossed the inbound magnetopause and entered the magnetosphere, the counts elevated and spread out in energy, consistent with the higher temperatures expected in the central plasma sheet [*Slavin et al.*, 2008]. Furthermore, the orientation dependence disappeared, also consistent with expected higher temperatures and the much broader velocity distribution that results (as in Figure 3.2E). These features remained qualitatively similar until the point of closest approach to the planet. Just after closest approach, proton counts again decreased, and precipitously so, as the spacecraft passed into the dayside magnetosphere, where very low densities should be expected. Proton counts returned quickly when MESSENGER entered the dayside boundary layer. Once the spacecraft passed the outbound magnetopause, crossing into the Mercury magnetosheath, proton counts showed an order-of-magnitude increase. This jump is expected for two reasons: First, this crossing of the magnetosheath is on the dayside, so density is expected to be high, several times the solar wind density. Second, the streamlines of the solar wind in

the magnetosheath follow the shape of the magnetopause and provide the closest alignment of flow direction and FIPS boresight during these flybys [*Spreiter et al.*, 1966].

Markedly different proton fluxes were measured during M2 (Figure 3.3B). Because the spacecraft entered through the southern lobe, the count rates were very low from the magnetopause crossing until nearly 08:33 UTC, when MESSENGER reached the inner edge of the tail [*Slavin et al.*, 2009a]. When counts increased again upon entry into the nightside boundary layer, the plasma was much hotter than during M1, as counts were spread through a large *E/q* range, 0.3–13 keV e^{-1}, nearly the entire *E/q* range seen during the flyby. Because MESSENGER passed through the plasma lobe while in the magnetotail, the plasma sheet was not observed during M2. The FIPS count rate became variable through closest approach, increasing again as the spacecraft reached the dayside boundary layer [*Anderson et al.*, 2010], finally increasing markedly in the outbound magnetosheath, as was observed during M1.

Close-up views of the boundary layers are shown in Figure 3.4. These can be seen clearly as regions where changing magnetic field magnitude leveled out and variation increased. The magnetic field dropped substantially upon entry into the dayside boundary layer; the particularly pronounced drop during M1 was described by *Slavin et al.*, [2008] as a "double magnetopause."

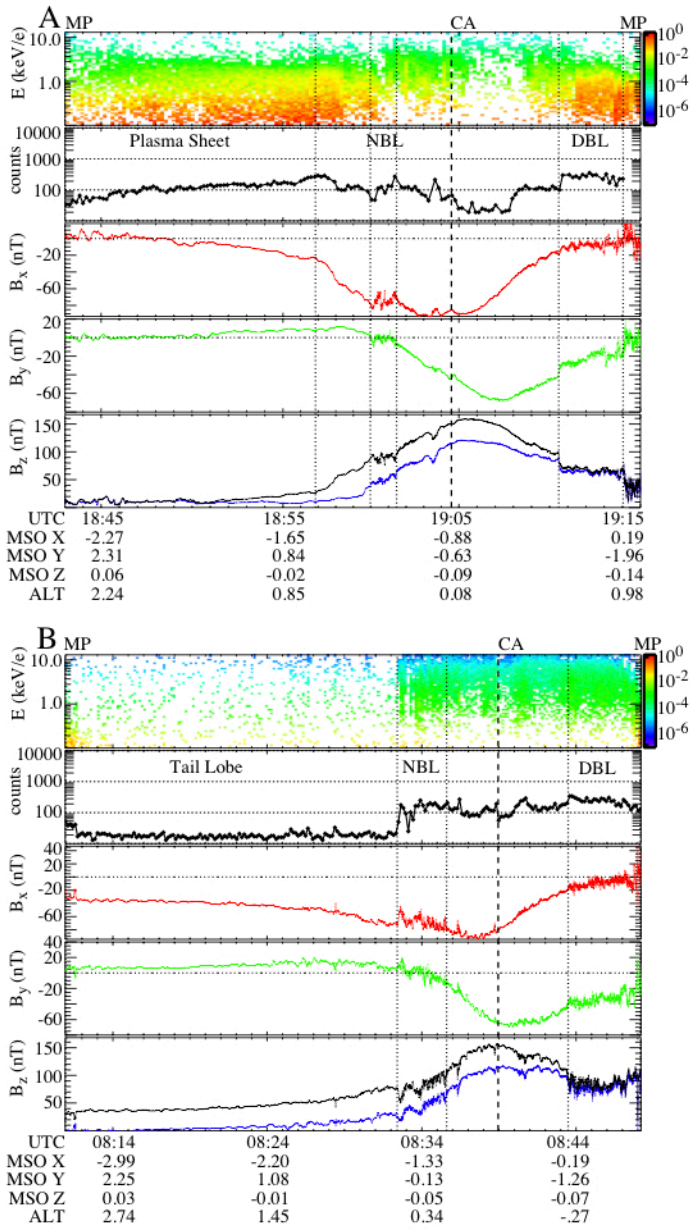

Figure 3.4. Close-up views of boundary-layer regions during (A) M1 and (B) M2. See Figure 3.3 for other information.

3.3 Results and Discussion

To compute the plasma moments in specific physical regimes of the data shown in Figure 3.3, we use a forward modeling approach [e.g., §1.3 of *Tarantola*, 1987] to determine basic plasma moments (density, bulk velocity, and temperature). We take this

approach because of the various FOV and pointing limitations already mentioned, rather than calculate the moments directly from observed data.

The method we use is conceptually straightforward. First, we create a set of modeled measurements that are characterized by specific plasma moments. Then, we compare each of these models to actual measurements to find the combination of moments that best explains the FIPS observations of a given distribution function. The details of this process, specific and relevant examples for such a moment calculation, and the density calibration process are described in the Appendix.

We focus on plasma parameters from three regions, where the assumptions discussed in the Appendix most likely hold: the central plasma sheet (CPS), the nightside boundary layer, and the dayside boundary layer. Temperatures and pressures were calculated from the recovered values for n_p and v_{th} using standard definitions.

The resulting plasma moments for Mercury's CPS during M1 are shown in Figure 3.5, in conjunction with magnetic field measurements and geometrical information. In general, the density grew steadily as MESSENGER approached Mercury, from <1 cm^{-3} at -2.33 R_M to ~12 cm^{-3} at -1.59 R_M. The temperature was relatively steady at ~ 2×10^6 K, with occasional, sometimes sudden, enhancements. A comparison of fluctuations in density and temperature shows that increases in one of these values was often coincident with decreases in magnetic field intensity, as expected under pressure balance.

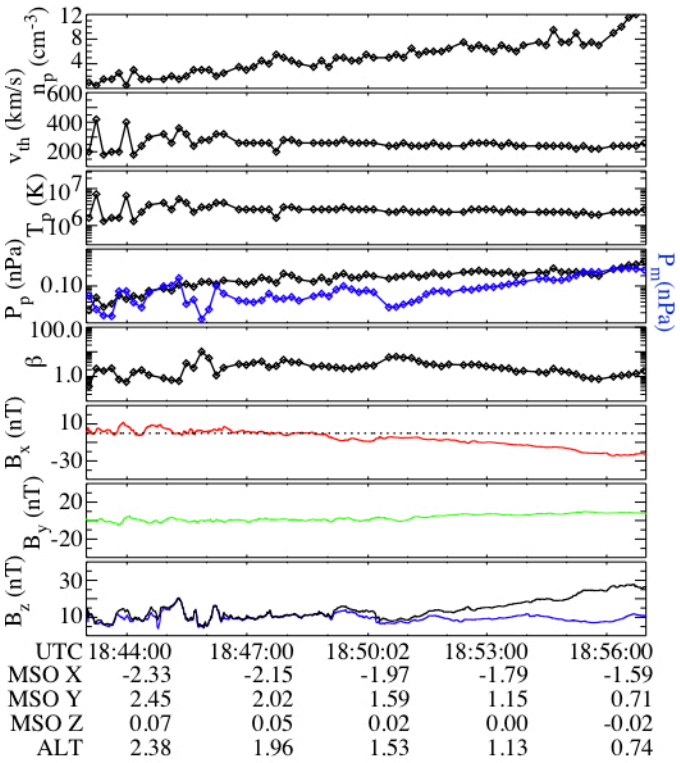

Figure 3.5. Recovered plasma parameters for the plasma sheet during M1. Density (n in cm^{-3}) and thermal velocity (v_{th} in km s^{-1}) are recovered as described in the text. Temperature (T in K) and proton plasma pressure (P_P in *nPa*) are calculated from n and v_{th}. Magnetic pressure (P_M, blue line) is shown with proton plasma pressure. Magnetic field components are as measured by the MESSENGER Magnetometer and given in MSO coordinates. Field magnitude is shown in the bottom panel (black line).

For comparison, we examined average values for the central plasma sheet at Earth reported by *Baumjohann and Paschmann* (1989). In that study, a large volume of observations was surveyed, spanning a range of magnetospheric conditions and positions in the plasma sheet. Those workers found an average plasma velocity of ~50-75 km s^{-1}. Furthermore, flows over 300 km s^{-1} occurred in < 3% of cases and typically lasted less than 1 min (< 3% lasted longer than 100 s). This velocity range, if also present at Mercury, is consistent with the assumptions of our recovery method (Appendix), especially when the IMF is northward and the magnetosphere is quiet. That terrestrial study also yielded average densities of ~0.2–0.5 cm^{-3}. By comparison, the recovered density for the full plasma sheet during M1 ranged from 1 to 12 cm^{-3}, considerably larger

than the average at Earth. However, the FIPS densities span the typical plasma sheet density of ~1 cm^{-3} reported at Mercury by *Ogilvie et al.*, (1977) from available Mariner 10 electron measurements. Those workers argued that the density in planetary magnetospheres may scale with the solar wind density as $1/r^2$, where r is solar distance. This radial scaling works out to approximately a factor of 10 greater for Mercury than for Earth. In this light, the recovered FIPS plasma sheet densities are approximately consistent with this scaling law. Further, strong, steady northward IMF is known at Earth to produce substantial increases in plasma sheet density and reductions in temperature [see *Terasawa et al.*, 1997]. The temperature of the Mercury plasma sheet is considerably lower than seen at Earth, ~ 2×10^6 K compared to ~$(30\text{-}56) \times 10^6$ K. At Earth, the plasma β, the ratio of plasma pressure to magnetic pressure, was found to vary greatly, from 20 to 30 near the inner edge of the CPS to 0.3 at the outer edge. We found the plasma β in the Mercury quiet-time CPS to be more steady, averaging ~2, but within the range reported for Earth. These differences may be due to the wide range of conditions surveyed by *Baumjohann and Paschmann* [1989], which included cases with both northward and southward IMF. The proton pressure increased by about a factor of 2 as MESSENGER approached the planet. This trend is certainly consistent with observations at Earth [*Shiokawa et al.*, 1997].

We now consider the two passages through the nightside boundary-layer region. The recovered plasma parameters, as well as calculated temperature and pressure, for this region are shown along with magnetic field data in Figure 6. Average values are shown in Table 3.1. Also in Table 3.1 is the magnetic pressure drop on entry into the dayside boundary layer, calculated by averaging the magnetic field for 20 s before and after the

transition into the layer. In addition to the magnetic field signature, a shift to higher mean energy is apparent in the energy spectra, especially during M1 (Figure 3.4), indicating a higher mean proton temperature. During M1, density in the nightside boundary steadily increased again as the distance to the planet decreased, as evident in Figure 3.6A. This trend was less pronounced than in the quiet-time CPS, but that region was larger and thus there are more observations to show a trend. The temperature was not as steady as the CPS during M1.

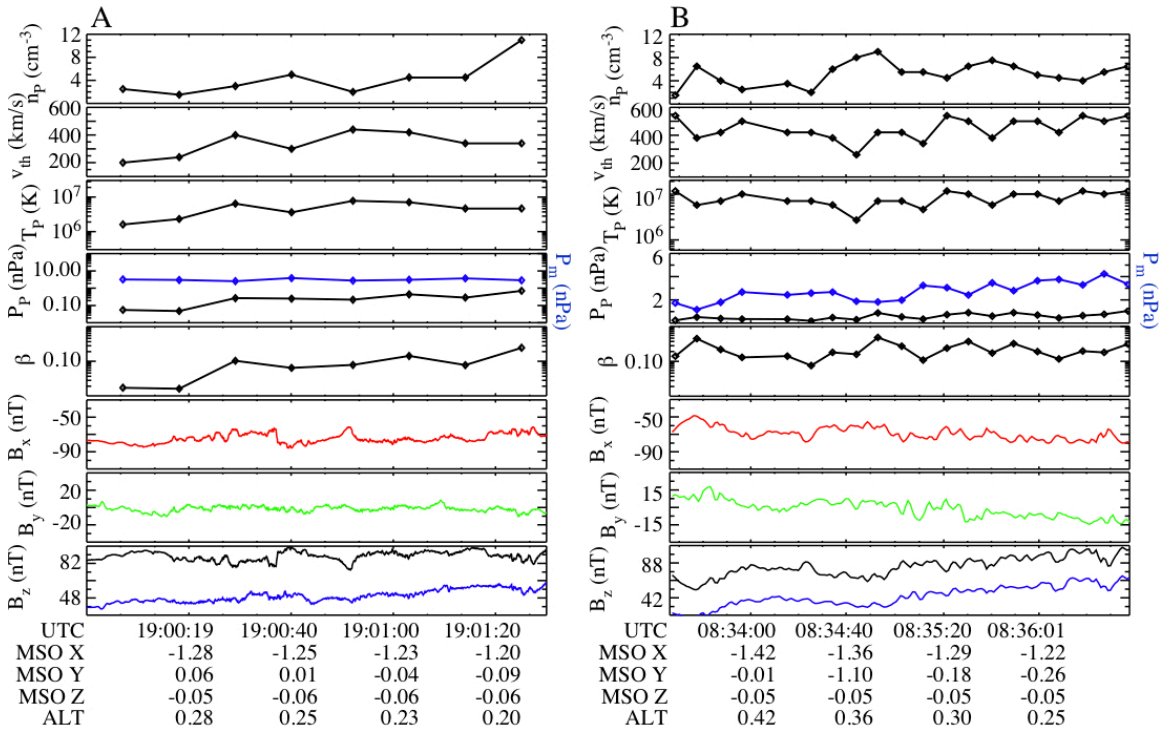

Figure 3.6. Recovered plasma parameters for the nightside boundary layer during (A) M1 and (B) M2. See Figure 3.5 for other details.

Table 3.1. Comparison of average plasma parameters.

	Dayside Boundary Layer		Nightside Boundary Layer	
Flyby	M1	M2	M1	M2
$\langle n \rangle$	16	8	4.3	5.2
$\langle T \rangle$	1.7×10^6	9.3×10^6	4.8×10^6	8.2×10^6
$\langle P_P \rangle$	0.38	1.02	0.28	0.56
$\langle P_M \rangle$	1.9	3.01	3.1	2.7
ΔP_M	-1.63	-1.61	n/a	n/a
$\langle \beta \rangle$	0.2	0.4	0.1	0.2
$\langle \lvert B \rvert \rangle$	69.1	86.6	88.4	81.4

Notes: the "< >" brackets denote averages of values through the layer; P_P is proton pressure (*nPa*), P_M is magnetic pressure (*nPa*) and ΔP_M is the change in P_M upon entry into the layer.

Results for the nightside boundary layer during M2 are shown in Figure 3.6B. No clear trend in temperature with altitude is evident, and there were many more density fluctuations. The temperature during M2 was nearly a factor of 2 larger than during M1. Likewise, plasma β during M2 was 2 times that during M1. For both crossings of the nightside boundary layer, a correlation is still evident between depressions in magnetic field magnitude and increases in n_p or T_p, more pronounced during M2 because of the higher variability. The higher temperature, β, and variability are consistent with the more active magnetosphere observed during M2, driven by increased reconnection due to southward IMF. The nightside boundary layer is therefore consistent with the braking of fast sunward flow as it approaches the planet. If measurements from orbit confirm flow braking at the inner edge of Mercury's tail, such a situation would provide an important

opportunity to study aspects of the near-Earth neutral line model of substorms in two magnetospheres that are in some ways similar yet in others very different [see *Slavin et al.*, 2009a, 2010].

The full set of plasma parameters recovered for the dayside boundary layer transits during M1 and M2 are shown in Figure 3.7, and average values are listed in Table 3.1. During M1, the density was steady at 20 cm^{-3}, considerably higher than the density in the nightside boundary layer. Temperature showed a steady decrease by about a factor of 2 as MESSENGER passed into the flank magnetosheath at the end of this region. As with the nightside boundary layer, the dayside boundary layer was more variable during M2 than it was during M1. Of particular note is the fact that T_p dropped precipitously near the end of the layer while n_p increased substantially, both as the spacecraft approached the outbound magnetopause. This behavior may indicate that magnetosheath plasma, expected to be cooler and denser, was penetrating into the magnetosphere and would be consistent with the observations of a large normal (to the magnetopause) magnetic field component [*Slavin et al.*, 2009a; *Anderson et al.*, 2010]. Plasma β was again substantially higher during M2, by a factor of ~2. In contrast, average density was also 2 times lower during M2 than M1, 8 versus 16 cm^{-3}. The existence of this boundary layer is consistent with the simulation results, which show an annular disk of increased plasma density around the planet [*Benna et al.*, 2010; *Trávníček et al.*, 2010], but additional measurements and modeling are required.

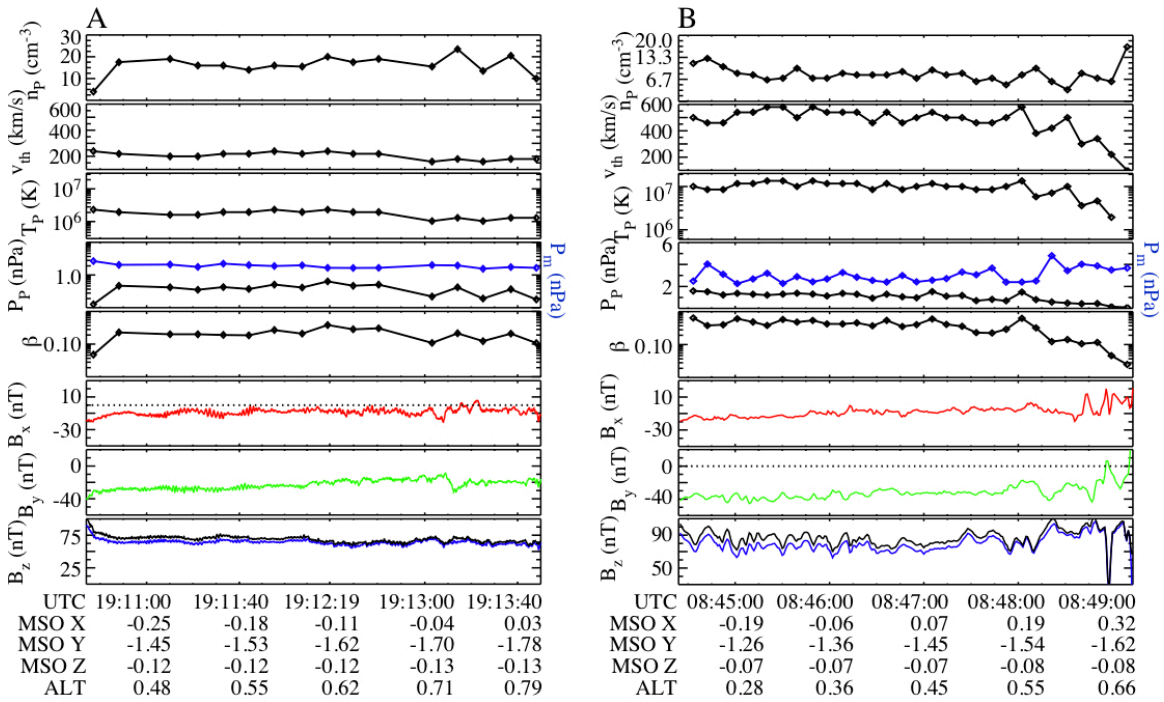

Figure 3.7. Recovered plasma parameters for the dayside boundary layer during (A) M1 and (B) M2. See Figure 3.5 for other details.

A strong drop in magnetic field strength was evident during both flybys when the spacecraft was passing into the dayside boundary layers. In both cases, the magnetic pressure drop was about 1.6 nPa, but the pressure due to protons within the boundary layer was only 0.4 nPa during M1 and 1.0 nPa during M2. Proton plasma pressure does not account for full magnetic-pressure drop upon entering the layers, even including a density uncertainty of 20%. Of course, it is possible that protons in this layer violate the assumptions of our recovery method, which could cause the observed density to be lower than the actual density. This explanation cannot be ruled out. However, an alternative explanation for the missing pressure is planetary ions [*Zurbuchen et al.*, 2008]. *Slavin et al.*, [2009a] suggested that planetary neutrals could be photo-ionized in the fast magnetosheath flow at the flanks of the magnetosphere. These ions would be quite energetic and penetrate about 1 gyro-radius inside of the magnetopause. These planetary

ions would not yet be thermalized and would occupy a non-Maxwellian velocity distribution [*Delcourt et al.*, 2003], possibly with velocities clustered in a narrow ring in velocity space, offset at the speed of the tailward convection. If we assume that their thermal velocity is comparable to the local magnetosheath flow speed of 300 km s^{-1}, we can estimate that the equivalent temperature would be approximately 8.3×10^7 K for Na^+. For M1 and M2 an estimated density of ~1 cm^{-3} Na^+ ions would be required to make up the missing pressure.

3.4 Conclusions

We have developed a method for recovering n_p and T_p from MESSENGER's Mercury flyby plasma observations under the constraints of $v_{th} >> v_{bulk}$ and isotropic Maxwellian distribution functions. This method has yielded the first plasma parameters derived from Mercury's magnetosphere, including the quiet-time central plasma sheet, a nightside boundary layer in the inner magnetosphere, and a dayside boundary layer near the dayside magnetopause. The recovered plasma density, temperature, and pressure values are relatively consistent with expectations from measurements at Earth and the plasma electron measurements by Mariner 10. They show marked differences between the two flybys, supporting the conclusion that Mercury's magnetosphere responds strongly to IMF direction. Density and pressure variations compare favorably with observations at Earth and are consistent with the highly active magnetosphere observed previously during M2 [*Slavin et al.*, 2009a]. In particular, the southward IMF during M2 clearly produced notably higher temperatures in the dayside and nightside magnetosphere, consistent with increased reconnection. Furthermore, detailed comparison of the magnetic pressure drop on entering the dayside boundary layer during both encounters

shows that proton pressure does not account for a substantial portion of that pressure drop. The remaining pressure may be the result of heavy planetary ions not included in this analysis; the much more extensive FIPS measurements to be collected after orbit insertion (March 18, 2011) will permit tests of this hypothesis.

3.5 Acknowledgements

This work was funded by the MESSENGER project and a NASA Graduate Student Research Program fellowship (JMR). The MESSENGER project is supported by the NASA Discovery Program under contracts NAS5-97271 to the Johns Hopkins University Applied Physics Laboratory and NASW-00002 to the Carnegie Institution of Washington. We acknowledge helpful suggestions by Sean Solomon, MESSENGER Principal Investigator. JMR gratefully acknowledges the help of Eli Busen, Aaron Dodger, and Jonathon Thomas for their contributions to the FIPS software instrument model and related software, and Deborah K. Eddy for help with manuscript preparation. THZ acknowledges the hospitality of the International Space Science Institute in Bern, Switzerland, where much of his contribution to this work was performed.

3.6 Appendix: Data Analysis Process

This appendix summarizes the methodology used to derive the plasma moments discussed in this paper. The key element of this methodology is the creation of a forward model for analyzing the FIPS data. We first develop this methodology and show relevant examples. We then address the density calibration of the FIPS sensor using solar wind data obtained prior to the flybys.

3.6.1 FIPS model

A mathematical analogue of the FIPS instrument was created to model the sampling of distributions in velocity space while taking into account the specific properties of the FIPS field of view, spacecraft obstructions, and dynamic spacecraft orientation. Given a velocity distribution function, we calculated FIPS *E/q* and angle histograms—identical to measurements made during the first and second flyby, and taking into account actual spacecraft trajectory and attitude—and then compared them with the measurements. The code is implemented in the IDL programming language and built in a modular fashion.

The model is constructed so that any three-dimensional (3D) velocity distribution can be input. For the calculations in this paper, a 3D, bi-Maxwellian, gyrotropic distribution is used, with six determining quantities: density, speed, two directions, and two thermal velocities, one parallel to the magnetic field and the other perpendicular to the field. This input distribution is sampled at incident angles and *E/q* values as the physical distribution is sampled by the instrument. Input distributions can be specified in MSO coordinates for work within the Mercury magnetosphere or solar radial-tangential-normal (RTN) coordinates when MESSENGER is in the solar wind [*Fränz and Harper*, 2002]. In RTN coordinates, the R axis points from the Sun to MESSENGER. The T axis is orthogonal to

R and the spin axis of the Sun. The N axis is orthogonal to R and T, completing the right-handed coordinate system.

The model outputs are designed to match actual FIPS telemetered data items, which, for these specific flybys, are a one-dimensional (1D) histogram of counts versus *E/q* and a two-dimensional (2D) histogram of position on the FIPS imaging microchannel plate (MCP) [cf. *Andrews et al.*, 2007] at a variety of time resolutions. This procedure is automated in the recovery scheme described below. Alternatively, the modeled output can be transformed into an arbitrary coordinate system for direct physical interpretation.

MESSENGER trajectory and attitude variation are fully included in the model by use of the Spacecraft, Planet, Instrument, C-matrix Pointing, and Events (SPICE) software package for frame transformations [*Acton*, 1996], interfaced to IDL with an additional toolkit. Spacecraft state information for a given time period is loaded into SPICE, in the form of SPICE C-kernels. Instrument-specific information, in this case the FIPS instrument coordinate system and locations for FOV obstructions, is loaded as instrument kernels. Planetary constants, spacecraft clock offsets, and MESSENGER-specific reference frames (e.g., MSO) are also loaded via such kernels. Once these kernels are loaded, transformations between any two known frames include consideration of this information and thus provide a robust method for handling these time-dependent transformations in a consistent and reliable way.

The fundamental role of the model is to sample the input velocity-space distribution as the actual instrument would. To do this, the model must scan over each pixel on the position-sensing MCP detector as well as the full set of *E/q* values. We denote each pixel by two coordinates, X_{MCP} and Y_{MCP}, and the *E/q* step *i* as $(E/q)_i$. The model proceeds as

follows for each [X_{MCP}, $Y_{MCP,}$ $(E/q)_i$] triplet: The $(E/q)_i$ is transformed to incident velocity, v_i, via the kinetic energy equation. The (X_{MCP}, Y_{MCP}) value is transformed from FIPS MCP to incident zenith (θ) and azimuth (ϕ) angles via a function determined from FIPS ground calibration data. Using SPICE, this triplet (v_i, θ, ϕ), is transformed from FIPS spherical to FIPS Cartesian and then to the Cartesian frame of the input distribution where phase space density, $f(v_x, v_y, v_z)$, is retrieved. This transformation gives phase space density, $f(v_i, \theta, \phi)$, which is related to counts (N_i) at E/q step i (v_i) over time Δt:

$$N_i = \frac{1}{\pi} f(v_i, \theta, \varphi)\, \Delta t\, \eta_i\, g\, \Delta\theta\, \Delta\varphi\, \sin\theta\, {v_i}^4. \qquad (3.1)$$

Eq. (3.1) includes dependence on observed solid angle, $\Delta\theta\, \Delta\phi\, sin\theta$, and two instrument parameters, the effective geometric factor (g) and the efficiency at step i (η_i). Units are $s^3km^{-3}cm^{-3}$ for f, km s^{-1} for v_i, and s for Δt. All angles are in radians. This relation effectively weights counts at higher velocities more than those at lower velocities, in the same way that the instrument does in the process of measurement. Geometric factor and efficiency values derived from calibration data of the actual FIPS instrument are used in the model. The geometric factor represents the effective aperture of the instrument, a combination of the physical aperture area and electrostatic effects experienced by ions passing through the aperture. Efficiency values are calculated by measuring instrument response to known beam conditions as a function of incident angle.

This software model was tested by running a large range of input temperatures, bulk velocities, and incident angles to investigate the limitations and accuracy of FIPS-derived distribution functions. To provide accurate tests, the modeled output was transformed back to the coordinate system of the input, in order to directly compare the effects of FIPS measurements and assess their limitations.

3.6.2 Example: Plasma-sheet data

We show an example of a multi-parameter inversion of a situation reminiscent of Figure 3.2E. We assume an isotropic Maxwellian distribution with a small sunward flow speed and temperature and density values that must be fit to the observations.

Sample outputs from this process are shown in Figure 3.A1 for a single measured *E/q* spectrum. For this part of the analysis, the curves are normalized and the focus is on the thermal speed to fit the shape. Figure 3.A1A-C shows comparisons between modeled spectra and actual data for three candidate v_{th} values. The mean square error for each of these comparisons is shown in Figure 3.A1D. In this case, the minimum error is for the v_{th} = 220 km s^{-1} spectrum, so that value is chosen. The recovery of density proceeds in a similar fashion. An example plot of mean square error versus input n_p is shown in Figure 3.A1E. The recovered density in this example is 0.65 cm^{-3}. Little change in the recovered n and v_{th} values were observed when the bulk velocity was increased to 100 km s^{-1} sunward. So, within limits, our measurements do not provide good constraints on the flow speed and direction of these subsonic plasmas. Similarly, the instrument setting used in flybys 1 and 2 do not provide enough information to derive temperature anisotropy in this situation. The minimum errors for recovered density and temperature are calculated from the shape of the fit curves as shown in Figure 3.A1 and are 0.05 cm^{-3} and 20 km s^{-1}, respectively. An additional uncertainty in the density of 10-20% results from counting statistics of the measured data.

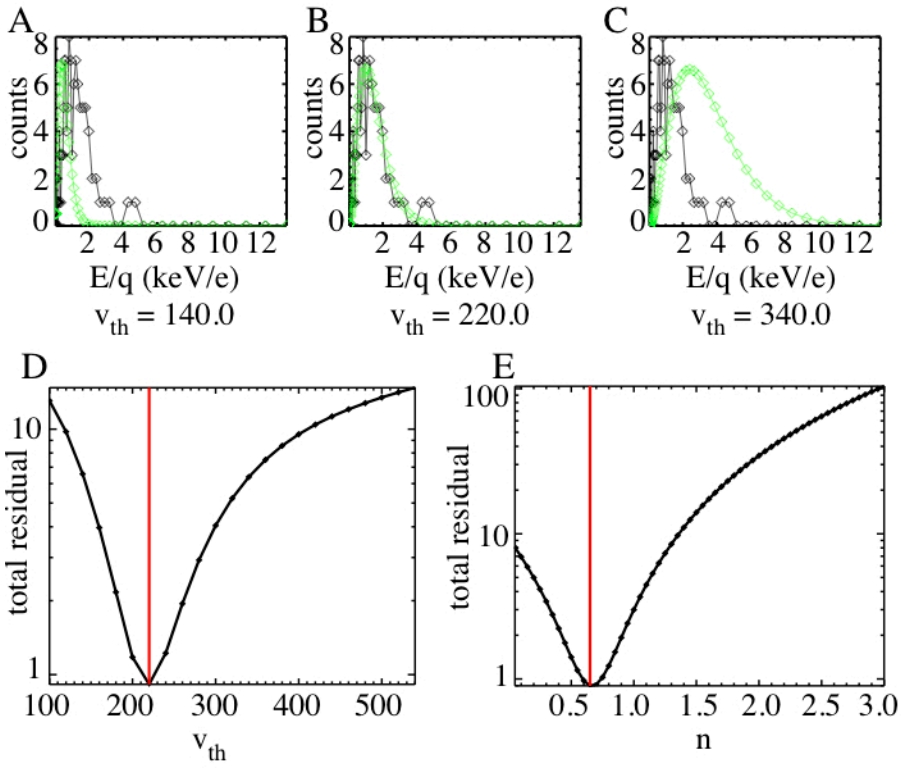

Figure 3.A1. Recovery process details. (A-C) Comparison between measured data (black) and modeled data (green) for three candidate values for v_{th} at one time step in the recovery process. The middle frame (B) shows the best fit. (D) and (E) show total residual between measured and modeled data for all candidate values of the thermal velocity and density for this one time step. The parameter that minimized error in each case is chosen as the recovered value; v_{th} = 220 km s^{-1} and n_p = 0.65 in this case.

3.6.3. Density calibration

As an end-to-end test and as calibration, density recovered from one of these FIPS solar wind observations was compared with solar wind density measured at the same time by comparable instrumentation on the Advanced Composition Explorer (ACE) satellite at 1 AU from the Sun. At four times early in the mission, MESSENGER was rotated so that FIPS could look directly in the solar direction, allowing an unimpeded measurement of the solar wind plasma. However, comparing measurements from the two spacecraft is complicated by the fact that they were at different positions in the variable heliosphere

when the FIPS solar wind measurements were made. To overcome this obstacle, ACE solar wind observations were shifted to the position of MESSENGER through a combination of time offset and radial-dependent scaling [see Eqs. (3.3)-(3.7) below]. Subscripts *S*, *M*, and *A* denote values at the Sun, MESSENGER, and ACE, respectively. The equatorial solar rotation rate (Ω_S) was taken from *Snodgrass* (1990). Radial distance (r) and azimuthal angle (ϕ) were extracted from SPICE for each particular time. Solar wind speed (v_{SW}) was taken from ACE measurements and assumed to be constant. Density (n), temperature (T), and the radial magnetic field component (B_x) were scaled by the radial distances of both spacecraft from the Sun.

$$\Omega_S = 14.71 \text{ deg/day}, \tag{A.2}$$

$$\Delta t = \frac{\varphi_M - \varphi_A}{\Omega_S} + \frac{r_M - r_A}{v_{SW}}, \tag{A.3}$$

$$t_M = t_A + \Delta t, \tag{A.4}$$

$$n_M = n_A \left(\frac{r_A}{r_M}\right)^2, \tag{A.5}$$

$$T_M = T_A \left(\frac{r_A}{r_M}\right)^{4/3}, \tag{A.6}$$

$$B_{X,M} = B_{X,A} \left(\frac{r_A}{r_M}\right)^2. \tag{A.7}$$

ACE plasma and magnetic field data for 40 days around the first FIPS solar wind observation on 15 April 2005 were transformed in this way and compared to density, temperature, and velocity recovered from FIPS measurements, as well as MESSENGER Magnetometer measurements. Since FIPS had an unobstructed view of the solar wind beam, velocity and temperature could be recovered directly from fits to a Maxwellian distribution, without need for the model. Density were recovered from FIPS observations using the procedure described above. The derived magnetic field and plasma parameters

were comparable to within 20%, good agreement indicating that the solar wind parcel measured by the two spacecraft changed very little over the elapsed time.

Chapter 4

MESSENGER Observations of the Spatial Distribution of Planetary Ions Near Mercury

This chapter is taken from Thomas H. Zurbuchen, Jim M. Raines, James A. Slavin, Daniel J. Gershman, Jason A. Gilbert, George Gloeckler, Brian J. Anderson, Daniel N. Baker, Haje Korth, Stamatios M. Krimigis, Menelaos Sarantos, David Schriver, Ralph L. McNutt, Jr., Sean C. Solomon (2011), MESSENGER Observations of the Spatial Distribution of Planetary Ions Near Mercury, *Science*, 333, 1862-1865. I performed all the data reduction processes resulting in Figures 4.2, 4.3 and 4.4 that are essential contributions to this paper. I made significant contributions to the writing and manuscript preparation.

Abstract: Global measurements by MESSENGER of the fluxes of heavy ions at Mercury, particularly Na^+ and O^+, exhibit distinct maxima in the northern magnetic-cusp region, indicating that polar regions are important sources of Mercury's ionized exosphere, presumably through solar-wind sputtering near the poles. The observed fluxes of He^+ are more evenly distributed, indicating a more uniform source such as expected from evaporation from a helium-saturated surface. In some regions near Mercury,

especially the nightside equatorial region, the Na^+ pressure can be a substantial fraction of the proton pressure.

Mercury's dipole magnetic field, particularly its small magnitude and near-alignment with the planet's rotation axis, defines the planet's interaction with the constantly expanding solar atmosphere – the solar wind – and structures the plasma and charged-particle environment of the planet [*Anderson et al.*, 2011]. By its orientation and strength, Mercury's magnetic field inhibits direct solar wind access to the planetary surface in dayside equatorial regions [*Slavin et al., 2008]*, where the average magnetic field orientation is nearly perpendicular to the velocity of the incoming solar wind [*Kabin et al.*, 2000]. At high latitudes, in contrast, the solar wind interaction with the magnetic field forms northern and southern "cusps," funnel-shaped indentations in the magnetopause that capture some of the magnetosheath plasma and guide it to lower altitudes [*Frank*, 1971; *Haerendel et al.*, 1978]. Since Mercury lacks an appreciable atmosphere, this funneling of solar wind plasmas down to the surface is of particular importance because the incident plasma is believed to sputter neutral atoms from the surface into the exosphere and to account for a substantial portion of the exosphere's variability [*Killen et al.*, 2007]. Neutral exospheric particles can also be generated by other processes, such as thermal evaporation off Mercury's surface, desorption stimulated by photons or electrons, and micrometeoroid impact. Less well understood are surface processes that might lead to the direct ejection of ions from the planetary surface [*Killen et al.*, 2007]. Whether they originate from ionization of the neutral exosphere or from the surface, Mercury's ions subsequently undergo energization and transport by

electromagnetic forces that dominate Mercury's space environment [*Slavin et al.*, 2008; *Lukyanov et al.*, 2004].

During its near-equatorial flybys of the innermost planet in 2008–2009, the MErcury Surface, Space ENvironment, GEochemistry and Ranging (MESSENGER) spacecraft obtained initial measurements of the structure of the magnetosphere (Figure 4.1). Mercury's magnetic field is highly distorted by the solar wind. On the dayside the planetary magnetic field is compressed by the ram pressure of the incident solar wind, whereas on the nightside the magnetic field is pulled back to form a long magnetic tail [*Slavin et al.*, 2010]. Special attention is called to the northern and southern cusp regions, from which ions from all sources stream along magnetospheric field lines into the northern and southern lobes of the tail where they drift toward the tail's equatorial plane to concentrate and form the plasma sheet [*Delcourt et al.*, 2007].

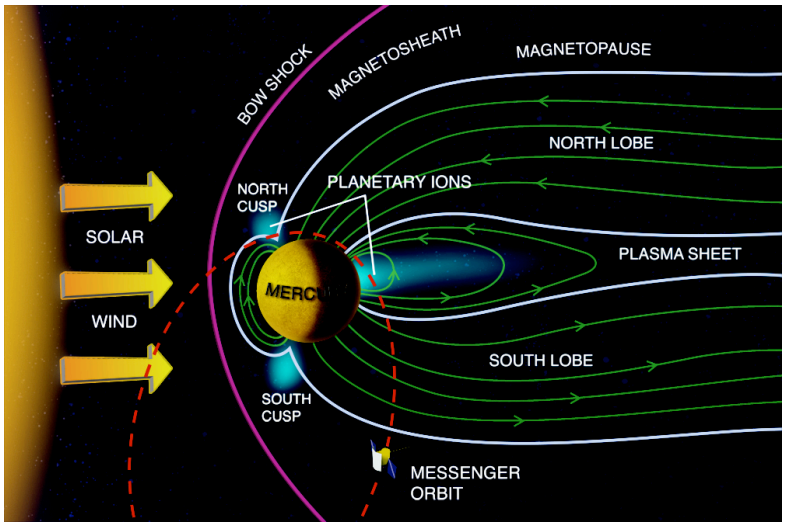

Fig 4.1. This schematic view of Mercury's magnetosphere, derived from measurements made during MESSENGER's three flybys, provides a context for the measurements reported here. Mercury's planetary magnetic field largely shields the surface from the supersonic solar wind emanating continuously from the Sun. MESSENGER has been in a near-polar, highly eccentric orbit (dashed red line) since 18 March 2011. Maxima in heavy ion fluxes observed from orbit are indicated in light blue.

MESSENGER was inserted into orbit about Mercury on 18 March 2011, and here we report the results of near-continuous measurements of planetary ions near Mercury on a global scale. These measurements were made with the Fast Imaging Plasma Spectrometer (FIPS), the low-energy portion of the Energetic Particle and Plasma Spectrometer (EPPS) instrument [*Andrews et al.*, 2007]. We focus on the spatial distribution of the most abundant ions with energy per charge *E/q* between 0.1 and 13 keV/e and with mass per charge *m/q* between 4 and ~50 atomic mass units per unit charge. Ions within those ranges constitute over 80% of the heavy ions (i.e., singly charged ions heavier than H^+) measured by FIPS. Ions with *m/q* = 21-30 (here termed the Na group, and including Na^+, Mg^+, and Si^+, among others) are dominated by Na^+, the most abundant exospheric ion component [*Zurbuchen et al.*, 2008]. Ions with *m/q* = 14-20 (here termed the O group) include O^+ and water-group ions (such as H_3O^+, OH^+, and H_2O^+). Because He in the solar wind is fully ionized, the observed He^+ (*m/q* = 4) flux must largely be produced locally, although it may contain a contribution of helium from interstellar gas, ionized near the Sun and then swept along with the solar wind [*Möbius et al.*, 2004].

As shown in Figure 4.2, He^+ and the Na and O groups of exospheric ions are distributed throughout the entire volume of Mercury's magnetosphere traversed by MESSENGER. Na-group and O-group fluxes peak near the northern polar regions, close to the periapsis of MESSENGER's eccentric orbit and coinciding with the location of the northern magnetic-cusp region. He^+ does not show a distinct enhancement in such regions but is more evenly distributed, with observed fluxes near 60°N latitude comparable to values seen elsewhere even though Na-group and O-group ions are enhanced by factors of 3 or more. Ions that are strongly associated with surface

sputtering effects near the magnetospheric cusps should be concentrated near the polar regions, whereas ionized exospheric components associated with the global neutral exosphere would not be expected to have such a strong correlation with polar regions but would instead be distributed more evenly around the planet. At comparable distances, fluxes near dusk (~18 hours local time) are identical to those near dawn (~6 hours local time) to within 5%. A predicted large-scale asymmetry, resulting from the transport of exospheric particles in Mercury's magnetosphere [*Lukyanov*, 2004], has not been observed. Measured spatial distributions of Na-group, O-group, and He^+ ions might also reflect the spatial distribution of the associated components in a neutral exosphere in which the He originates primarily from evaporation of a He-saturated planetary surface [*Hartle et al.*, 1975].

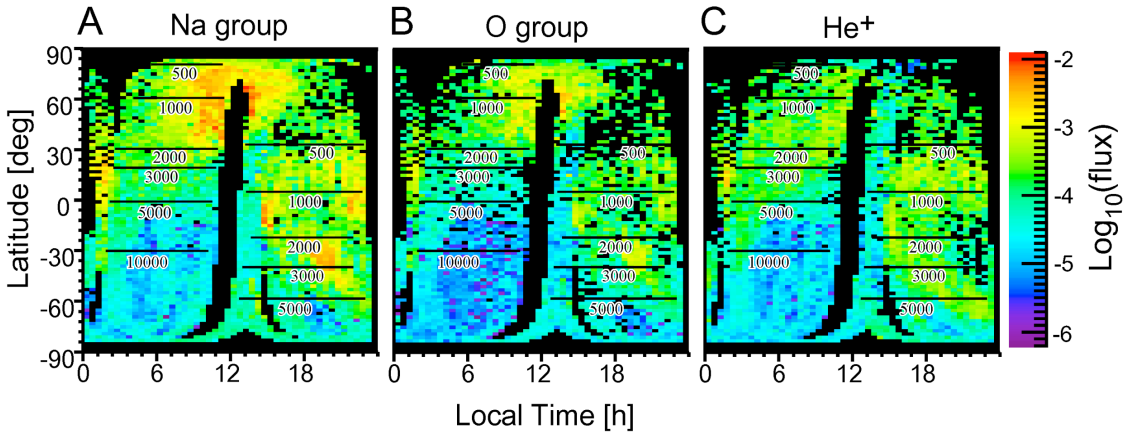

Fig. 4.2. Spatial distribution of (**A**) Na-group, (**B**) O-group, and (**C**) He^+ ions versus planetary latitude and local time. Measurements span 66 days (26 March to 30 May 2011) of MESSENGER orbital observations, during which the periapsis local time varied from 17.84 hr to 10.14 hr. Approximate distances from Mercury's surface in km are indicated in black. Colors indicate relative fluxes (in units of $cm^{-2}sr^{-1}s^{-1}$); black areas denote regions not observed, including a swath during which FIPS was mostly powered off. The observed heavy-ion data were collected at 8-s time resolution for most of each orbit and binned by latitude and local time in bins of width 2° and 0.5 hr. Multiple measurements in a single bin were averaged. During these orbits, near Mercury, the planet is generally within the $\sim 1.4\pi$ sr field of view of the FIPS instrument. At distances greater than ~1 Mercury radius, the probability for FIPS to observe ions strongly depends on spacecraft orientation. For example, the solar direction is obstructed at all times by the spacecraft's sunshade. The *m/q* ratio is derived from the measured ratio of *E/q* and a velocity measurement, through time of flight, of each ion [*Andrews et al.*, 2007].

Observations during three dayside high-latitude magnetospheric passes, each lasting 30-40 min, provide strong evidence for the cusp association of Na-group and O-group ions (Figure 4.3). On each orbit MESSENGER crossed the bow shock and magnetopause moving anti-sunward and eastward at local times of 09:00 to 10:00 and altitudes of 2000 to 2700 km and 1200 to 1800 km, respectively. The cusp passages are identified by a diamagnetic depression in magnetic field intensity and are characterized by the appearance of 0.1-2 keV H^+. These MESSENGER cusp encounters occurred at magnetic latitudes of 65-75°N and altitudes of 600-800 km, or about halfway between the magnetopause and the surface. The duration of the cusp crossings varied from ~100 s for the first two passes to ~150 s for the last. These durations imply that the horizontal dimensions of the cusp along these trajectories were 400–600 km.

On 13 April the heavy ion flux was maximum near the magnetopause, but heavy ions were also present throughout the entire pass, with the lowest fluxes observed after crossing the bow shock and poleward of the cusp. On 14 April the strongest heavy-ion fluxes were observed within and just prior to the cusp traversal. However, the most intense and most broadly distributed heavy-ion fluxes were seen during the 16 April pass. Here, the heavy-ion flux exhibited a broad maximum near the magnetopause, but the flux was very high from the middle of the magnetosheath through the cusp region, after which it dropped rapidly. The interplanetary magnetic field (IMF) orientation was quite variable during these passes, and additional studies will be necessary to ascertain the external factors controlling the penetration of heavy planetary ions from the magnetosheath into the magnetosphere and the local production of neutral and ionized species associated with surface sputtering. However, the most probable reason for the enhanced ion flux on 16

April (Figure 4.3C) is the anti-sunward and northward direction of the IMF measured just prior to the bow-shock encounter. This IMF orientation is believed to be favorable to magnetic reconnection between the IMF and the magnetospheric magnetic field just tailward of the northern cusp, leading to enhanced solar wind access to the surface and ion sputtering in the northern cusp [*Sarantos et al.*, 2001].

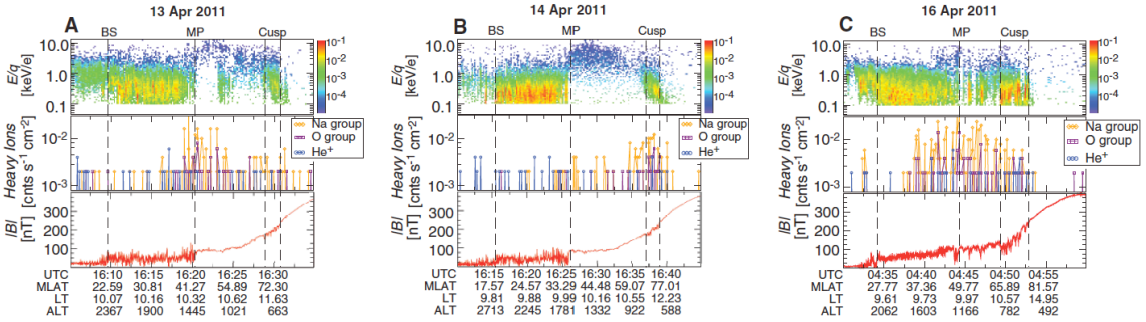

Fig. 4.3. MESSENGER observations for three passes through the dayside magnetosphere on (**A**) 13, (**B**) 14, and (**C**) 16 April 2011. For each, the top panel gives *E/q* spectrograms for H^+ with a time resolution of 8 s covering the *E/q* range 0.1-13 keV/e. The middle panel gives the integrated flux of He^+, O-group, and Na-group ions at the same time resolution and *E/q* range. The bottom panel gives the magnitude of the measured magnetic field with a time resolution of 50 ms. All quantities are plotted relative to Coordinated Universal Time (UTC), magnetic latitude (MLAT, degrees), local time (LT, fractional hr), and altitude over Mercury's surface (ALT, km). Magnetic latitude includes the northward offset of Mercury's magnetic equator from the geographic equator [*Anderson et al.*, 2011]. These passes show representative maxima in the H^+ and heavy-ion fluxes at high magnetic latitudes near noon local time (Fig. 1). On each orbit, MESSENGER crossed the bow shock (BS) and the magnetopause (MP) and entered the magnetosphere near 10:00 local time at magnetic latitudes 30–50°N, and the spacecraft moved closer to Mercury as it headed northwestward to encounter the cusp near noon around 62–72°N. The FIPS field of view was stable during all three passes, so the H^+ and heavy-ion fluxes may be compared along each pass and from pass to pass.

Enhancements to the fluxes of Na-group and O-group ions were also observed during MESSENGER passes through the nightside magnetosphere at equatorial latitudes (Figure 4.2). Three examples of such equatorial passes on 13, 15, and 21 April are displayed in Figure 4.4. As with the cusp region, these enhancements were often, but not always, associated with diamagnetic decreases in the magnetic field (Figure 4.4A, B). Although lower fluxes of these heavy ions can be observed at slightly higher and lower latitudes,

they maximized near the magnetic equator. The measurements in Figure 4.4 are consistent with passages through the inner portion of the plasma sheet that separates the northern and southern lobes of Mercury's magnetotail (*Slavin et al.*, 2008; *Slavin et al.*, 2010; *Delcourt et al.*, 2007).

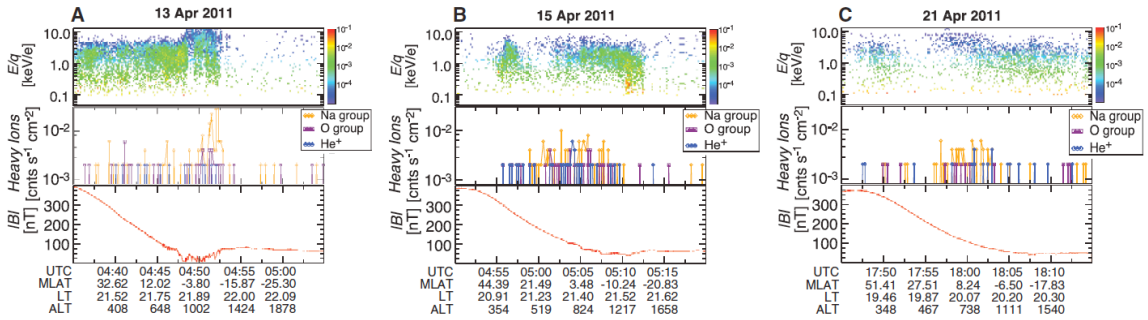

Fig. 4.4. MESSENGER observations for three passes through the pre-midnight magnetosphere at mid to low latitudes on (**A**) 13, (**B**) 15, and (**C**) 21 April 2011 in the same format as in Fig 3. These passes show representative maxima in the H^+ and heavy-ion fluxes near low magnetic latitudes (Fig. 1). On each orbit MESSENGER moved southward and away from Mercury until it crossed Mercury's equatorial plane at altitudes of 800–1000 km.

For Maxwellian velocity distributions and low Mach numbers, we determined densities, temperatures, and thus thermal pressures for the H^+ and Na-group ions, where sufficient counts were available [*Raines et al.*, 2011]. Typically, within these assumptions, the densities and temperatures are accurate to within 20% and are mostly limited by counting statistics. For a given temperature, magnetic field strength, and ion mass-per-charge ratio, the spatial scale of the gyrating motion of a given particle around the field, the Larmor radius, can be calculated. Temperatures of H^+ and Na-group ions imply Larmor radii in the ranges 10-30 km and 200-700 km, respectively. Both ion groups should therefore be organized by the magnetospheric field, although the Larmor radii of Na-group ions are of the same order of magnitude as the horizontal dimension of the cusp. For the cusp passage of 16 April (Table 4.1), we find a thermal pressure ratio

$P_{Na-group} / P_{H^+}$ of 2%. The heavy ion particle distributions during the passages of 13 and 14 April are non-Maxwellian, and a pressure calculation is not possible with this methodology.

Table 4.1. Estimates of ion density *n*, temperature *T*, and pressure *P* for the cusp (C) and equatorial (E) regions shown in Figs. 4.3 and 4.4.

		H^+			Na group		
Date		*n*, cm^{-3}	*T*, MK	*P*, nPa	*n*, cm^{-3}	*T*, MK	*P*, nPa
13 Apr	C	12	1.3	0.22	(1)	(1)	(1)
14 Apr	C	20	0.79	0.21	(1)	(1)	(1)
16 Apr	C	40	0.79	0.44	0.5	1	0.008
13 Apr	E	1.5	5.1	0.11	(2)	(2)	(2)
15 Apr	E	1.6	3.6	0.079	0.2	1-3	0.003-0.008
21 Apr	E	0.28	7.8	0.030	0.3	3	0.01

Notes: (1) Too few counts. (2) Substantial bulk velocity violates assumptions for data inversion.

All magnetospheric passes in Figure 4.4 exhibit strong maxima in the heavy-ion flux near the equator. In all cases, there was a maximum in the Na-group flux near the equator, yet the extent of these heavy-ion maxima varied by a factor of ~3 among the three passes. We determined H^+ and Na-group thermal pressure ratios for the 15 and 21 April equatorial passes (Table 1): $P_{Na-group} / P_{H^+}$ = 4-10% and 33%, respectively (Table 1). The nightside magnetospheric plasma is expected to be transported preferentially through the magnetically dominated lobe regions and concentrated in the plasma sheet at low latitudes. The plasma sheet is threaded by closed planetary magnetic fields such that its northward component combined with the dawn-to-dusk electric field imposed by the

global solar wind interaction result in a sunward magnetic stress. This stress is balanced by a tailward-directed gradient in the plasma pressure (i.e., plasma density and temperature decrease with increasing downtail distance).

The heavy-ion observations provide important constraints for Mercury's neutral exosphere and its temporal variability and spatial distribution. Single-particle calculations indicate that He^+ and O^+ ion fluxes could be comparable if the near-surface density of neutral oxygen does not exceed 200 atoms cm^{-3}, as predicted by exosphere models [*Sarantos et al.*, 2001; *Wurz et al.*, 2010]. From the observed spatial distributions, the energy of the observed ions, and comparisons with observations of the neutral exosphere, we conclude that the planetary ions discussed here are being created by the ionization of exospheric neutral species. Moreover, MESSENGER observations reveal that Mercury's cusps act as natural collection points and conduits for solar wind and planetary ions, such as the O group, Na group, and other ions, that are likely to contribute to the neutral exosphere as they precipitate onto the planetary surface. There are orbit-to-orbit differences in observations, which reflect the magnetospheric response to a highly variable solar wind [*Baker et al.*, 2011] and which are anticipated from the temporal variability of Earth-based observations of the Na exosphere [*Killen et al.*, 2007]. Given the high heavy-ion thermal pressures relative to proton pressures at Mercury reported here, the role of heavy ions must be included to properly understand the dynamics of Mercury's magnetosphere.

Acknowledgements: The MESSENGER project is supported by the NASA Discovery Program under contracts NAS5-97271 to the Johns Hopkins University

Applied Physics Laboratory and NASW-00002 to the Carnegie Institution of Washington.

Chapter 5

Distribution and Compositional Variations of Plasma Ions in Mercury's Space Environment: The First Three Mercury Years of MESSENGER Observations

This chapter is taken from Jim M. Raines, Daniel J. Gershman , Thomas H. Zurbuchen, Menelaos Sarantos, James A. Slavin, Jason A. Gilbert, Haje Korth, Brian J. Anderson, George Gloeckler, Stamatios M. Krimigis, Daniel N. Baker, Ralph L. McNutt, Jr., Sean C. Solomon (2013), Distribution and compositional variations of plasma ions in Mercury's space environment: The first three Mercury years of MESSENGER observations, *J. Geophys. Res.*, (in press).

Abstract

We have analyzed measurements of planetary ions near Mercury made by MESSENGER's Fast Imaging Plasma Spectrometer (FIPS) over the first three Mercury years of orbital observations (25 March 2011 through 31 December 2011). We determined the composition and spatial distributions of the most abundant species in the regions sampled by MESSENGER during that period. In particular, we here focus on altitude dependence and relative abundances of species in a variety of spatial domains. We used observed density as a proxy for ambient plasma density, because of limitations to the FIPS field of view. We find that the average observed density is 3.9×10^{-2} cm^{-3} for

He^{2+}, 3.4×10^{-4} cm^{-3} for He^{+}, 8.0×10^{-4} cm^{-3} for O^{+}-group ions, and 5.1×10^{-3} cm^{-3} for Na^{+}-group ions. Na^{+}-group ions are particularly enhanced over other planetary ions (He^{+} and O^{+} group) in the northern magnetic cusp (by a factor of ~2.0) and in the pre-midnight sector on the nightside (by a factor of ~1.6). Within 30° of the equator, the average densities of all planetary ions are depressed at the subsolar point relative to the dawn and dusk terminators. The effect is largest for Na^{+}-group ions, which are 49% lower in density at the subsolar point than at the terminators. This depression could be an effect of the FIPS energy threshold. The three planetary ion species considered show distinct dependences on altitude and local time. The Na^{+} group has the smallest *e*-folding height at all dayside local times, whereas He^{+} has the largest. At the subsolar point, the *e*-folding height for Na^{+}-group ions is 590 km, and that for the O^{+} group and He^{+} is 1100 km. On the nightside and within 750 km of the geographic equator, Na^{+}-group ions are enhanced in the pre-midnight sector. This enhancement is consistent with non-adiabatic motion and may be observational evidence that non-adiabatic effects are important in Mercury's magnetosphere.

5.1 Introduction

The plasma environment at Mercury is determined by a complex interaction of plasma and neutral atom populations and competing processes involving Mercury's surface, Mercury's atmosphere, solar photons, and the solar wind. Mercury's thin, collisionless atmosphere – a surface-bounded exosphere – is produced by a variety of processes that act on the surface of the planet. It is composed mainly of neutral H, He, Na, Mg, K, Ca, Al, and Fe atoms, though other constituents are expected [*Broadfoot et al*., 1974; *Domingue et al.*, 2007; *Killen et al*., 2007; *McClintock et al*., 2009; *Killen and*

Bida, 2012]. These atoms may be on ballistic trajectories, in orbit around the planet, or on escape trajectories that are controlled by Mercury's gravity, their initial launch energy, and solar radiation pressure. Though the fraction of atoms escaping depends substantially on season, there is a sufficient population to form a persistent, though rarified, cloud around the planet [*Potter et al*., 2007; *Leblanc and Johnson*, 2010; *Schmidt et al*., 2012]. On the nightside, radiation pressure stretches this cloud into a comet-like neutral Na tail that extends more than 1,000 Mercury radii (R_M) in the anti-sunward direction [*Potter and Killen*, 2002; *Baumgardner et al*., 2008; *Baumgardner and Mendillo*, 2009]. Ground-based telescopic studies [reviewed by *Killen et al*., 2007] have shown large variations in inferred neutral column densities, their distribution through Mercury's atmosphere and space environment, and the relative abundances among the various species, both seasonally and on timescales of hours [*Potter and Morgan*, 1990, 1997; *Killen et al*., 1990, 1999, 2001, 2003; *Sprague et al*., 1997, 1998; *Potter et al*., 1999; *Schmidt et al*., 2012].

The seasonal variability of the exosphere is related to changes in the solar photon intensity, the Doppler shift in the incident solar radiation, and the solar wind environment and micrometeoroid influx during Mercury's highly eccentric orbit, but it may also be related to a limited surface reservoir of volatiles [e.g., *Leblanc and Johnson*, 2003, 2010; *Killen et al*., 2004]. The observed variability of Na on the timescale of hours has been hypothesized to relate to variations in Mercury's local space environment, including variations in solar wind dynamic pressure and the interplanetary magnetic field (IMF) affecting dayside magnetic reconnection with Mercury's internal dipole field [e.g., *Killen et al*., 2001; *Sarantos et al*., 2007]. These two processes control the direct impact of solar

wind plasma onto the surface and therefore the resultant sputtering of surface material, the most variable of the exospheric sources [e.g., *Sarantos et al*., 2001, 2007; *Massetti et al*., 2003; *Benna et al*., 2010].

Planetary ions are formed at Mercury through several processes, including photoionization of exospheric neutral atoms, sputtering directly off the surface by solar wind, and vaporization of micrometeoroids upon impact on the surface [*Cheng et al*., 1987]. Once created, these planetary ions become part of the planet's plasma environment, and their motion is dominated by the interaction of the solar wind with Mercury's small internal magnetic field. The field is weak but sufficient to stand off the solar wind (under most circumstances) and form a small, permanent magnetosphere [*Ogilvie et al*., 1974; *Slavin et al*., 1979; *Russell et al.,* 1988; *Zurbuchen et al*., 2004]. Mercury's magnetosphere has a basic structure that is similar to that of Earth but is much smaller, and Mercury's weaker internal field causes the planet to take up a much larger fractional volume [*Russell et al.,* 1988; *Slavin*, 2004]. Furthermore, Mercury's closer distance to the Sun places it in a region that subjects its magnetosphere to higher solar wind densities (by a factor of ~10 on average) and a more radial interplanetary magnetic field than at Earth. These factors together make Mercury's magnetosphere very dynamic, with reconnection rates ~10 times faster than at Earth and a Dungey cycle time of ~2 min [*Slavin et al*., 2009] compared with ~ 1 h at Earth [*Dungey*, 1961]. Mercury is therefore an important test case for our understanding of planetary magnetospheres and their interaction with the solar wind [*Baker et al.,* 2012].

Mercury's small magnetosphere has a strong impact on fundamental plasma dynamics. Once created, ions begin to gyrate around the local magnetic field and are

"picked up" into the convection of the magnetospheric plasma. Because heavy ions can have gyroradii that are large compared with the size of the small magnetospheric system, finite-gyroradius effects are expected to be prevalent, causing anisotropic or possibly non-gyrotropic phase space distributions [*Delcourt et al*., 2002, 2003]. In particular, both planetary ions and solar wind ions entering the open magnetosphere are expected to be in loss-cone distributions. Such distributions occur when ions with pitch angles inside the loss cone collide with the planet and are removed from the distribution. Finite-gyroradius effects can allow ions to be lost due to gyration across the magnetopause boundary and resulting pickup into the solar wind and give rise to non-adiabatic behavior, by which ions no longer gyrate around a single guiding center and can detach from magnetic field lines. Since gyroradius increases with the ratio of mass per charge (m/q), heavy ions of planetary origin (e.g., Na^+ ions, m/q = 23 amu/e) are expected to experience these effects markedly more than He^{2+} (m/q = 2 amu/e) from the solar wind.

During its first Mercury flyby (M1) on 14 January 2008, the MErcury Surface, Space ENvironment, GEochemistry, and Ranging (MESSENGER) spacecraft [*Solomon et al*., 2007] made the first observations of planetary ions with the Fast Imaging Plasma Spectrometer [*Zurbuchen et al.*, 1998; *Andrews et al*., 2007]. MESSENGER flew by Mercury two additional times, on 6 October 2008 (M2) and 29 September 2009 (M3), before being inserted into orbit. A first analysis of M1 data revealed the presence of H^+, He^{2+}, He^+, Na^+/Mg^+, and several other heavy ion species [*Zurbuchen et al*., 2008].

MESSENGER became the first spacecraft to orbit Mercury on 18 March 2011, and FIPS began taking continuous measurements shortly thereafter. Analysis of the first 65 days of orbital observations by *Zurbuchen et al*. [2011] reinforced the flyby analysis and

revealed that planetary ions were typically organized into three dominant features. On the dayside, a large plasma population was observed at high northern latitudes, in the region of the magnetospheric cusp. On the nightside, plasma was observed near the equator, in the central plasma sheet. Finally, increased plasma flux was observed near the magnetopause with corresponding planetary ion enhancements that span the magnetopause boundary (as identified in magnetic field measurements [*Winslow et al.,* 2012; *Anderson et al.,* 2012]). These features are observed on nearly every orbit, despite highly variable solar wind and IMF conditions [*Baker et al*., 2012; *Gershman et al*., 2012].

In this work, we present analysis of FIPS planetary ion measurements over the first three Mercury years of the MESSENGER orbital mission (25 March 2011 through 31 December 2011). Analysis results include ion composition, the distribution of different species in latitude and local time, their dependence on altitude, and their relative abundances in a variety of spatial domains. We have compared these results with the predictions of global modeling studies and neutral exosphere observations. The results are shown to have important implications for planetary ion formation and transport in Mercury's small magnetosphere.

5.2 Description and Processing of Measurements

FIPS is a miniaturized time-of-flight (TOF) plasma mass spectrometer designed to measure heavy ions (atomic number > 4) in Mercury's space environment. When inside of the magnetosphere, the FIPS sensor measures energy per charge (E/q) from 0.1 to 13 keV/e, with a time resolution (scan time) of ~ 8 s. Outside of the magnetosphere, the E/q range is 0.05–13 keV/e and the time resolution is ~ 1 min. The instrument can resolve

mass per charge from 1 to 60 amu e^{-1}. FIPS has a very large instantaneous field of view (FOV) of ~ 1.4 sr and an approximate angular resolution of 15°. A portion of the FIPS FOV is blocked due to its position behind the spacecraft sunshade. A detailed description of the FIPS placement on the spacecraft, its FOV obstructions, and their impact on measured distribution functions was given by *Raines et al*. [2011]. Because the dominant flow in the magnetosphere is sunward or anti-sunward and the FIPS FOV points mostly to the side, the velocity distribution core (center) is typically not within the FOV. Under these conditions, we must apply a model-based recovery algorithm on an individual time-step basis to estimate plasma moments. Whenever the distribution is isotropic and hot (i.e., a thermal velocity comparable to convection speed), the plasma density and temperature can be estimated without knowledge of the three-dimensional bulk speed [*Raines et al*., 2011]. Though these conditions are often reasonably met in both the magnetospheric cusp and plasma sheet, they do not apply to all of the measurements included in this large survey. Therefore, we do not attempt to recover the true number density of the ambient plasma from the observations in this work. We instead use observed number density, n_{obs}, as a proxy for comparisons of relative abundances of different ion constituents. Observed density is calculated by converting observed counts to phase space density then integrating over the observed velocity range, to reach particles per unit volume (cm^{-3}) observed by FIPS. *Gershman et al.* [2012] has described the calculation of n_{obs} for solar wind ions, but an identical calculation applies for both supersonic and subsonic plasmas. Observed density differs from the true number density of the ambient plasma by a time-dependent and unknown factor that depends on the vector flow velocity of the plasma, the plasma thermal velocity, and the orientation of the

spacecraft. The assumption here is that different ions will have similar distribution functions to one another, and consequently their observed densities can be compared.

If different ion species arrive at the instrument with substantially different velocity distribution functions, our estimates of relative abundances will be affected. For example, the heaviest planetary ions are likely to exhibit large loss cones. In the more extreme cases, ions that are created just before measurement may not have had sufficient time to scatter into an isotropic or even gyrotropic distribution and are thus highly directional. In contrast, solar wind ions, such as He^{2+}, are much more likely to be near equilibrium and have distributions that are not far from Maxwellian. The cusp is a region for which our estimates of relative abundance are most trustworthy because the electric fields there are expected to be small and particles are not expected to be highly directional. Where the effects of the limited FOV of FIPS are substantial, observed densities for planetary ions reported here are lower limits.

FIPS uses a double-coincidence technique to greatly reduce background noise. However, spurious double-coincidence counts still do occur. These counts come from two main sources: the extension of very-high-count proton measurements into other times of flight, and the release of small numbers ions from surface processes within the instrument. Although all major ion species reported here can be analyzed from the raw data, accuracy is markedly improved by removing these spurious counts. A detailed noise model and removal method has been developed and is employed with the data in this work at the individual scan level. After noise removal, ion species are identified from *E/q*–TOF tracks. To improve signal to noise, heavy planetary ions are grouped together into *m/q* ranges. This analysis makes use of two ion groups: O^+ group (*m/q* = 16

– 20 amu/e, including O^+ and water-group ions) and Na^+ group (m/q = 21-30 amu/e, including Na^+, Mg^+, and Si^+). Additional details concerning this process are given in the Appendix.

Observations analyzed here were taken on an orbit-by-orbit basis and thus occurred at altitudes ranging from 200 km to 15,248 km over 3.1 Mercury years (565 orbits). Because the MESSENGER orbital plane is approximately fixed in inertial space, the periapsis altitude of the orbit moves around the planet during each Mercury year. A side effect of this arrangement is that a particular local time of periapsis is always sampled at the same part of Mercury's orbit around the Sun, so that local time variations in our figures may involve contributions from seasonal variations of the exosphere. Several sample orbits are shown in Figure 5.1, along with the respective Mercury true anomaly angle (TAA), which describes the position of Mercury in its orbit around the Sun, and the radial distance to the Sun (R).

Another complication for the interpretation of these measurements arises from the placement of FIPS on one side of the spacecraft: measurements around the subsolar point are taken with FIPS pointing approximately perpendicular to the radial direction from Mercury. For these measurements, the angle between FIPS boresight vector and the Mercury radial direction is in the range 80–100°. In contrast, this angle is mostly in the range 40–60° for measurements elsewhere around the planet, symmetric about dawn and dusk. Small variations in pointing within the above ranges should not affect conclusions drawn from this analysis.

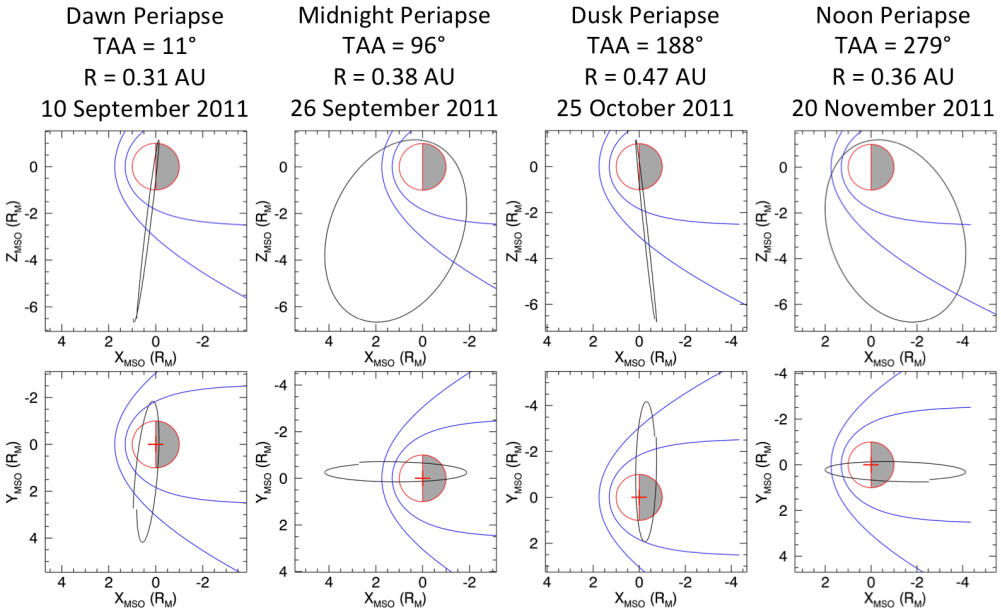

Figure 5.1. Selected MESSENGER orbits during the first three Mercury years of the MESSENGER orbital mission showing periapsis at four different local times. Mercury TAA and radial distance to the Sun (in AU) are also given.

5.3 Data Analysis and Overview of Results

We analyzed the detections of planetary ion species in the Na^+ group, the O^+ group, and He^+, for data collected from 25 March 2011 through 31 December 2011, a span that includes the first 3.1 Mercury years of the MESSENGER orbital mission. We also included He^{2+} as a tracer for solar wind plasma, since these ions cannot be produced in substantial numbers within the Mercury environment. It is important to note that approximately 97% of the plasma ions measured by FIPS are protons, but since the focus of this work is planetary ions, protons are not included here. The average observed density for each of these species, as well as the ratio of each to the averaged n_{obs} for Na^+-group ions, is given in Table 1. These values are computed by averaging the n_{obs} value from each FIPS *E/q* scan over all of the measurements, including all altitudes and latitudes. MESSENGER spends most of its time far from the surface, so lower n_{obs}

values are weighted heavily in Table 1. The data from the first (M1) and second (M2) MESSENGER flybys of Mercury have been re-analyzed with these updated and refined techniques. They are also presented in Table 1.

Table 5.1. Mean and standard deviation of observed density (in cm^{-3}), by ionic species, averaged over all altitudes for orbital and flyby (M1+M2) measurements. The ratio of the mean to that of Na^+-group ions is also given for both data sets.

Species	Orbital		M1+M2	
	$\langle n_{obs} \rangle$ (cm^{-3})	Ratio	$\langle n_{obs} \rangle$ (cm^{-3})	Ratio
He^{2+}	$(3.9 \pm 0.0012) \times 10^{-2}$	7.7	$(1.0 \pm 0.012) \times 10^{-3}$	0.31
He^+	$(3.4 \pm 0.0035) \times 10^{-4}$	0.067	$(2.2 \pm 0.23) \times 10^{-3}$	0.68
O^+ group	$(8.0 \pm 0.010) \times 10^{-4}$	0.16	$(1.0 \pm 0.18) \times 10^{-3}$	0.31
Na^+ group	$(5.1 \pm 0.0043) \times 10^{-3}$	1	$(3.3 \pm 0.047) \times 10^{-3}$	1

Notes: Observed densities near the surface are at least one order of magnitude higher than given in this table. Standard deviation is divided by the square root of the number of measurements to estimate the error in the mean. Flyby data are from the magnetosphere only.

5.3.1 Global Distribution of Measurements

To assess the global spatial distribution of measurements, we co-added all measurements for all four species over this period and binned them into two-dimensional spatial maps. The map for Na^+-group ions is shown in Figure 5.2. The coordinate system used, Mercury solar orbital (MSO) coordinates, is centered on the planet and defined as follows: the X_{MSO} axis points from Mercury toward the Sun; the Z_{MSO} axis points north, normal to Mercury's ecliptic plane; and the Y_{MSO} axis completes the right-handed triad. The color in each cell represents average n_{obs}, calculated from the n_{obs} values measured within a 100 km × 100 km grid divided by the number of FIPS scans

taken within the cell, to normalize the inherently uneven sampling (in time) of the various spatial cells. The color scale for these and the other maps in this work is logarithmic to show variations on multiple scales. On these maps, black indicates $n_{obs} = 0$ cm^{-3}, meaning that no counts were observed. White indicates that the spacecraft did not pass through that cell.

The noon-midnight projection in Figure 5.2a shows that planetary ions are much more abundant close to the planet, within ~5000 km, than they are farther away. Three areas of major enhancement Na^+-group ions are clearly visible; these will be discussed below.

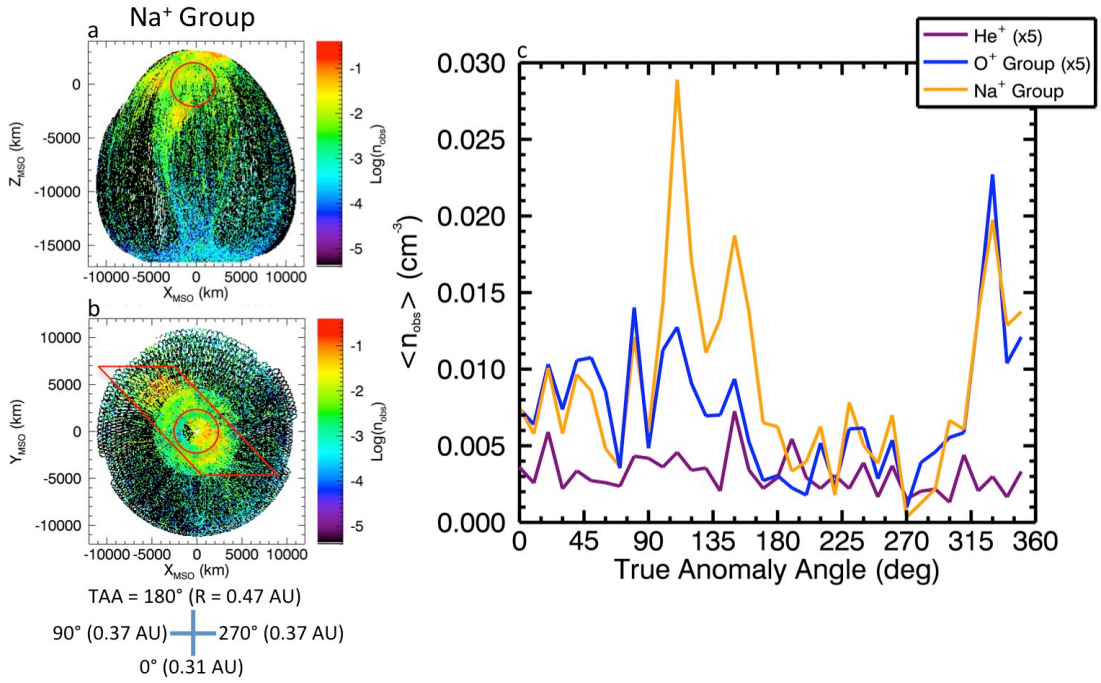

Figure 5.2. Average observed ion density (cm^{-3}) projected onto (a) noon-midnight and (b) equatorial planes. Binning within each plane shown is 100 km by 100 km. The Sun is to the right in these figures. Red circles show the approximate size of the planet in the projection planes. The approximate Mercury TAA at four MESSENGER periapsis local times (in the equatorial plane) is indicated in the legend at bottom left, along with Mercury's heliocentric distance in AU. The enhancements outlined in a red trapezoid are discussed in the text. (c) Average observed ion density (cm^{-3}) plotted versus Mercury TAA, collected into 10° bins for each of the three planetary species. Note that FIPS provides a local rather than a global measurement.

The equatorial projection for Na^+ group (Figure 5.2b) shows enhancements as well. In particular, enhancements centered on (X_{MSO}, Y_{MSO}, Z_{MSO}) = (2500, -2000, 0) km on the dayside and (-3500, 4500, 0) km on the nightside are very prominent. These observations may come from groups of orbits with an overall higher average observed density, a temporal effect. Alternatively, the dayside and nightside enhancements may be independent of one another and depend on the spatial region being sampled. If the enhancements are from groups of orbits, they would be those with MESSENGER periapsis at local times in the range 6−11.5 h (dawn-to-subsolar sector). Orbits grouped together such as these are not likely to be entirely due to solar wind conditions, for three reasons: (1) Solar wind density and speed vary on much smaller timescales than the accumulated durations of these ~10 orbits [*Gershman et al*., 2012; *Baker et al*., 2012]. (2) Periods marked by a negative Z component of the IMF, $B_{Z,IMF}$, required for enhanced dayside reconnection and solar wind precipitation [*Massetti et al*., 2003; *Sarantos et al*., 2007] at the northern cusp, also vary on much smaller timescales [*Baker et al*., 2012]. (3) Finally, the He^{2+} distribution (not shown) does not show obviously higher n_{obs} in these same orbits, as would be expected for this to be a solar wind effect. An examination the dependence of total observed density on Mercury TAA (below) sheds more light on these enhancements.

These projections are a clear reminder that these measurements are made up of individual orbits and are actually quite sparse on the scale of Mercury's space environment. This fact dictates many of the possible avenues for global analysis.

5.3.2 Variation with Mercury TAA

The average observed density for each of the three planetary ions is plotted as a function of Mercury TAA in Figure 5.2c. Since the TAA changes by ~5° per day, measurements are collected into bins of 10° width to smooth the data. To facilitate comparison, the average observed densities for O^+-group ions and He^+ are multiplied by a factor of 5.

There are three prominent peaks for Na^+-group ions, centered at TAA ~ 110°, 150°, and 330°. These peaks show some qualitative similarities to peaks in neutral Na predicted by exospheric models [*Leblanc and Johnson*, 2010; *Wang and Ip,* 2011] and observed from Earth [*Potter et al*., 2007]; this comparison is examined in detail in Section 5.4.2. O^+-group ions follow the same trends, at a nearly constant 20% fraction of the observed density of the Na^+ group through much of the Mercury year. The exception is for TAA 110–180°, for which O^+-group ions are not strongly enhanced, unlike Na^+-group ions. He^+ ions behave quite differently. Except for some very small enhancements, the clear peaks seen in Na^+-group ions are absent. He^+ ions show a nearly constant average observed density throughout the Mercury year.

When interpreting these results, one must remember that the local time of MESSENGER periapsis is locked to Mercury season and TAA. Therefore, each of the peaks in Figure 5.2c are from measurements taken at particular local time of periapsis and Mercury–Sun distance. FIPS does not provide an instantaneous global measurement. The spacecraft was at periapsis for local times in the 19−20.5 h range for the peaks at TAA ~ 110° and 150°, when Mercury was approaching its aphelion of 0.47 AU from the Sun. For the TAA ~ 330° peak, MESSENGER periapsis was at local times in the range

6.5–11 h (Figure 5.2b) and moving away from its perihelion of 0.31 AU. The predicted peak in exosphere content at aphelion, at TAA=180° [*Leblanc and Johnson*, 2010], coincided with a time when MESSENGER was above the dusk terminator. In principle, then, it is impossible to attribute conclusively the enhancements in Figure 5.2c to seasonal variations. We will return to this question below.

5.3.3 Variation with Altitude and Local Time

A major source of ions measured by FIPS is expected to be photoionization of exospheric neutral atoms. This process takes place at all altitudes and without regard for magnetic boundaries, depending mainly on the neutral atom generation and convection processes. Therefore, in sunlight the observed density of ions is expected to show a strong dependence on altitude. Once formed, ions are also subject to the magnetic and electric field forces in the environment, which complicates analysis of altitude profiles. In eclipse, of course, no photoionization takes place, making electromagnetic forces the primary sources of influence.

An overview of the dependence of average observed density on local time and altitude for the four ions species considered in this study is shown in Figure 5.3. These maps were created by binning the observations by altitude (100 km bin width) and local time (0.5 h bin width) and further separated into 60° latitude ranges, with the same normalization and color scheme as for Figures 5.2a and 5.2b. These maps show a variety of enhancements and a general altitude profile that is different for each ion species. Altitude profiles will be discussed in more detail in Section 5.3.3.1.

The Na^+-group ions show an enhancement at high latitudes (Figure 5.3a, feature 1), centered at local time ~10.5 h, which corresponds, at least in part, to the northern

magnetic cusp. An additional enhancement is centered at local time ~19 h (Figure 5.3a, feature 2). Around the equator (Figure 5.3b), an enhancement is evident around the dawn terminator (local time 6, feature 3), consistent with some neutral and ion transport models (see section 5.4.2 below). Another enhancement is located in the pre-midnight sector, (local time ~20 h), at altitudes above ~2000 km, similar to the one evident in Figure 5.3a, feature 2. This latter enhancement extends to low latitudes (Figure 5.3c, feature 5) to an altitude of ~6000 km. Slices through the Cartesian binning of the data (similar to Figures 5.2a and 5.2b, not shown) confirm that these three enhancements (features 2, 4, and 5 in Figure 5.3) appear to be part of a single feature that creates a large asymmetry between dawn and dusk.

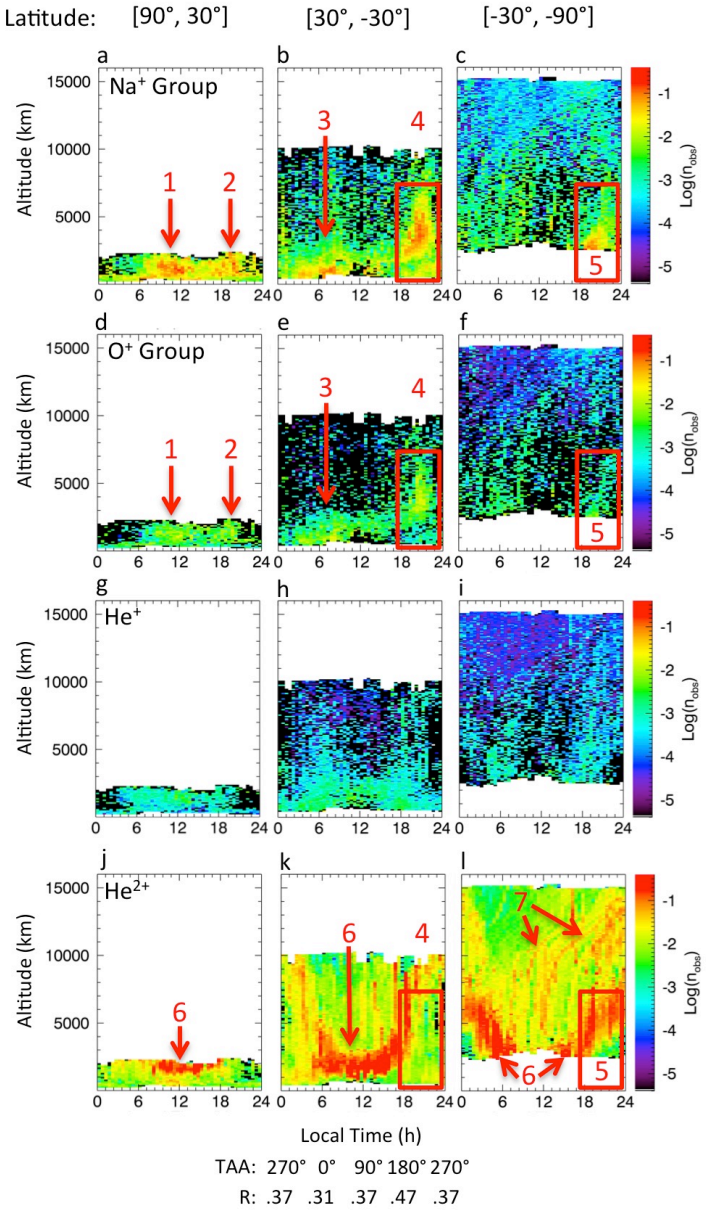

Figure 5.3. Average observed ion density (cm^{-3}) for all species as a function of altitude (km) and local time (h). Measurements are separated into three latitude ranges (inclusive). All ions are plotted on the same color scale, with the color bar for each panel showing the range present in that panel. Mercury TAA and heliocentric distance (*R*, in AU) are shown under panel k and apply to all panels.

The O^+-group ions (Figures 5.3d, e, and f) show the same major features (features 1-5), at lower average observed density, as the Na^+-group ions (Figures 5.3a, b and c). Close comparison between the two groups reveals that in some cases even the small-scale

structure is reproduced (features 2, 3 and 4). In other cases, only the large-scale structure is similar, with cells of particular high or low n_{obs} arranged a little differently (features 1 and 5). These differences may arise from the limited statistics for the low-abundance O^+-group ions and need not represent a global difference in the behavior of the two ion groups.

The most obvious feature of the He^{2+} map is the magnetosheath, visible as thick, nearly solid red bands (Figures 5.3j, k, and l, feature 6). Orbits with overall higher n_{obs} measurements are also evident, as narrow, right-turning trails (Figure 5.3l, feature 7). With these observations to guide the eye, it is possible to see some enhancements in the other ions at the same locations as those for He^{2+}. Features 4 and 5 from Figure 5.3 are also identified in Figures 5.4k and 5.3l, showing that these enhancements only partially overlap the magnetosheath. This enhancement may be related to the magnetopause-associated heavy ions that are commonly seen in individual passes through the magnetosphere [*Zurbuchen et al*., 2011].

He^+ ion maps do not show the same clear enhancements as the Na^+-group ions, but instead they are much more evenly distributed around the planet. The average observed density spans only two orders of magnitude, 10^{-4} to 10^{-2} cm^{-3}, rather than the five orders of magnitude spanned by Na^+-group ions. Low-altitude enhancements are present, but they are much less pronounced than for the Na^+-group and O^+-group ions. These patterns likely indicate a different source for He^+ than for Na^+-group and O^+-group ions. One possible source is charge exchange between solar wind He^{2+} and exospheric neutrals, gravitationally bound and/or escaping. If this mechanism were a dominant source, then charge exchange would be most prevalent where He^{2+} density is the highest – in the

magnetosheath region. Comparison of Figure 5.3h to Figure 5.3k and Figure 5.3i to Figure 5.3l suggests that unlike other planetary ions, slight enhancements in the He^+ distribution may be present in the magnetosheath (bright red bands in Figures 5.3k and 5.3l)

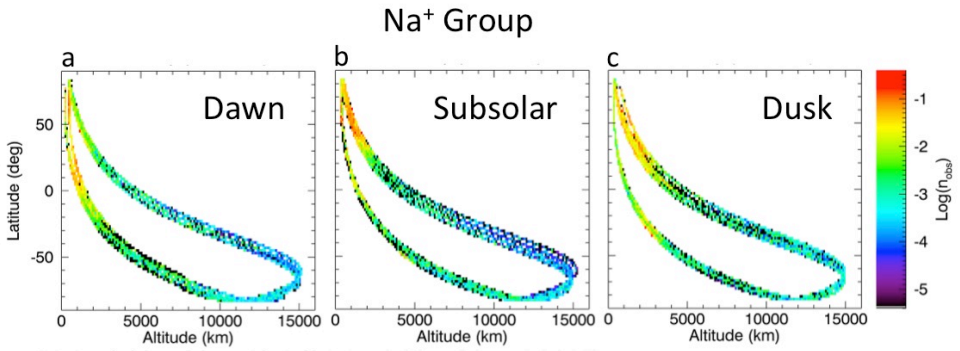

Figure 5.4. Altitude profiles of Na^+-group ions obtained from summed orbits. Observed density is binned by latitude (0.5° bin widths) and altitude (100 km bin widths) and averaged, analogous to Figure 5.2. See text for further details. These figures show the interconnection of latitude and altitude resulting from MESSENGER's highly eccentric orbit.

Because of differences between measurements in sunlight and eclipse, we consider the two sets of measurements separately in the quantitative analyses in the next two sections. The eclipsed region is defined as measurements taken when the spacecraft was in the shadow within 1 R_M perpendicular distance of the $-X_{MSO}$ axis. Everywhere else is considered sunlit.

5.3.3.1 Ion e-folding heights

In sunlight, we can quantify the altitude dependence of Na^+-group, O^+-group, and He^+ ions by estimating an *e*-folding height. We intentionally avoid the use of the term "scale height" to emphasize that this quantification is only mathematical in nature and is independent of any physical interpretation. Because these altitude profiles are fit

reasonably well by an exponential function, *e*-folding height provides a useful metric for comparison.

We subdivided the observed density for each of these three species into 3-h regions of local time, centered on the dawn terminator (local time 6±1.5 h), subsolar point (local time 12±1.5 h), and dusk terminator (local time 18±1.5 h). The orbits in each of these ranges, summed and plotted versus latitude in Figure 5.4, show the close coupling of altitude and latitude due to MESSENGER's highly eccentric orbit. Observed density was then summed over latitude, to produce profiles of observed density versus altitude alone (Figure 5.5). These altitude profiles show clear differences among species and local time regions.

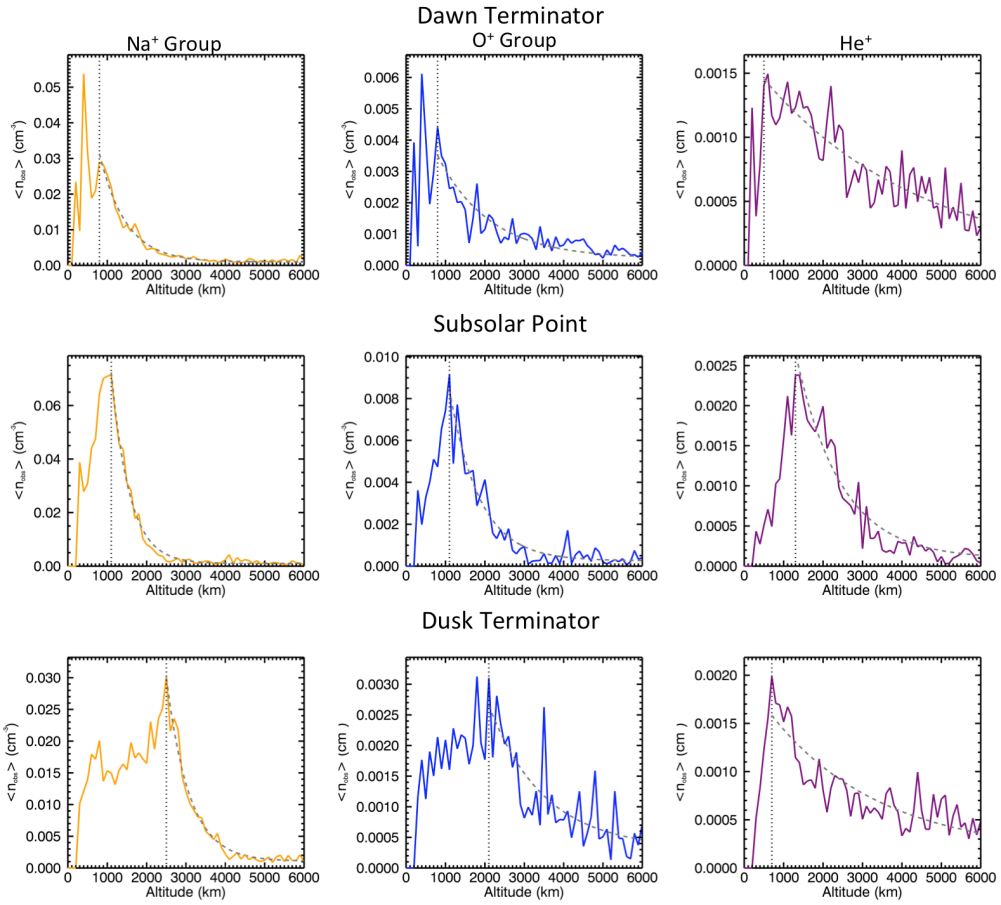

Figure 5.5. Altitude dependence of observed density in sunlight, over all latitudes, for three species in three regions of local time. The vertical dotted line denotes h_0 from Table 2. The exponential curve generated from the corresponding B value (Table 2) is also shown (dashed curve).

We fit the dependence on altitude (h) of the observed density (n_{obs}) to a function of the form:

$$n_{\text{obs}} = Ae^{-\frac{(h-h_0)}{B}} + C \qquad (5.1)$$

where A, B, and C are determined by a least-squares fit to the data. The peak altitude (h_0) denotes the portion of the data we chose to fit; it is the altitude at which the observed density starts to fall off clearly with altitude. The B parameter represents the e-folding height of the ions, the height at which the observed density has decreased by $1/e$ from the

value at h_0. (The C parameter, which is very small, has negligible influence on the e-folding height.) To estimate the uncertainty in these fits, we used a bootstrap method [*Hesterberg et al.*, 2010; *Hesterberg*, 2011] as follows: We produced 1,000 bootstrap samples of the altitude profile by randomly sampling with replacement from the measurements within each 100-km-wide bin. The distribution with altitude of the binned means in each bootstrapped sample was fit with the exponential function (Figure 5.6a) to produce a distribution of e-folding distances that reflect the expected sampling variability (Figure 5.6b). The h_0 and average B values are the most physically relevant and are tabulated in Table 5.2. To facilitate comparison across local times, the B values at dawn and dusk are divided by B at the subsolar point for a given ion species. These values are shown in parentheses in Table 5.2.

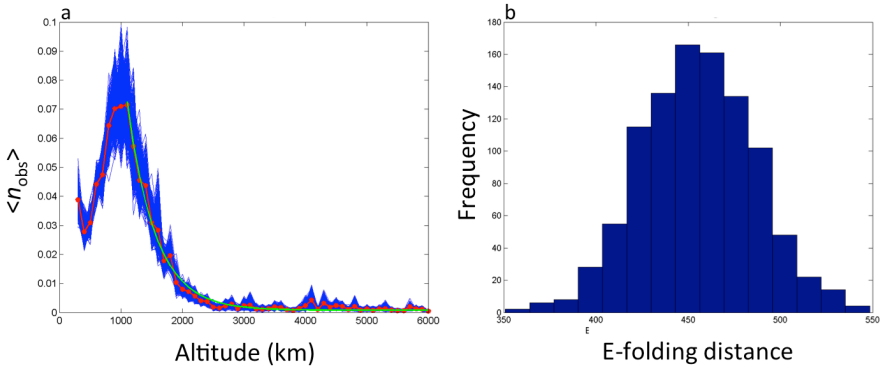

Figure 5.6. Estimation of e-folding distance error for Na^+ over the subsolar region. (a) Comparison of 1,000 curves constructed from chosen bootstrapped samples of data in 100-km altitude bins (blue) with the average curve (red). (b) Distribution of e-folding distances derived from exponential fits to each of the curves in (a), from which the average e-folding distance was computed. The curve produced from that average e-folding distance is shown in green in (a).

For the Na^+ group, the e-folding height shows a clear dependence on local time, with a much smaller B in the subsolar region than at the terminators. This pattern is consistent with the expected behavior of neutral Na, as the result of increased radiation pressure at the subsolar point [*Mura et al.*, 2007]. O^+-group and He^+-ions show the same smaller e-

folding height at the subsolar point than the terminator regions. He^+ ions are much more extended than the other two, and their measured distribution is substantially more extended at the dawn terminator. The implications of these differences are discussed in Section 5.4.

Table 5.2. Peak altitude (h_0, km) and *e*-folding distance (B, km) from fits of average observed density versus altitude at three local times.

Local Time		Na^+ group	O^+ group	He^+
Dawn	B	670 ± 40 (1.5)	1330 ± 250 (1.8)	4040 ± 300 (3.6)
	h_0	800	800	500
Subsolar	B	460 ± 30 (1)	760 ± 70 (1)	1140 ± 90 (1)
	h_0	1100	1100	1300
Dusk	B	580 ± 40 (1.3)	1400 ± 300 (1.8)	2790 ± 350 (2.6)
	h_0	2500	2100	700

Notes: Values in parentheses are ratios to the *e*-folding distance at the subsolar point for a given ion. h_0 is the altitude above which these *e*-folding distances were obtained.

For the Na^+ group, the *e*-folding height shows a clear dependence on local time, with a much smaller B in the subsolar region than at the terminators. This pattern is consistent with the expected behavior of neutral Na, as the result of increased radiation pressure at the subsolar point [*Mura et al*., 2007]. O^+-group and He^+-ions show the same smaller *e*-folding height at the subsolar point than the terminator regions. He^+ ions are much more extended than the other two, and their measured distribution is substantially more extended at the dawn terminator. The implications of these differences are discussed in Section 5.4.

The quantity h_0 denotes the altitude above which an *e*-folding scale height can be well defined. The h_0 values for Na^+-group and O^+-group ions gradually increase from dawn to subsolar to dusk, whereas He^+ ions do not show this trend. This behavior for the heavy ions does not appear to be an effect of the FIPS pointing and its limited FOV. The angle between FIPS boresight vector and the nadir direction can be used to generally assess pointing as a function of altitude and local time. Though there are differences in this angle between the dawn and dusk regions, it stays within 75°, so that the planet is within the FOV most of the time in both regions. Seasonal variations may play a role: The dusk-side observations are taken when Mercury's heliocentric distance is near maximum (0.47 AU), whereas it is near minimum (0.31 AU) for the dawn and subsolar measurements.

5.3.3.2 Composition dependence on local time

To extend quantitatively the comparison of composition in the dusk terminator, subsolar, and dawn terminator regions, the average observed density in each was calculated and plotted (Figure 5.7). In Figure 5.7a, data only from ±30°N latitude were used. In Figure 5.7b, these averages were obtained from data at all latitudes. All altitudes were included in both panels. The average observed densities from the cusp region, defined broadly here as 6–18 h and 45°–90° latitude, was added to both panels for comparison. The statistical errors in these averages are < 1%.

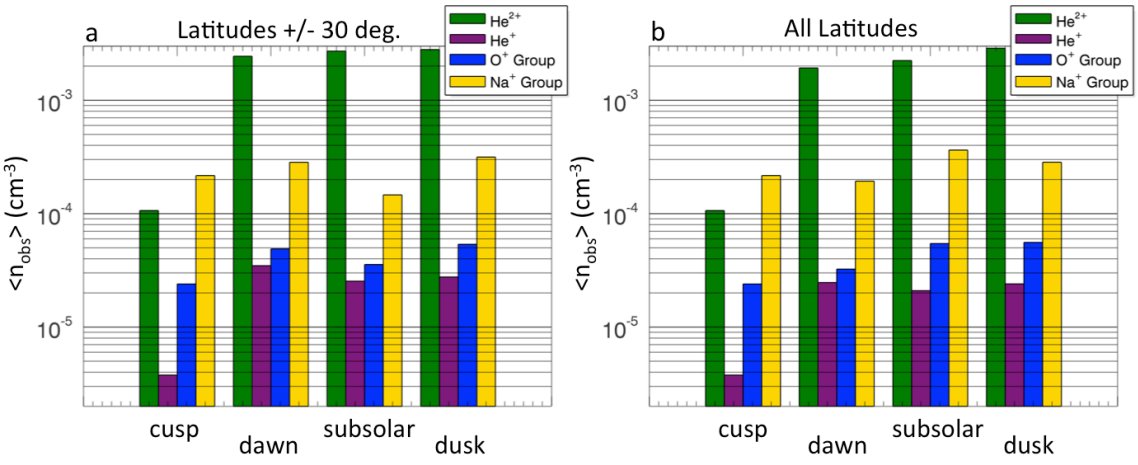

Figure 5.7. Ion composition on Mercury's dayside for two latitude ranges. Shown are n_{obs} averaged over all measurements, including all altitudes and the indicated range of latitudes and local times. The cusp observations are the same in both panels. Statistical errors in these averages are < 1%.

The most interesting feature of the cusp composition is that the average observed density of Na^+-group ions in the cusp exceeds that of He^{2+} by a factor of ~ 2. (Even though observed density for Na^+-group ions exceeds that of the solar wind tracer, He^{2+}, protons are still the dominant plasma in the cusp during most, if not all, orbits.) It may be possible to use this very high ratio of Na^+-group to He^{2+} ions as a compositional marker for cusp plasma. If so, then tracking of plasma convection from the cusp to other regions of the magnetosphere might be enabled. Of course, this large ratio would need to be verified by examining a large number of individual orbits.

Around the equator (±30° latitude, Figure 5.7a), average observed density for all ion groups is depressed at the subsolar point, the same trend observed in *H* values above. For Na^+-group ions, the subsolar n_{obs} is 49% of the average of the dawn and dusk values. O^+-group and He^+ n_{obs} values are depressed less, with subsolar averages that are 69% and 81% of their respective dawn-dusk averages. This effect is inverted for Na^+ and O^+

groups when all latitudes are included: The n_{obs} values at subsolar local times, which include the large plasma source of the cusp, are enhanced relative to the dawn and dusk regions.

For observations during eclipse, a fairly small fraction, we focus on measurements in and around the central plasma sheet, within 750 km of the geographic equator. This volume includes the magnetic equator, which is shifted north of the geographic equator by ~500 km [*Anderson et al*., 2011]. These plasma sheet observations were further subdivided into pre-midnight, occurring between local times of ~21 and 0 h (midnight) and post-midnight, occurring between local times of 0 and ~3 h. (The precise local time bounds are determined by the eclipse condition, described above.) Because of MESSENGER's orbit, these restrictions produce observations that lie entirely within two narrow altitude bands, each about 1000 km thick, and centered at altitudes of ~600 km and ~3600 km (Figure 5.8a). These bands are too restricted to be used to analyze the functional dependence of observed density on altitude. The average n_{obs} values for Na^+-group ions, O^+-group ions, He^+, and He^{2+} were each summed for all measurements within these two regions. The results are displayed in Figure 5.8b.

The main result is a persistent enhancement in Na^+-group ions by a factor of 1.6 in the pre-midnight sector compared with the post-midnight sector. This enhancement is visible in both the inner and outer ring in Figure 5.8a. The enhancement around the dawn terminator, seen in Figure 5.3, is also apparent. On the contrary, none of the other ion species show this enhancement. We will return to these results in Section 5.4.6.

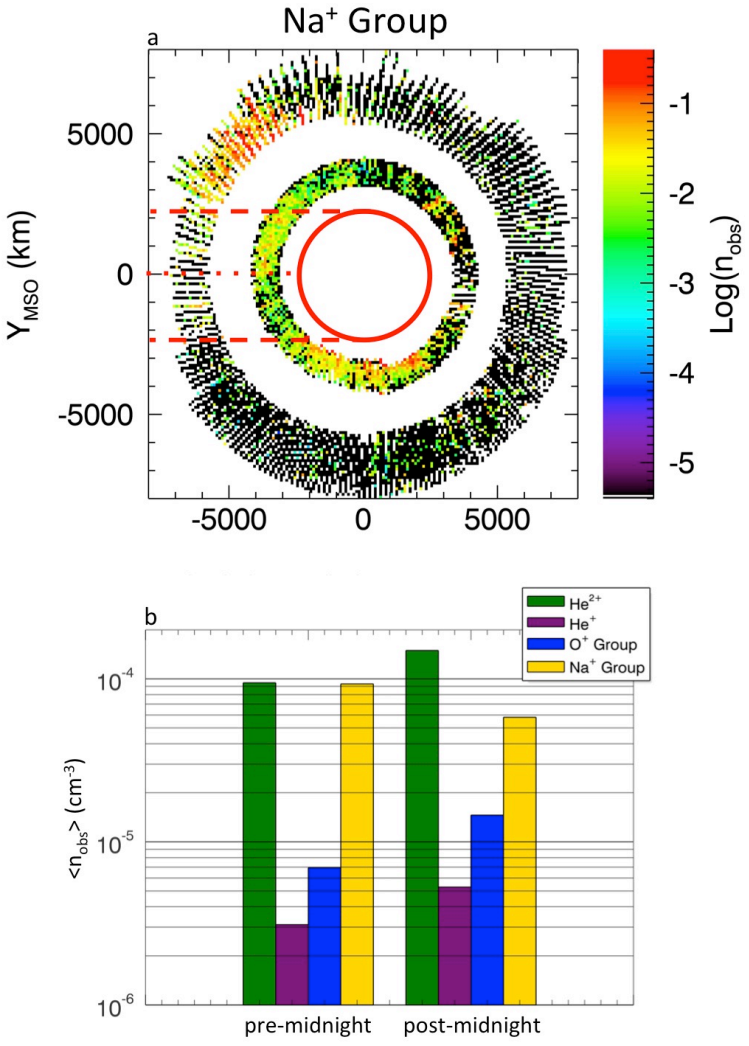

Figure 5.8. (a) Equatorial cross section of average observed density, from observations within 750 km of the geographic equator. Measurements are normalized by the number of FIPS scans within each 100 km × 100 km bin, as in Figure 5.2. Statistical errors are < 1%. A red circle shows the approximate size of Mercury in the equatorial plane. The Sun is to the right. (b) Average observed density on the nightside, including only measurements from (a) that were collected while MESSENGER was in the shadow of Mercury, delineated by dashed red lines. A dotted red line separates the pre-midnight sector (top) from the post-midnight sector (bottom) within the shadow.

5.4 Discussion and Implications

The observations presented in this paper provide a fresh perspective on previous studies of ions and neutral atoms in Mercury's environment. There are inherent similarities and differences expected between these two populations. The neutral

exosphere is likely the major source of ions at Mercury, so if measured soon after ionization the ions may retain some characteristics of the neutral atom population, such as spatial distribution. Yet because ions and neutrals are controlled by different forces, ions measured long after ionization will show a much less direct relationship to the population of neutrals. In making these comparisons, our aim is to begin to differentiate between these two situations.

5.4.1 Overall Composition

It is clear that the Na^+ group dominates the planetary ions (Table 1), consistent with expectations from ground observations and photoionization rates [*Killen et al*., 2007] and previously reported measurements at Mercury [*Zurbuchen et al*., 2008, 2011]. As discussed in the Appendix, the average density measured in this group likely comes from a combination of Na^+ and Mg^+ ions, produced both by photoionization of exospheric neutrals and sputtering of the surface. Production rates of Mg^+ from the exosphere should be much less than that of Na^+ if neutral Mg densities inferred from second flyby data are representative [*Sarantos et al*., 2011], but the relative effect of surface-generated ions on our measurements is difficult to estimate at present. Average observed densities for Na^+-group and O^+-group ions obtained during the flybys are quite comparable to orbital values, within the larger statistical uncertainty resulting from poorer counting statistics. He^+ and He^{2+} measured during the flybys, in contrast, are much different from their orbital averages. Flyby averages were taken from magnetospheric data only, which likely accounts for a substantial drop in He^{2+}. However, He^+ actually had a larger average observed density during the flybys than found in the orbital data. The flyby trajectories were much different from MESSENGER's orbit, because the spacecraft passed from

deep in the magnetotail in pre-midnight, past the dawn terminator close to the planet, to the dayside. The deep tail observations obtained during M1 and M2 are not matched in the orbital data, and it is possible that this different sampling contributed to the observed differences in He^+.

5.4.2 Variation with TAA

We return to the variation of observed ions with TAA in Na^+-group ions (Figure 5.2). *Leblanc and Johnson* [2010] modeled the total Na content of the Mercury exosphere through a full Mercury year, adjusting the contributions of the various production processes to explore their effects. They then calculated Na brightness and compared that prediction with trends versus TAA from ground-based observations. They predicted a factor of 3 variation in exospheric Na content as a function of Mercury true anomaly, with minima of 1.5×10^{28} Na atoms at TAA = 140° and 70° and maxima of 4.5×10^{28} Na atoms at TAA = 180° and 0° (their figure 12). Their figure 11 shows that that the peak at TAA = 180° is due the dominance of photon-stimulated desorption and solar wind sputtering, whereas thermal desorption is the dominant process producing the peak at TAA = 0°.

If we consider the two Na^+-group ion peaks (which are very close to one another) as representing one peak at ~130°, then FIPS ion measurements show two peaks separated by ~200°. This separation is within 10% of that predicted by *Leblanc and Johnson* [2010]. Clearly their modeling results do not fully explain observed differences in Na^+-group distribution reported here. For example, in sunlight, a large enhancement is seen only on the dawn side, for TAA = 0°, whereas the modeling predicts enhancements on the dusk side (TAA = 180°) as well. In general, their results show peaks centered at TAA

= 40° and TAA = 300°, although results from different specific models showed substantial variations.

Variation of Na D_2 emission with TAA was reported from ground observations by *Potter et al*. [2007]. Their figure 1 shows a two-peak structure, in which the first peak is split, a pattern qualitatively similar to FIPS observations (Figure 5.2c), except that the TAA values for the peaks are shifted. As shown by *Potter et al.* [2007], these peaks are centered at TAA ~ 70° and TAA ~ 300°, whereas the peaks in the FIPS measurements are at TAA ~ 130° and TAA ~ 330°. *Potter et al.* [2007] offered that radiation acceleration has a varying affect on this emission over a Mercury year, and so emission does not relate directly to column abundance of Na. They normalized their emission data to one set of conditions. Their figure 2 shows Na emissions that should be directly related to column abundance. These normalized emissions do not compare well to FIPS observations (Figure 5.2c), however. *Wang and Ip* [2011] modeled these Na D_2 emissions and found total Na emission peaks at TAA = 90° and 310°. Their study did not involve calculation of Na content, which differs from emission by a TAA-dependent radiation acceleration term. Nonetheless, it is interesting to note that their results show two peaks separated by ~220°, which is also within 10% of the 200° separation of the peaks in FIPS Na^+-group ions.

5.4.3 Dayside Planetary Ion Distribution

Delcourt et al. [2003] modeled Na^+ in Mercury's magnetosphere with a simplified version of the exosphere model of *Leblanc and Johnson* [2003] and analytic expressions for the magnetic and electric fields. Na^+ particles were launched from a variety of locations and with a variety of energies, then flown through the model magnetosphere by

integrating the full equations of motion. Their results show that the dayside magnetosphere, local time ~8-16 h, is populated with very-low-energy ions having energies < 100 eV. During the orbital observations reported in this study, FIPS was operated with two minimum energies: 100 eV in burst mode (8 s time resolution) and 46 eV in normal mode (64 s time resolution). Typically, FIPS was in burst mode on the dayside, within a few R_M of the surface. It is possible that this 100 eV energy threshold near the planet could partially account for the generally lower average n_{obs} values at the subsolar point. If ions were present, they may have been below the FIPS energy threshold and thus unable to be measured. In February 2012, the FIPS burst-mode energy threshold was lowered to 46 eV. Analysis of these data, outside the range considered in this study, should provide fresh information on this point.

Other features of the FIPS-derived ion spatial distributions correlate with previously published results or predictions for Na neutrals. Some exospheric simulations predict a dawn enhancement of neutral sodium [*Leblanc and Johnson*, 2003, 2010; *Misawa et al*., 2008]. *Yagi et al*. [2010] carried out simulations in which Na^+ test particles were tracked through electric and magnetic fields derived from a magnetohydrodynamic model, using the same exospheric model as that of *Delcourt et al.* [2003]. They studied Na^+ behavior under four distinct sets of solar wind conditions. In all cases, their simulations showed enhancement of Na^+ density in the morning sector, over the local time range 6–12 h. As seen in Figure5. 2c, FIPS results show a peak in Na^+-group and O^+-group ions when MESSENGER periapsis was in this local time range. (The local time ranges in Figure 5.7 are not conducive to observing this enhancement.). The fact that average observed density for Na^+ group ions in the cusp exceeds that of He^{2+} is consistent with the cusp

serving as a major source of planetary ions due to increased surface exposure to solar wind sputtering [e.g., *Massetti et al*., 2003; *Sarantos et al*., 2007; *Benna et al*., 2010]. The cusp is a strong source of planetary ions, as evident in these measurements, and may also serve to trap planetary ions that are created from escaping neutrals in the magnetosheath.

5.4.4 Altitude Dependence

The functional fits of observed dependence on altitude yield many differences and reflect a combination of competing effects. First, escape of neutrals from Mercury's gravity under the influence of radiation pressure yields a neutral density that peaks at the surface then generally drops off as the inverse of altitude. Because Mercury's exosphere is considered optically thin above ~50 km altitude, the number of photons is constant with altitude. Therefore, the production of ions by photoionization is simply proportional to neutral density. If these ions are measured close to the time that they are created by photoionization, they could serve as a tracer for the neutral atom density. However, as the time between photoionization and measurement increases, the influence of plasma processes increases as well. One way to separate these two regimes would be to limit the altitude consideration to low altitudes (< 2000 km) at which the effects of convection should be minimal. However, the observed flux typically peaks near this altitude and begins to fall off at higher altitudes.

One option for the interpretation of the *e*-folding distance is as a scale height, as is done for gravitationally bound exospheric neutral atoms. For neutral species, scale height reflects the ratio of particle mean energy to the potential in which the particles find themselves, which includes only gravity in the simplest scenario:

$$H = \frac{kT}{mg}$$

The scale heights of various exospheric components at the same "temperature" T (i.e., mean ejection velocity from the surface) are therefore different by the ratio of their masses. Thus, comparing Hm gives information about the temperature of the neutral populations. Interpreting the ion *e*-folding distances calculated in this work as scale heights raises several issues. Even at 1000 km, the altitude at which observed density typically peaks, a Na^+ ion has the gravitational potential energy of ~2.4 eV. When compared with the high average energy measured for the ions (~2–4 keV), gravity is negligible. Furthermore, measured He^+ exhibits very large *e*-folding heights, whereas the He neutral atoms are expected to be accommodated to Mercury's surface temperature, ~700 K. The variation of *e*-folding heights among species is more likely related to variation in the ratio of ion gyroradius to neutral scale height [*Hartle et al*., 2011].

These results can also be interpreted in the context of average magnetospheric boundary locations. From a statistical analysis of MESSENGER Magnetometer observations, *Winslow et al*. [2012] showed that the average altitude of the subsolar magnetopause is 1100 km, and the maximum altitude is 1340 km. Those authors also found that the average altitude for the subsolar bow shock is 2340 km, and the maximum altitude is 2660 km. In the subsolar region, FIPS measurements show peaks in n_{obs} in the range of the *Winslow et al*. [2012] magnetopause locations. This agreement is consistent with expectations, in that planetary ions formed from neutrals upstream will tend to collect at the subsolar magnetopause where plasma flow velocity is low [*Spreiter et al.*, 1966]. Moreover, planetary ions that form in the dayside magnetosphere or flow into that region will tend to gyrate across the magnetopause and out of the magnetosphere because

of their large gyroradii. This effect should be most pronounced in the subsolar region, where the distance from the surface to the magnetopause is at a minimum.

Interpretation of these differences is further complicated by the possibility that different species are present with substantially different distribution functions. In the simplest case, consider He^+ ions that are much hotter than Na^+-group ions. Such a scenario might follow from the much larger *e*-folding distance for He^+. In such a case, He^+ would be more easily measured by FIPS with its limited FOV, especially at larger convection speeds that might be present at larger altitudes.

5.4.5 Source of He^+

The measurements reported here show that He^+ is distributed differently from the other two planetary ion groups observed in abundance at Mercury, the O^+-group and Na^+-group ions. He^+ at Mercury may be created by charge exchange between He^{2+} and any neutral atom or by ionization of exospheric He from the surface. He^+ created by charge exchange should show enhancements where He^{2+} density is the highest – in the magnetosheath. Though some enhancements in He^+ are visible in this area (Figures 5.3h and 5.3i), there is only partial correlation with magnetosheath enhancements in He^{2+} (Figures 5.3j, 5.3k, and 5.3l). The even distribution of He^+ is consistent with the distribution of a He exosphere given by several models [e.g., *Hartle and Thomas*, 1974; *Hartle et al.,* 1975; *Leblanc and Chaufray*, 2011]. Thus the distribution of He^+ in the FIPS measurements presented here qualitatively supports ionization of exospheric neutral He as the more important source for He^+ than charge exchange. However, the ultimate source of He in those models is from surface implantation by the solar wind. In that

light, the fact that He^+ is depleted in the cusp measurements, contrary to the other two planetary ion groups, requires further explanation.

5.4.6 Nightside Distribution of Na^+-group Ions

As described above, the nightside (eclipse) measurements show the interesting result that the Na^+-group flux is higher on the pre-midnight side than on the post-midnight side (Figure 5.8). MESSENGER periapsis was in the pre-midnight sector for Mercury TAA = 100° to 140° (Figure 5.2c). The pre-midnight sector is where we expect to find Na^+ ions moving under the influence of gradient-curvature drift, the velocity imparted clockwise around the planet (when looking down from north) by the combined effects of magnetic field gradient and curvature. However, high magnetic field gradients make pure drift motion unlikely around the magnetic equator and in the central plasma sheet [*Lukyanov et al*., 2001], where the pre-midnight enhancement is most prominent.

As discussed above, *Yagi et al*. [2010] simulated Na^+ behavior within Mercury's magnetosphere under four distinct sets of solar wind conditions. In all cases, Na^+ was found to be enhanced from local time ~1 to 11 h. Direct comparison of their results with FIPS observations is complicated by the fact that solar wind and IMF conditions encountered by MESSENGER varied over a wide range [*Baker et al*., 2012]. However, it is safe to conclude that, since the model results never showed an enhancement on the pre-midnight side, the model results do not show the same behavior as the observations in this regard. One reason may be the fact that the bulk of Na^+ energies were below 5 keV in the model, whereas FIPS observed substantial fractions of the Na^+ group population with energies up to 10 keV.

Delcourt et al. [2003] found that Na^+ ions launched from the region of the northern cusp were substantially energized (up to 10 keV) and precipitated on the pre-midnight side of the planet, unless their gyro-motion took them out of the magnetosphere first. These authors credited this behavior to non-adiabatic motion, driven largely by the small size of Mercury's magnetosphere and the large Na^+ gyroradius. These results qualitatively match the observations described in this work, particularly the enhancement in observed density of Na^+ group ions on the pre-midnight side in eclipse. These FIPS measurements may constitute the first observational evidence of large-scale non-adiabatic motion of heavy ion particles in Mercury's magnetosphere.

We recall here that only Na^+-group ions show the pre-midnight enhancement in eclipse; the other ion species do not (Figure 5.8a). Non-adiabatic motion depends on gyroradius, which increases with *m/q*. The gyroradius of Na^+-group ions is nearly 50% larger than that of O^+-group ions (and much larger than He^+ and He^{2+}). This difference may be enough to account for the difference in behavior.

5.5 Summary and Conclusions

In this work, we have presented an overview of ion measurements made by the FIPS sensor during the first three Mercury years of MESSENGER orbital observations, from 25 March 2011 through 31 December 2011. We used two-dimensional spatial maps, functional fits, and regional averaging of observed densities as the main tools in this analysis. We have provided the first comprehensive overview of the heavy ion composition at Mercury and, where possible, drawn connections to previously published observations, models, and physical explanations.

We find the following:

(1) He^{2+} ions are the second most abundant ion (after protons), with an average observed density of 3.9×10^{-2} cm^{-3}. Na^{+}-group ions are next most abundant, with an average observed density of 5.1×10^{-3} cm^{-3}, followed by O^{+}-group ions (8.0×10^{-4} cm^{-3}) and He^{+} (3.4×10^{-4}).

(2) The average observed density of Na^{+}-group ions exceeds that of He^{2+} in the northern magnetic cusp by a factor of ~2. This ratio may be a compositional marker of the cusp.

(3) Within 30° of the equator and in sunlight, all planetary ions show minimum observed densities at the subsolar point. Near the equator, the average observed density of Na^{+}-group ions is reduced to 49% of the terminator value. Reductions are less for others species.

(4) All three planetary ion species considered show a different dependence on altitude and some differences with local time. Na^{+}-group ions fall off most strongly with altitude, followed by O^{+}-group ions and then He^{+}.

(5) In eclipse, Na^{+}-group ions are enhanced in the pre-midnight sector. Such an enhancement is consistent with modeling of Na^{+} energization and transport by *Delcourt et al*. [2003]. This pattern may be observational evidence that non-adiabatic effects are important in Mercury's magnetosphere on a large scale.

These results provide the first quantitative assessment of plasma composition at Mercury, its spatial variations, and temporal variations over an entire Mercury year. They give important clues to understanding exospheric and magnetospheric processes on the innermost planet.

5.6 Acknowledgements.

This work was supported by NASA's Graduate Student Research Program and the MESSENGER mission. The MESSENGER project is supported by the NASA Discovery Program under contracts NAS5-97271 to The Johns Hopkins University Applied Physics Laboratory and NASW-00002 to the Carnegie Institution of Washington. NASA's Astrophysics Data System has been used extensively for this work. JMR thanks Jonathan W. Thomas for designing and programming FIPS software libraries and Mark O. Stakhiv for suggesting one of the key visualizations used in this work.

5.7 Appendix: Ion Identification from *E/q* and TOF

After background removal, the next step in the detailed analysis of FIPS data is the assignment of individual counts to a particular ionic species. Because FIPS measures time of flight rather than *m*/*q* directly, this step is accomplished with a simple TOF forward model that is calibrated with flight data. The TOF forward model is comprised of the following:

$$E_{tot} = q\left[\left(\frac{E}{q}\right)_{ESA} - V_{PAV}\right] - E_{loss} \qquad (5.2)$$

$$v = 439\sqrt{\left(\frac{E_{tot}}{m}\right)} \qquad (5.3)$$

$$TOF = 10^4\frac{d}{v} - \tau_e - \tau_{MCP} \qquad (5.4)$$

Equation (5.2) relates the total energy (E_{tot}, in keV) to the *E/q* (in keV/e) measured by the electrostatic analyzer (ESA), the additional energy supplied by post-acceleration (V_{PAV}, a negative voltage, in kV), and the energy lost from passage through the carbon foil (E_{loss}, in keV). With E_{tot} in hand, the velocity (*v,* in km/s) of the ion in the TOF chamber can be

calculated via Equation 5.3. Finally, the expected TOF (in ns) is calculated via Equation 5.4. It is less than the ideal flight time, $10^4\ d/v$, where d is the flight distance (in cm) by the time required for electrons to travel from the carbon foil to the start microchannel plate (MCP) (τ_e, in ns) and detection times within the MCP (τ_{MCP}, in ns). In this work, τ_{MCP} was used as a small adjustable constant to optimize the fit of the TOF forward model to the data, and thus could be positive or negative. The same value of τ_{MCP} was used for all species.

The energy lost from passage through the carbon foil (E_{loss}) depends on the incident energy and mass of a particular ion, but not on the charge. This quantity was measured in laboratory calibrations for FIPS, but not for all possible ion species and energies. In this work, E_{loss} was derived from the modeled carbon foil interactions using the Transport of Ions in Matter (TRIM) software [*Zeigler* 2004; *Zeigler et al*., 2009]. For each element and total energy to be used in the analysis, 10^5 atoms were run through TRIM, producing a statistical distribution of energy loss values for that particular element and total energy combination. The peak energies for all of these runs were determined and used to make a polynomial fit of energy loss versus total energy for each element, shown in Figure 5.A1.

The forward model was implemented in a computer code that produced tracks in *E/q*–TOF space for each ion analyzed. These tracks were overlaid onto long accumulations of orbital data, from which specific ion tracks are clearly evident (Figure 5.A2). This procedure allowed for calibration of the model by comparison of the alignment of model tracks and measured tracks. The ability to see clearly the alignment of the modeled tracks with observed data from long accumulations allowed use of the same model under

much lower signal-to-noise ratios typically present when analyzing individual FIPS scans.

There are several limitations of this technique. Without being able to distinguish individual ion tracks, it is impossible to specify uniquely the set of ions identified in the analysis. Ions were selected that best fit the observations among those expected from studies of the neutral exosphere. Furthermore, where ion tracks overlap, due to TOF uncertainties (track width), no attempt was made to distribute statistically the counts to individual species. Rather, a composite track was constructed that includes the full range of TOF values for the corresponding group of ions. The consequences of this procedure are expected to be minor. Among the set of ions and groups chosen, no overlap was present.

Some estimation of the error in the reported abundances can be made. Systematic errors, partly due to TOF overlap described above, are estimated at ~20%. Additional errors come from uncertainties due to counting (Poisson) statistics. Thus, the total error (ε) is calculated from

$$\varepsilon = \sqrt{(0.20)^2 + \left(\sqrt{N}/N\right)^2} \tag{5.5}$$

where N is the number of counts. Since the errors are independent and random, they are added in Gaussian quadrature.

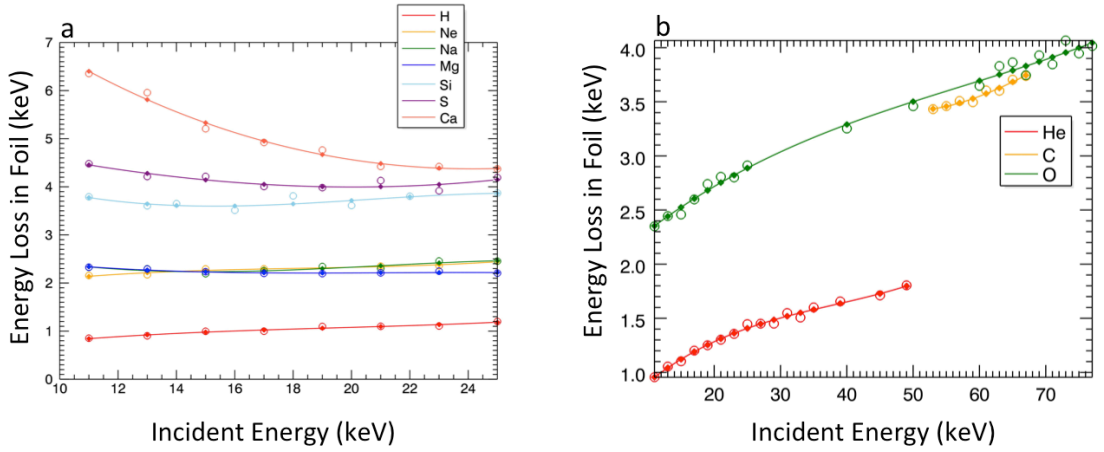

Figure 5.A1. Energy loss in foil as a function of total ion energy from TRIM simulations. (a) Loss over an energy range appropriate for singly charged ions. (b) Loss over a larger energy range reflecting additional energy gained in post-acceleration by multiply charged ions, up to O^{6+}.

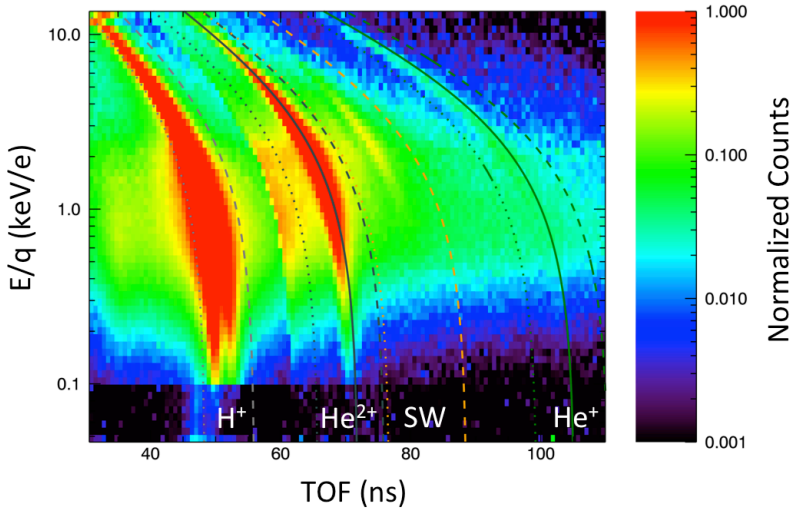

Figure 5.A2. Accumulated raw FIPS event data from 25 March 2011 through 22 November 2011 together with lines showing the lower (dotted) and upper (dashed) bounds on modeled TOF as a function of *E/q*, for each species. The modeled TOF center as a function of *E/q* (solid) is also shown for He^{2+} and He^{+}. Counts are normalized to the maximum value. Background removal has not yet been completed for the data shown in this figure. The darker region below 0.1 keV/e is due to less time spent observing in this energy range.

Chapter 6

Magnetospheric cusp structure and dynamics: MESSENGER FIPS measurements at Mercury

This chapter is taken from Jim M. Raines, Daniel J. Gershman, James A. Slavin, Thomas H. Zurbuchen, Haje Korth, Brian J. Anderson, George Gloeckler, Stamatios M. Krimigis, Sean C. Solomon (2013), Magnetospheric cusp structure and dynamics: MESSENGER FIPS measurements at Mercury, manuscript in preparation.

Abstract

MESSENGER has observed the northern magnetospheric cusp regularly since the spacecraft was inserted into Mercury orbit in March 2011. Observations from the Fast Imaging Plasma Spectrometer (FIPS), taken < 400 km from the surface, have shown the cusp observed plasmas to be second only to the magnetosheath for consistently high (>10 cm^(-3)) densities. This high plasma content is also reflected in strong diamagnetic depressions observed by the Magnetometer experiment (MAG). Plasma in the cusp may originate from several sources: 1) Direct inflow from the magnetosheath; 2) Locally-produced planetary photo-ions and ions sputtered off the surface from solar wind impact; 3) Magnetic field-aligned flow of magnetosheath and magnetospheric plasma accelerated from dayside reconnection X-line(s). In this work, we surveyed 518 cusp crossings,

focusing on the spatial distribution, energy spectra and also pitch-angle distributions of Na^+-group ions. We find that Mercury's cusp is a highly dynamic region, both in spatial extent and plasma composition and energies. On the average, Na^+-group ions are observed with high mean energies, 2-4 keV, and found in nearly isotropic pitch angle distributions. Both observations are inconsistent with direct transport of sputtered ions or newly photoionized particles into the cusp. The highest levels of observed densities and mean energies are strongly correlated with high levels of magnetic fluctuations attributed to flux transfer events along the magnetopause (option 3) above). Together, these results indicate that cusp Na^+-group ions are likely formed by ionization of escaping neutral Na in the outer dayside magnetosphere and magnetosheath followed by acceleration and transport into the cusp by reconnection at the subsolar magnetopause.

6.1 Introduction

Mercury's northern magnetospheric cusp has been apparent in MESSENGER observations [*Solomon et al.,* 2007] since the beginning of the orbital science mission on March 18, 2011. The Fast Imaging Plasma Spectrometer (FIPS) [*Zurbuchen et al.*, 1998; *Andrews et al.,* 2007] has detected enhancements in solar wind and planetary ion plasma in this region on nearly every orbit [*Zurbuchen et al,* 2011]. These enhancements span Mercury latitudes ~30°-80° and local times 6-14 hours. They are found in solar wind protons (H^+) and alpha particles (He^{2+}), as well as planetary ions (O+ group and Na+ group). Of the planetary ions, Na^+-group ions are particularly enhanced in the cusp, on average twice as abundant as solar wind alpha particles [*Raines et al.,* 2013]. Depressions in the magnetic field have been also been observed by the MESSENGER Magnetometer [*Anderson et al.*, 2007] (MAG), always co-located with plasma

enhancements indicating that they are diamagnetic in nature. As such, these depressions result from the superposition between the main magnetic field and the induced magnetic field of gyrating ions directly opposing the dipole field of Mercury. Winslow et al. [2012] used these diamagnetic depressions to perform a statistical study of Mercury's cusp region. Their analysis showed that the cusp is a broad, highly-variable region located around 56°-84° magnetic latitude and 7-16 hours local time. The size of Mercury's northern cusp is more similar to the V-shaped outer cusp at the Earth [*Smith and Lockwood*, 1996], which follows mainly from the very large volume occupied in the magnetosphere by Mercury itself. The high variability in the cusp is attributed to constantly changing solar wind conditions and magnetospheric dynamics, with dayside reconnection and tail loading likely playing a substantial role [*Slavin et al.,* 2010]. These variations in the cusp cause the area of Mercury's surface open to direct solar wind impact to be highly variable as well [*Kabin et al.*, 2000; *Massetti et al.*, 2003].

The goal of this study is to answer the following question about Mercury cusp plasma: Where do the Na^+-group ions observed by FIPS in the cusp originate and what are their major energization processes? Two scenarios are considered (Figure 6.1).

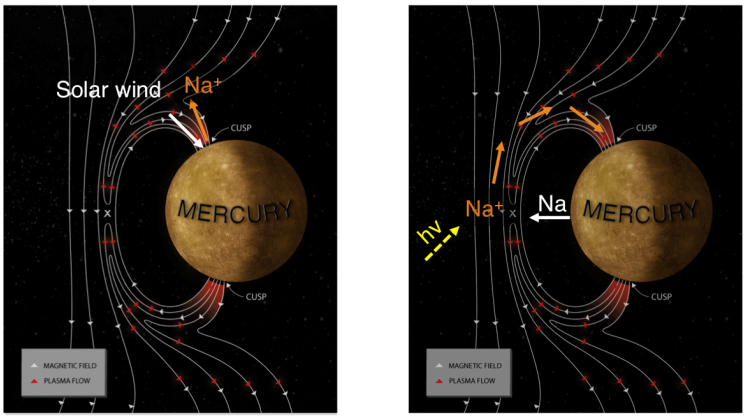

Figure 6.1. Two possible sources for Na^+-group ions in the cusp.

Since the cusp regions preferentially allow solar wind access to Mercury's surface, it may be reasonable to assume that Na^+ ions are created there by solar wind impact on the surface [*Lammer et al.*, 2003; *Leblanc and Johnson,* 2003; *Leblanc et al.*, 2010; *Massetti et al.*, 2003]. Solar wind ions impacting the surface with typical energies of 1-4 keV cause the release of surface-bound atoms. The effectiveness of this sputtering depends strongly on the impacting ion flux and its energy deposition properties, as well as many factors dependent on the surface composition, such as binding energy and nuclear stopping cross section [*Lammer et al.,* 2003]. The sputtered products are both neutral atoms (>90%) and ions (<10%), both of which are predicted by simulations to have energies in the 0.01-1 eV range [*Cassidy et al,* 2005]. Impact of solar wind electrons can also release surface-bound atoms in a process called Electron-Stimulated Desorption (ESD). ESD produces neutral atoms and ions in similar proportions to sputtering, but with higher energies, up to 10 eV [*McLean et al.*, 2011]. Neutral Na atoms are then subject to photoionization, though with an ionization lifetime of ~10,000 sec. [*Milillo et al.*, 2005], most travel away from the cusp on ballistic trajectories before being ionized. Ions are tied to the intrinsic magnetic field by the Lorentz force, so any velocity component parallel to the field would cause them stream away from the surface on magnetic field lines. At the altitudes that MESSENGER passes over the cusp (< 1000 km), the magnetic field lines are largely radial with respect to the planet, so ions streaming up from the surface should be detected by FIPS when it is oriented towards the surface.

There is, however, a second scenario: Neutral Na atoms can achieve ballistic trajectories on the dayside, provided they have enough energy. Some of these ions will be

photoionized right away within the magnetosphere and become trapped on dayside closed magnetic field lines, with no significant change to their kinetic energy. The remainder of these neutrals could pass through the magnetopause and even the bow shock, which present no barrier to uncharged species. Ions created by photoionization outside of the bow shock will be picked up into the solar wind and experience considerable acceleration. Likewise, ions created in the magnetosheath will be picked up at the local shocked solar wind flow speed. This flow speed varies from nearly stagnant at the subsolar point to a large fraction of the incident solar wind speed after ~45° away from the Sun-Mercury line [*Spreiter et al.,* 1966]. The fraction of the flow speed gained during pickup in the magnetosheath also depends on the orientation of the inter-planetary magnetic field (IMF) draping in the magnetosheath [*Slavin et al.*, 2008]. A larger magnetic field component perpendicular to the flow direction leads to more speed gained during pickup. Ions created in the solar wind or magnetosheath will therefore gain energy equivalent to up to two times the local flow speed. Those ions created outside of the bow shock will be further heated as they pass through the shock.

To evaluate the relative importance of each scenario, we surveyed MESSENGER plasma and magnetic field measurements of Mercury's Northern magnetospheric cusp over 518 orbits, collected from September 2011 through May 2012. During this time period,the FIPS instrument measured ions with energy per charge (*E/q*) in the range 0.046-13.3 keV/e and mass per charge (*m/q*) up to 60 amu/e. It has a large instantaneous field of view (FOV) of 1.4 π steradian, though ~0.25 π steradian is blocked by the MESSENGER spacecraft and sunshade. For all of the observations used in this study, FIPS' time resolution was about 8 seconds, the time required for a full *E/q* scan. We

focus on Na^+-group ions, a combination of Na^+, Mg^+ and Si^+ ions, ranging in m/q between approximately 21-30 amu/e [*Zurbuchen et al*, 2011]. For this heavy ion group, we report only *observed density,* which is the density calculated from the measured counts alone, with no attempt to correct for the fraction of the distribution sampled. We have reported true ambient plasma densities calculated from FIPS [*Raines et al.*, 2011; *Zurbuchen et al*, 2011] but those calculations often require assumptions which may not be generally applicable in the cusp and dayside magnetosphere region. See Raines et al. [2013] for more details of FIPS plasma measurements, observed density calculation and ion groups. MAG operated at its maximum time resolution of 20 Hz for all of the periods considered herein, providing three-dimensional magnetic field data at high cadence.

In this paper, we present representative examples of MESSENGER cusp crossings. We then use the observed properties of those examples to infer the likely origin of the observed Na^+-group ions and their major energization processes.

6.2 Cusp Examples

We analyzed cusp passages through a series of analyses as shown in Figure 6.2-6.5. In each of these figures, the top panel is the proton energy spectrogram in units of flux (counts s^{-1} cm^{-2} sr^{-1} kV^{-1}). The second panel shows the proton pitch angle distribution (arbitrary units). We use the proton pitch angle distribution in this study as a general indicator of plasma conditions in the cusp. With many more counts available, it is much easier to interpret for an individual scan (time step) than the Na^+-group pitch angle distribution. Here, our focus is on Na+ and not on protons and we therefore do not discuss in detail the observational signatures of this panel. The third panel shows observed number density (cm^{-3}). Four species are shown on this plot, alpha particles

(He^{2+}, green), He^{+}, O^{+} group and Na^{+} group. The fourth panel shows the energy spectrogram for Na^{+}-group ions. Because these energies are crucial to this work, these are given in phase space density (s^3/km^6), to be sure that FIPS sampling in velocity space is properly weighted [*Raines et al.*, 2011]. To make these energies easier to see in the figure, groups of 4 native energy bins have been combined in the figure. This makes no substantive change in the interpretation. The bottom panel is magnetic field intensity (nT). Under the bottom panel, several tick marks are labeled with time (UTC), magnetic latitude (degrees), local time (fractional hours) and altitude (km).

We found it useful to organize the cusp passages in four specific categories which we will now discuss.

Figure 6.2 shows the Quiet cusp, characterized by a small spatial extent and Na^{+}-group ion flux co-located with that of the alpha particles and protons. The proton pitch angle distribution shows either isotropic or enhanced flux near 90°. While the energies of measured Na^{+}-group ions do vary for different Quiet cusps (0.8 keV – 13 keV), they are often in the 2-4 keV range. The depressions in the magnetic field magnitude from MAG that have corresponding enhancements in the FIPS measured proton flux are likely diamagnetic depressions. During this particular time period, FIPS FOV was pointed toward the planet, so that particles traveling away from the planet were measured. However, in many other Quiet cusp examples FIPS FOV was pointed away from the planet. Quiet cusps make up ~10% of the cusps surveyed.

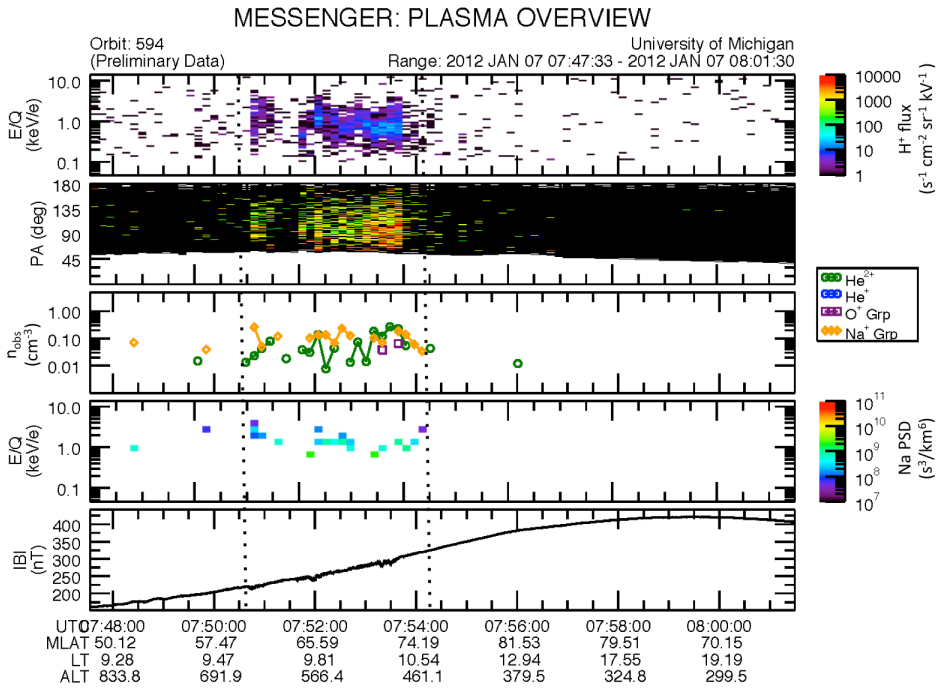

Figure 6.2. Quiet cusp. Shown from top to bottom are the following time series: proton energy spectrogram in units of flux (counts s^{-1} cm^{-2} sr^{-1} kV^{-1}); proton pitch angle distribution (arbitrary units); observed number density (cm^{-3}) alpha particles (He^{2+}, green), He^{+} (blue), O^{+} group (purple) and Na^{+} group (yellow); Na^{+}-group ion phase space density (s^3/km^6); magnetic field intensity (nT). Under the bottom panel, several tick marks are labeled with time (UTC), magnetic latitude (degrees), local time (fractional hours) and altitude (km).

Care is required to interpret the relatively narrow range of Na^{+}-group energies shown in Figure 6.2. Particle energies appear to cluster around ~ 1 keV, with no measured phase space density at energies below ~800 eV - misleadingly indicating a cold, fast flowing plasma. In FIPS, however, as with most plasma analyzers, the detection threshold decreases with increasing energy along with the volume of phase space measured, i.e., the one count limit is a lower phase space density at high energies that at low energies . This effect is shown in Figure 6.3. The one and two count limits (transformed into phase space density) are plotted along with the energy spectrum of the Na^{+}-group counts from the orbit 594 cusp in Figure 6.2. Given the very low counts (29) in this example, ions with energies below 1 keV are not typically detectable. Therefore, rather than indicating

a fast flowing plasma, this energy signature very likely indicates hot plasma at low density.

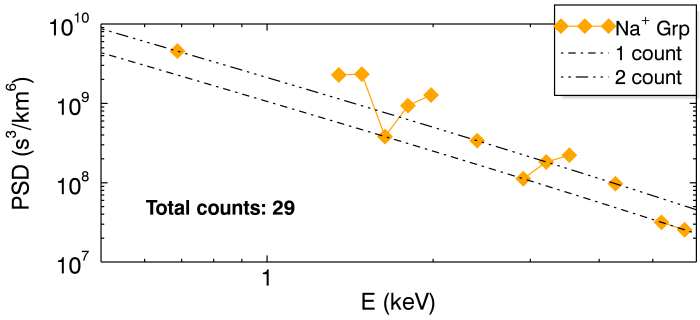

Figure 6.3. Phase space density versus energy for cusp passage on orbit 594.

A representative Weak cusp is shown in Figure 6.4. This cusp is characterized by spatially localized, low proton flux, as well as low Na^+ group observed densities (<0.1 cm^{-3}) measured at just a few time steps within the cusp. A number of even weaker cusps were surveyed, where Na^+ group and even alpha observed densities drop below the 10^{-3} cm^{-3} lower limit this study. Again, for most time steps within this cusp, the proton pitch angle distribution is spread over many angles and indicating a nearly isotropic and stagnant plasma. Diamagnetic depressions are still evident in the magnetic field, though fewer fluctuations are present. FIPS FOV was pointed away from the planet in this particular cusp observation, but there are a great many Weak cusp examples where FIPS was pointing directly at the planet, as in the Quiet cusp cases. In fact, FIPS pointing did not appear to be an important factor for most observations of the cusp proper. This FOV independence is consistent with our evaluation that the cusp plasma is very hot and nearly isotropic rather than convecting at high speeds with respect to the plasma thermal velocity. The Weak cusp category very broad, since the low flux conditions make

features difficult to identify. As such, this category makes up ~60% of the cusps examined.

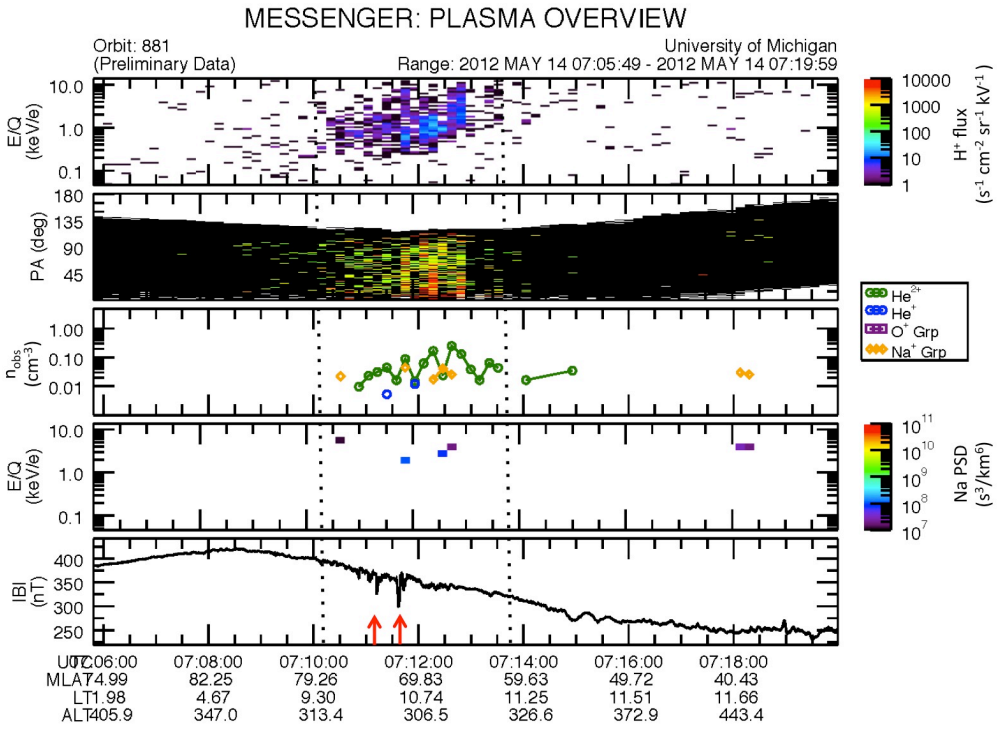

Figure 6.4. Weak cusp. Strong depressions (red arrows) not coincident with larger plasma flux periods (stripes in top panel). See Figure 6.2 caption and text for details.

An Active cusp is shown in Figure 6.5. As with the other cusp types, Na^+-group ions and alpha particles are co-located with increases in proton flux. However, high Na^+-group ion flux extends to lower latitudes (left side in this figure), independent of the protons. These lower latitude Na^+-group ions are very hot, with mean observed energies > 1-5 keV. The cusp proper, where the proton flux peaks (delimited by black dotted lines), contains slightly lower energy Na^+-group ions, down to a few hundred eV, indicating a denser and cooler population. In the proton flux spectrogram, an angled feature is evident starting around 21:22:00 UTC. This may be a velocity dispersion signature, which is a side effect of FTEs passing over the cusp [ref]. These signatures are

common for Active cusps. About 20% of the cusps surveyed fit cleanly into this category.

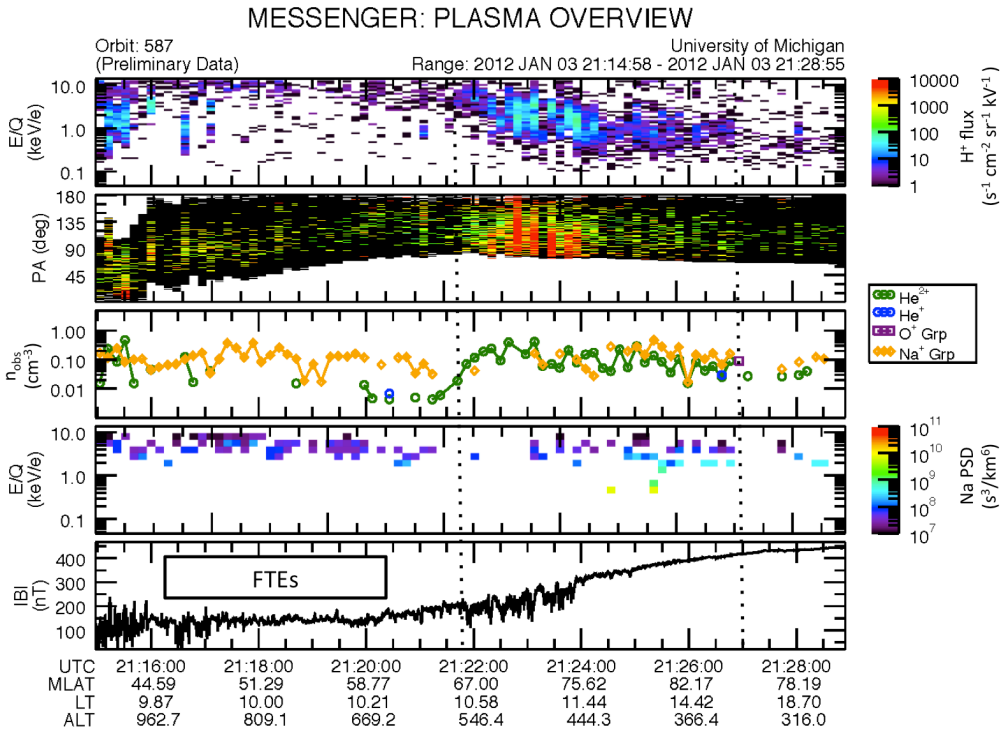

Figure 6.5. Active cusp. See Figure 6.2 caption and text for details.

In stark contrast to the weak cusp, the magnetic field in the active cusp is highly disturbed, showing not only stronger diamagnetic depressions, but also rapid, large-scale fluctuations, where the field intensity increases as well as decreases. Some of these transients are Flux Transfer Events (FTEs) that result from episodic reconnection [FTE ref]. Figure 6.4b shows the magnetic field in boundary normal coordinates [*DiBraccio et al.*, 2013]. {Waiting on this figure for more description.} The IMF orientation was highly variable just prior to passage into the magnetosheath.

In addition to many cusps which fit reasonably into the above three categories, there are variants of Quiet or Active cusps each with unusual and interesting features. These

are very special cases, which are either unique or occurring in less than 1% of the cusps surveyed.

The last cusp, shown in Figure 6.6, is less an example of a broad class than an example of a special case. Similar examples occurred in <1% of cusps surveyed. First, it is a particularly extreme example of an Active cusp. There is a large proton flux, with many bright (higher flux) stripes. There are large numbers of planetary ions, which are spread out beyond the cusp. There are very deep diamagnetic depressions in the field strength and compression peaks due to FTEs. However, this cusp shows another feature: a large population of very low energy Na^+-group ions just below the cusp in latitude. By definition of the cusp, latitudes below the cusp within the magnetopause should be in a dayside closed-field region. We examine this possibility that these low energy Na^+-group ions quasi-trapped in the dayside magnetic field using simple gyroradius calculations in the Discussion section below.

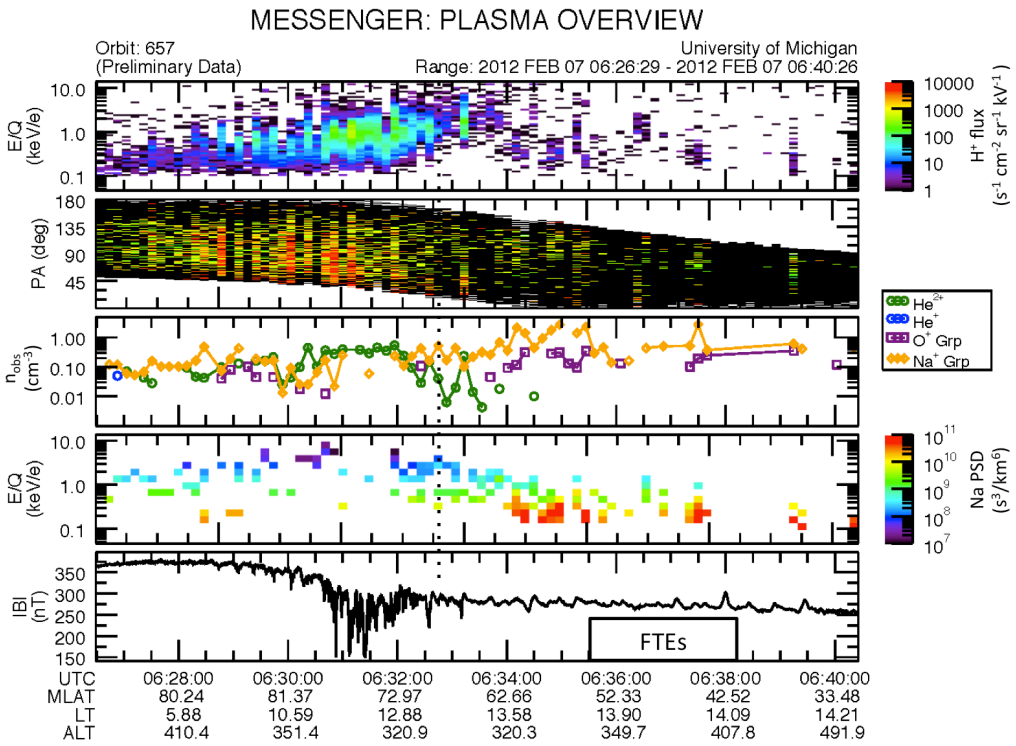

Figure 6.6. Active cusp with low-energy Na^+-group ions in dayside closed-field region. See Figure 6.2 caption and text for details.

6.3 Average Properties

We turn now to several summary plots to examine the collective properties of the cusp.

Figure 6.7 shows a color histogram of Na^+ group observed density versus local time (hours) and altitude (km). The plot was restricted to observations in the 50°-90° latitude range and local times from 9-15 hours. The total observed density in each cell was normalized by observation time. See Raines et al. [2013] for details. There is substantial structure in the observed density, but clearly the highest density region is centered around 11.5 hours local time and 900 km altitude. No clear trend of variation in observed energy with altitude or local time is evident (not shown).

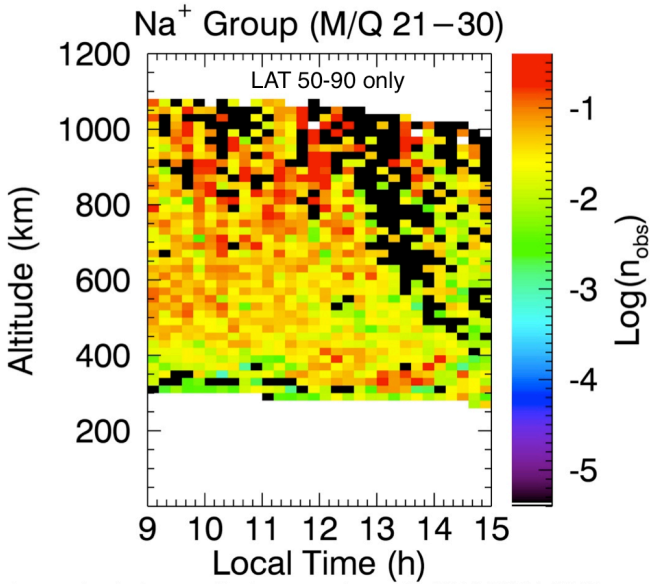

Figure 6.7. Local time and altitude dependence of observed Na^+ group density, co-added for cusp region.

In Figure 6.8, we collected together data from 24 Quiet cusps (Figures 6.8a-c) and 25 Active cusps, which were split into the cusp proper (Figures 6.9d-f) and lower latitude dayside region (Figures 6.8g-i). We then plotted the average kinetic properties of Na^+-group ions. The top panels show histograms of particle arrival direction centered on Mercury. The color is proportional to the number of counts in each arrival bin; white indicates directions that were not sampled. These are normalized for FIPS FOV sampling and projection effects. The average magnetic field direction is indicated by a dot with a circle around it, while the opposite to the field direction is indicated by a times symbol inside a circle. The black dashed line is the 90° pitch angle direction. The average magnetic field properties are intended as a rough guide only, since the orientations vary among the cusps included. The middle panels of Figure 6.8 give the pitch angle distribution for the collection. Finally, the bottom panel shows the accumulated phase space density (black dots) with error bars based only on counting statistics. The two dashed lines are the 1 count and 2 count thresholds to indicate the

actual measurement limit. Moments were taken of this summed data, using the method of Gershman et al. [2013], which assumes that the plasma is clearly subsonic. A Maxwellian distribution with these properties is plotted as a thin red line. The density and temperature values are included in the bottom left corner of these panels.

Looking first at the arrival directions in the top panels, we can see that the dawn hemisphere was well sampled, from North to South, in all three cases. Particles tended to arrive from all directions, again consistent with hot plasma of low Mach number. The arrival direction of the dayside region seems may be peaked a bit more (Figure 6.8h), but the number of counts available in that region were also higher. Each of the three pitch angle distributions (Figures 6.8b, 6.8e and 6.8g) are spread out fairly uniformly in energy, consistent with hot, isotropic plasmas. They are centered at a very small value of parallel energy, ~0.1 keV for singly charged ion, indicating little field-aligned convection. This distribution shows that most particle energy is fairly evenly distributed between the parallel and perpendicular directions, making the distribution nearly isotropic. The phase space density distribution of the Quiet and Active cusps are quite similar (Figures 6.8c and 6.8f), though the latter is a bit more broad. Likewise, their densities are very close, 0.52 cm^{-3} for the Quiet cusp and 0.41 cm^{-3} for the Active cusp. The recovered temperature shows the Active cusp to be substantially hotter, 14.0 MK, versus 10.7 MK for the Quiet. These figures indicate that the Quiet cusp plasma ions are consistent with a hot nearly isotropic Maxwellian distribution, with a broad distribution of arrival directions and energies.

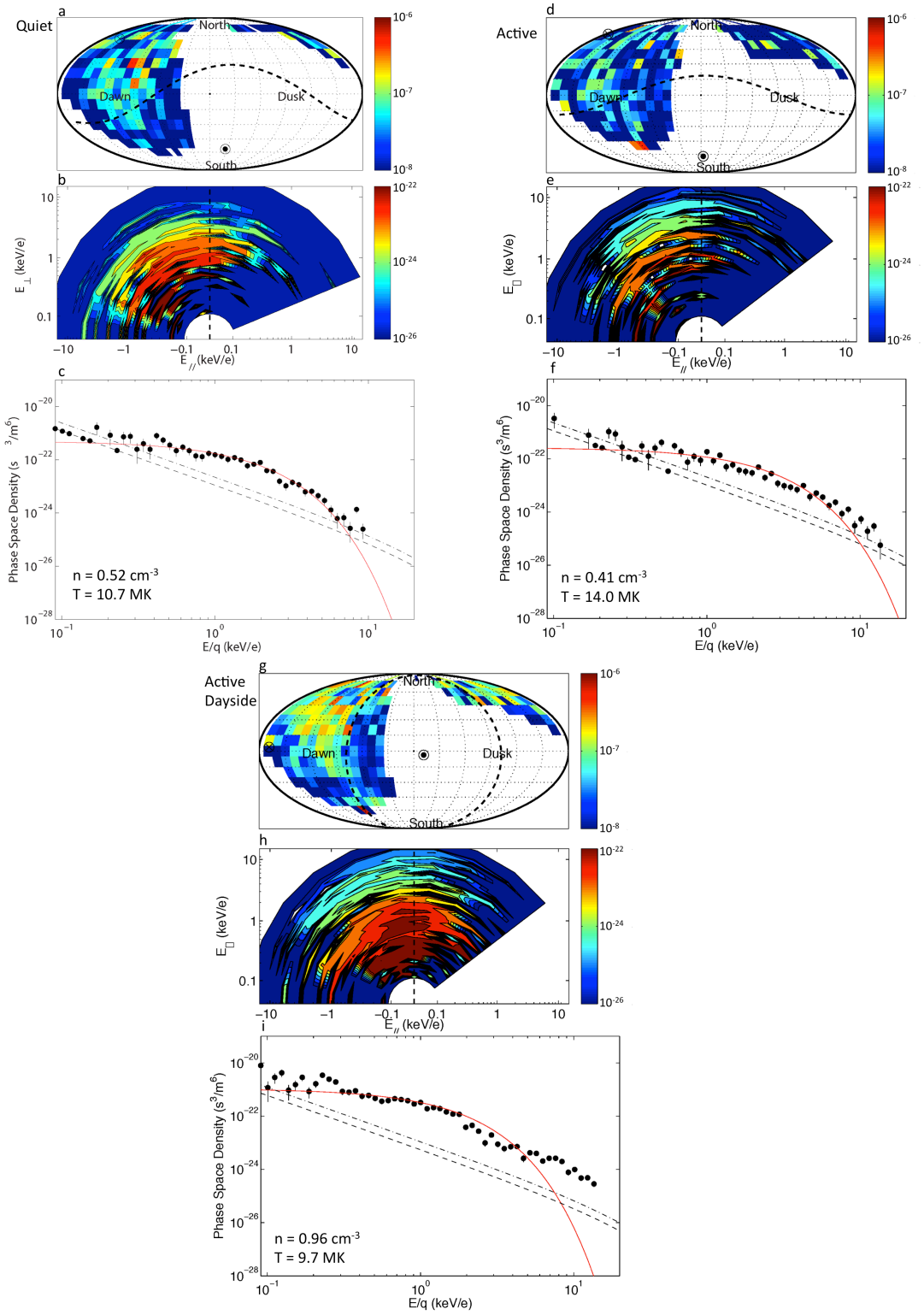

Figure 6.8. Average kinetic properties for Quiet and Active cusps. The average ambient Na^+-group ion density and temperature is given as well. See text for details.

6.4 Discussion

6.4.1 Sources of high energy (≥ 2 keV) Na^+-group ions

In the Introduction, we described two basic options for the origin of the observed Na^+-group ions: 1) Na^+-group ions are ejected by interaction of the solar wind with Mercury's surface at the cusp, via solar wind sputtering and ESD. 2) Neutral Na atoms are ionized upstream of the magnetopause, then swept back into the cusp by the plasma flow.

It is immediately clear that most of the ions observed by FIPS in the cusp are not simply ejected from the surface or photoionized. Ions observed in FIPS have significantly higher energies (>1 keV) than what is expected from sputtering (~ 1eV) [*Cassidy et al.*, 2005], or from ESD, which would result in Na+ energies < 10 eV [*McLain et al.* 2011]..

A cusp-localized acceleration mechanism known as the "cleft ion fountain" has been reported at Earth [*Horwitz,* 1984; *Horwitz et al.,* 1985; *Lockwood et al.,* 1985]. Horwitz et al. [1984] showed that ions released in the northern cusp with the right energy (0.3-0.5 eV) could follow a curved trajectory back into the magnetotail, staying within the magnetosphere. This acceleration is quite sensitive to the initial energy of the ions and the cross-polar cap electric field. Increasing the field and lowering the energy of the ions increased trapping. Horwitz et al., [1985] further showed particular examples where cusp ions could be energized by a factor of 10 in many cases due to a combination of E x B drift and magnetic field gradients along the field lines themselves. Delcourt et al. [2012] applied a very similar technique to Mercury, expanded into 3D and explicitly including the full equation of motion, to study centrifugal acceleration of ions traveling from the

cusp into the magnetotail. They show that largely due to the curvature of *E* x *B* drift paths, ions can be accelerate from energies of < 0.1 eV up to several hundred eV as they traverse the magnetospheric tail lobes. This is more pronounced at Mercury than at Earth, due to Mercury's large size in its magnetosphere and larger resulting magnetic field curvature.

However, this mechanism is very unlikely to account for the observed ions with keV energies within the cusp. First, ions in these works are only accelerated to hundreds of eV, still a factor of 10 smaller than most of the observed ion energies. Second, the acceleration takes place over a much larger path length than the size of the cusp. Acceleration achieved *within the cusp* by this mechanism should be a fraction of the total reported, falling even farther short of the observed energies. Second, acceleration in the cusp should produce ions that are streaming along field lines out of the cusp. Pitch angle distributions for Na^+-group ions in the cusp (Figure 6.8b and Figure 6.8e) do not show this. Instead, they show ions with very little field-aligned convection. Furthermore, the observed density of these ions peaks around 900 km, rather than peaking at the surface and falling off steadily with altitude as would be expected from a local source. Finally, for acceleration local to the cusp, we would expect a reverse velocity dispersion signature in the Na^+-group energies: Ion energy should increase with latitude. This mechanism accelerates ions anti-sunward, so ions measured at higher latitudes should have been accelerated more by the time they are measured than those measured at lower latitudes. This is not observed. It is possible that the rare occasions where very low energy (100-300 eV) Na^+-group ions are observed in the cusp, are periods where the convective electric field was particularly high. The cross polar cap potential may rise as high as 30

kV [*DiBraccio et al.,* 2013], which is much higher than Delcourt et al. [2012] used in their modeling. The resulting acceleration could have brought these ions into FIPS energy range and allowed them to be observed. So, while this mechanism may account for the very low energy ions observed, neither this nor any other acceleration mechanism, local to the cusp, is know which could accelerate cusp ions from < 10 eV to the observed >1 keV energies.

On the contrary, ions swept into the cusp would have very different properties. If they were swept in from the solar wind, they would first have to be picked up, resulting in speeds between 0-2 solar wind speeds, as observed near Mercury. When the solar wind is diverted around the magnetosphere slows down, to nearly stagnant at the subsolar point and back to nearly its original speed by 90° from the subsolar. Assuming a nominal 440 km/s solar wind speed, the flow speed in the magnetosheath at ~9 hrs local time should be ~160 km/s. For a Na^+ ion, this corresponds to energies of 3-12 keV, consistent with observations. This bulk speed could be converted to thermal speed by the increasing magnetic field in the cusp, as the plasma particles feel an increasing magnetic mirror force which converts their parallel energy to perpendicular energy. As was discussed above, the average pitch angle distribution in the Quiet cusp shows substantial perpendicular energy. Furthermore, the cusp is a dynamic environment, filled with magnetic irregularities that will serve to drive particle distribution functions toward the equilibrium Maxwellian distributions, consistent with the isotropic distribution observed. Alternatively, if ions are swept into the cusp by reconnection, they could have energies up to the local Alfvén speed. For an average solar wind density of 50 cm^{-3} at 0.3 AU, the density at the subsolar stagnation point could be up to 200 cm^{-3}. Assuming magnetic

field of 133 nT the subsolar point [*DiBraccio et al.,* 2013], this equates to 265 km/s. This speed corresponds to an energy of 8.4 keV for a Na^+, and is the same range as ions observed. Energy arguments alone to not allow us to distinguish between solar wing pickup and acceleration by reconnection.

The observed pitch angle distributions of ions on the dayside (Figure 6.8h) do show an interesting feature: They do not appear to be flowing along dayside field lines, as one might expect from a reconnection jet. It is possible that these ions are observed deep enough into the magnetic mirror of Mercury's North pole that much of their parallel energy has already been converted to perpendicular energy. We must keep in mind that MESSENGER has not likely directly sampled the reconnection site in these examples, so it is difficult to assess this scenario. Another, very interesting scenario could involve non-adiabatic behavior, which may be quite important for Mercury heavy ions [*Delcourt et al.*, 2003; *Delcourt et al.*, 2012; *Raines et al.*, 2013]. In particular, the large gyroradius of the Na^+-group ions may cause them to respond differently to the reconnection electric field, since the scale of the reconnection region is based mostly on the proton gyroradius. Investigating this option would require an additional modeling component and is beyond the scope of this work.

Given the consistency of the observations, we must conclude that the Na^+-group ions observed by FIPS have been transported from elsewhere, rather than generated in the cusp by surface processes. The correlation of the highest observed Na^+-group energies with FTEs is indicative of reconnection playing an important role. Therefore, we believe that ions being swept in by dayside reconnection is more consistent with our observations. Some evidence of this process may be evident in Figure 6.5: A steady

stream of alphas and planetary ions appears to be entering the dayside magnetosphere from magnetosheath.

6.4.2 Sources of low energy (≤ 300 eV) Na^+-group ions

Although lower energy (100-300 eV) Na^+-group ions are certainly in the minority, they are observed a number of cusp crossings, typically at latitudes lower than the cusp on the dayside.

Exospheric neutrals have been observed with a wide range of temperatures by the MESSENGER UltraViolet and Visible Spectrometer (UVVS) [*McClintock et al.* 2007], from 5000 K for Na to 20,000 K for Mg, to up to 50,000 K for Ca [*Vervack et al.*, 2010; *Burger et al.*, 2012]. These correspond to Na energies of ~0.22 eV or up to ~ 2 eV for 3σ from the mean. As we discussed above, the upper energy limit for neutrals released from the surface is 100,000 K (10 eV), from ESD [*McLean et al,* 2011]. Neutrals that are photoionized in the dayside magnetosphere may become trapped on closed dayside field lines at basically their same energy, since photoionization will not significantly change the kinetic energy of the particle. To escape Mercury's gravity, an atom must have a speed of 4.3 km/s [Hunten et al., 1988], which is 2.2 eV for a Na^+ ion. (For an ion, this assumes escape along a magnetic field line, which requires no extra energy.) These ion energies are too low (by a factor of 10) to account for ions observed in the 100-300 eV energy range.

Another possible source for the observed 100-300 eV ions may be circulation in from the magnetotail. It has been shown that Na^+ ions released from the cusp are accelerated by the centrifugal force created by the curvature of their E x B drift paths [*Delcourt et al,* 2003; *Sarantos et al.,* 2009; *Delcourt et al.*, 2012]. Furthermore, we have observed ions

with keV energies in the tail with FIPS [*Zurbuchen et al.*, 2011]. It is well know at the Earth that plasma flows back toward the planet and around equatorial region to the dayside as a result of Dungey cycle convection [*Dungey*, 1961]. Evidence of this flow pattern at Mercury has been observed as dipolarization [*Sundberg et al.*, 2012], which result from planet-ward plasma flow in the magnetotail. However, in order for planetary ions to make it back around to the dayside, their gyroradii must fit inside the dayside magnetosphere. As their gyroradius increases, the channel through which they can pass without gyrating into the planet or across the magnetopause (and being lost) narrows. Winslow et al. [2012] found that a mean magnetopause stand-off distance of 1.4 R_M (980 km altitude). The dayside portion of the magnetopause is approximately spherical [*Shue et al.* 1997; *Slavin et al*. 2010], so this measurement sets the approximate size of the dayside magnetosphere. We used the Alexeev magnetic field model [*Alexeev et al.,* 2008] to calculate typical ion gyroradii over a range of energies, from 100 eV to 8 keV, at center of the dayside magnetosphere 1.2 R_M (490 km altitude). We assumed that all of the measured energy was in the perpendicular direction, yielding the largest equatorial gyroradius and thus a bounding case. The results are shown in Table 6.1. These simple calculations show that ions in of these energies could fit through the equatorial dayside magnetosphere. It is also apparent that lower energy ions have much more clearance in the dayside magnetosphere, which in turn allows a greater range of trajectories to pass through. Transport through this region may act like an energy filter, preferentially allowing more low energy ions (100-300 eV) to pass than high energy ions (1-10 keV). Of course, the solar wind conditions would also play a role. When the solar wind dynamic pressure increases, due to increases in solar wind density, velocity or both, the

magnetopause will move closer to the planet and reduce the size of the dayside magnetosphere space. Likewise, dynamic pressure decreases will increase the size of the space.

Location (MSO)		Energy	Field	Gyroradius		Clearance	
X (R_M)	Y (R_M)	E (keV)	B (nT)	(km)	(R_M)	MP	surface
1.20	0.00	0.2	177	55	0.023	0.207	0.177
1.20	0.00	2	177	175	0.072	0.158	0.128
1.20	0.00	4	177	247	0.101	0.129	0.099
1.20	0.00	8	177	350	0.143	0.087	0.057
0.00	1.20	0.2	130	75	0.031	0.199	0.169
0.00	1.20	2	130	238	0.098	0.132	0.102
0.00	1.20	4	130	337	0.138	0.092	0.062
0.00	1.20	8	130	476	0.195	0.035	0.005

Table 6.1. Sample Na^+ gyroradii calculated from modeled magnetic field at locations specified in equatorial dayside magnetosphere. Clearance to magnetopause (MP) and surface is color coded in a linear scale, from 0.005 – 0.207 R_M. See text for details.

6.5 Conclusions

We reviewed MESSENGER cusp crossings for over 518 orbits from September 2011 through May 2012. We found that Na^+-group ions are routinely observed in the cusp region with energies in the 0.8-4 keV range and observed densities of 0.01-2 cm^{-3}, with energies observed up to 13 keV (FIPS maximum). There is substantial variability in the cusp for all species. We found that the highest densities and energies (5-10 keV) of Na^+-group ions correlate with magnitude of diamagnetic decrease and level of FTE activity. The high energies (2-4 keV) of Na^+ group ions regularly observed in the cusp along with the nearly isotropic pitch angle distributions strongly favor ionization in the magnetosheath (and beyond) then sweeping into the cusp by reconnection. Low energy (100-300 eV) Na^+ ions are occasionally present at lower dayside latitudes than the cusp.

These ions may be brought into the dayside magnetosphere through Dungey circulation from the magnetotail or by ion drift.

Chapter 7

Conclusions

7.1 Science Questions Revisited

We return now to the guiding science questions of this work to assess the progress made toward finding their answers.

1. Are the spatial distributions and kinetic properties of plasma ions consistent with a Mercury magnetosphere that is morphologically similar to that of Earth?

Bulk plasma ion measurements confirm that Mercury's magnetosphere is morphologically similar to Earth: There is heated and compressed solar wind plasma (protons and alpha particles) in the magnetosheath regions, between the bow shock and magnetopause. Magnetospheric plasmas are concentrated at the cusps and around the nightside magnetic equator in the central plasma sheet, with very little plasma content observed in the tail lobes. The bulk plasma parameters of these populations (density, plasma beta, and pressure) are consistent with expectations based on observations at Earth.

2. What is the nature of the coupling in the surface-exosphere-magnetosphere system?

We have found significant evidence of the influence of the exosphere on the magnetosphere. Planetary ions are found in Mercury's magnetosphere on every orbit, clearly identifying the exosphere as a source of magnetospheric heavy ions. These ions are not limited to within the magnetosphere and are also observed in the magnetosheath and upstream solar wind. Planetary ions show density enhancements corresponding to their parent neutral populations, particularly in the cusp and near the dawn equator. However, heavy planetary ion density is also enhanced near the nightside magnetic equator, in particular on the pre-midnight side, which is not true of the exospheric neutrals. He^+ are distributed much more uniformly than other planetary ions, which may result from substantially different source regions or processes. Planetary ions have much larger *e*-folding heights than their parent neutral populations across the dayside, indicating significant influence from magnetospheric electric and magnetic fields prior to their measurement by FIPS. The behavior of planetary ions appears to be only partially determined by their parent neutral populations.

We do not yet have conclusive evidence of a direct surface-magnetosphere coupling, though 100-300 eV Na^+-group ions measured in the northern magnetospheric cusp are compelling evidence of a possible link. The direct effects of the magnetospheric processes on the surface and exosphere have not yet been observed.

3. What role do planetary ions play in Mercury's magnetosphere?

This work has shed light on the dynamics of planetary ions in Mercury's magnetosphere, which is the first step in understanding their role in the overall system. First, the asymmetric distribution of large-gyroradius Na^+ ions preferentially in the pre-midnight central plasma sheet suggests that these ions undergo non-adiabatic motion in Mercury's magnetosphere. These demagnetized ions would respond very differently to magnetospheric electric fields, which could have wide-reaching implications in the surface-exosphere-magnetosphere system. In particular, non-adiabatic motion could alter locations and energies of planetary ions precipitating onto the surface, and the resultant creation of new ions and neutrals from surface constituents. Second, we found that Na^+-group ions can at times provide up to 25% of total plasma ion pressure in the central plasma sheet. At these times, these demagnetized Na^+-group ions could increase tail reconnection rates and alter wave growth rates, thus sharing the role of determining magnetospheric dynamics with ions of solar wind origin. Finally, we have shown Na^+-group ions observed in Mercury's northern cusp are swept in to the cusp rather flowing out of the cusp, as at Earth. Often correlated with dayside reconnection, this unusual behavior serves to energize planetary ions in Mercury's active magnetosphere.

7.2 Next Steps

In this work, we have presented many discoveries from these first ever plasma measurements at Mercury. While these results represent at substantial step forward in our understanding of Mercury's magnetosphere, there is plenty of investigation remaining..

We have shown that Mercury's magnetosphere is highly variable and dynamic, probably due its close coupling to the solar wind, exosphere and possibly even the planet.

While some of these connections have been inferred, we have not yet quantitatively tied features observed in the plasma ions with those observed in the exosphere or on the surface. There are many challenges to doing this, most of them related to the nature of point measurements of *in situ* instruments and line-of-sight or distant measurements of remote sensing spectrometers. Global modeling could be the key to making these connections. Global exospheric models are already being constructed which can be fit to UVVS exospheric measurements from a specific time period. These can provide a modeled exosphere that is self-consistent with measurements, specific to a relatively short window in time. If sufficiently realistic ionization models and fields can be incorporated into these models, they could be used to infer the global behavior ions in Mercury's space environment from FIPS single point measurements as well as add much-needed constraints to exosphere models.

On a smaller size scale, strong evidence for non-adiabatic behavior of Na^+-group ions indicates that there is much to learn about magnetospheric physics from Mercury. Particle tracing, hybrid and fully kinetic models can help, with their ability to follow individual planetary ion trajectories through the system using full equations of motion. However, to really push the boundaries of our knowledge, we must extract more and more detailed information from the data. Only the data is guaranteed to include all the physics, even the parts that we do not yet realize are important. We must continue to find new analysis methods that push the boundaries of the rich FIPS data set so that we can increasingly examine very localized, complex plasma ion behavior in many different situations throughout Mercury's space environment.

Appendix 1

FIPS FOV Model

This appendix describes the motivation, design considerations, implementation and testing of the FIPS field of view (FOV) model. This subject is treated very briefly in the appendix of Chapter 2.

A1.1 Motivation

Soon after the first MESSENGER flyby of Mercury on January 14, 2008, it became clear that interpreting FIPS data required the use of a software instrument model of FIPS, including field of view (FOV). Figure A1.1 shows the raw data collected by FIPS and MAG during this flyby. The region between the green (left) and purple (right) dotted lines is the inbound magnetosheath. The spacecraft is slewing back and forth by ~60° to scan the exosphere for UVVS, as evident in the orientation of FIPS boresight vector latitude in Mercury coordinates (panel 6 from top). (The FIPS boresight vector is centered in FIPS FOV.) Notice that there is a clear correlation between FIPS count rate (panel 2 from top) and these orientation changes. Each time that the boresight latitude approaches 0°, the FIPS counts go through a local maximum. Once within the magnetosphere (between dotted purple lines), this correlation stops. FIPS count rates were clearly correlated with some of these rotations and not with others, a fact that was a bit disconcerting at the time.

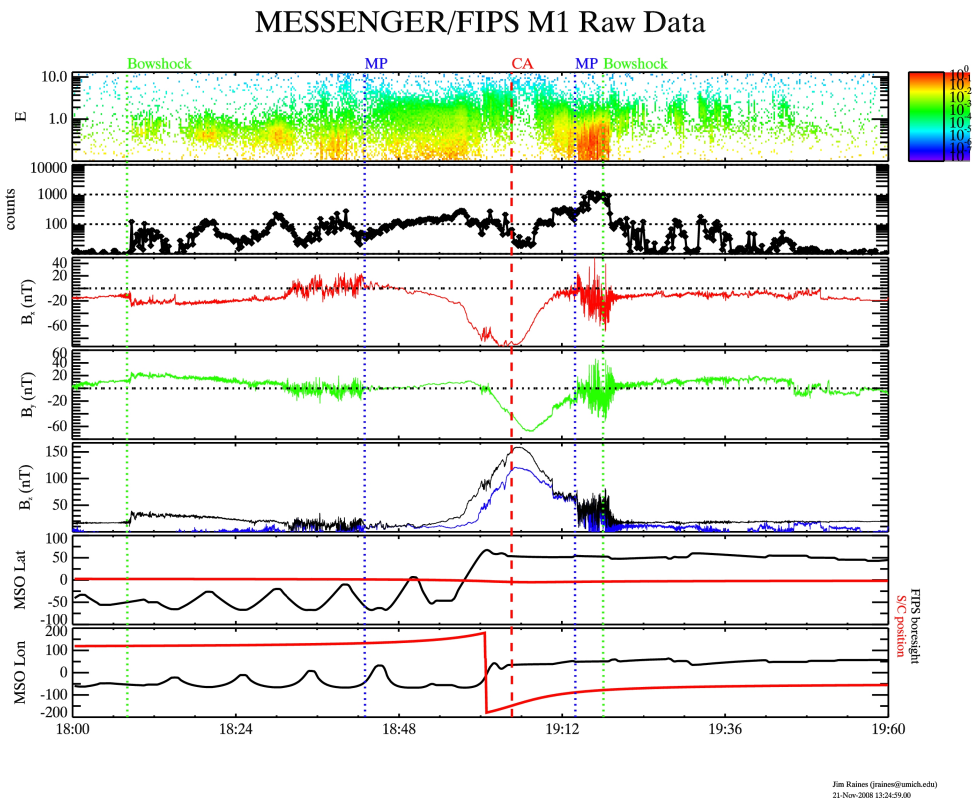

Figure A1.1. Raw data from M1 flyby. FIPS energy spectrogram (arbitrary units) and total counts are show in panels 1 and 2 (numbered from top). Magnetic field components B_X (red), B_Y (green), and B_Z (blue) as well as magnetic field magnitude (black) are shown in panels 3-5. The orientation of FIPS boresight vector (black) is shown in Mercury-centered latitude (panel 6) and longitude (panel 7), as well as MESSENGER position (red).

The second clear indicator of need for a software FOV model came when we performed some of our typical on the M1 data: moment calculations. For supersonic plasma distributions, like the solar wind, the bulk speed can easily be calculated as the first moment of the phase space distribution function. For a Maxwellian distribution, this is essentially just finding the velocity of the peak phase space density. The phase space densities from the M1 observations within the magnetosphere were clearly peaked, so bulk velocities were calculated, reaching speeds of up to 1000 km/s. These values were the first indication of a problem: Analysis of the magnetometer data did not show evidence of that sort of extreme magnetospheric convection, not to mention the difficulty

in explaining the generation of speeds surely exceeding the local Alfvén speed by reconnection in the magnetotail.

A1.2 The Model

The main requirements of the model are conceptually simple: Determine FIPS counts as a function of *E/q* and incident angle (zenith and azimuth) from an input distribution function in a suitable reference frame and output the resulting count histograms.

A1.2.1 Reference frames

There are four reference frames that are important to the FOV model:

1) The Mercury Solar Orbital (MSO) frame, centered on Mercury. In this frame X_{MSO} points from Mercury toward the Sun. The Z_{MSO} axis is co-axial with Mercury's spin axis and Y_{MSO} completes the right-handed system.
2) Radial Tangential Normal (RTN), a Cartesian frame centered on the Sun. In this frame, R points from the Sun to Mercury, rotating around the Sun with the planet. $T = \Omega \times R$, where Ω is the spin axis of the Sun. This causes T to point in the direction of Mercury's motion around the Sun. N completes the right-handed system.
3) The FIPS instrument frame, defined in a spherical coordinate system centered at the FIPS aperture, with the polar axis co-axial with the boresight vector through the middle of the FOV..
4) FIPS MCP frame, centered on FIPS start micro-channel plate. This is actually a 2D frame overlaid on the start MCP which corresponds to the Cartesian position on the MCP. The mapping between this frame and the (spherical) FIPS instrument frame was determined by fitting calibration data.

Each of the first two is a suitable frame in which to define an input distribution. The third is the frame in which the measurements take place. This spherical system is essentially 3D velocity space measured at the position of an infinitesimally small FIPS aperture. The fourth frame is where the data is actually taken.

Time-dependent rotation matrices must be used to transform between frames, because all frames moving relative to one another. To conveniently accomplish this, the model gets rotation matrices from the Spacecraft, Planet, Instrument, C-matrix, Pointing and Events (SPICE) software package [*Acton et al.*, 1996]. All of the above reference frames can be loaded into spice in the form of kernel files, as well as a MESSENGER trajectory file and day-specific attitude C-kernels. SPICE can also be used to find velocity of MESSENGER relative to Mercury or the Sun, which is used to correct for spacecraft velocity.

The use of SPICE had another advantage. Part of the FIPS FOV is obstructed by the MESSENGER spacecraft body and sunshade. These obstructions were mapped out using the MESSENGER CAD model and vectors for each of the corners written into a SPICE kernel. These vectors were then used to map out the cumulative blocked area within FIPS FOV and remove it from consideration by the model. This last feature can be disabled to allow for hypothesis testing on the effects of FOV blockage.

A1.2.2 Input distribution

In principle, the model can use any distribution that can be coded as a function returning counts for a given 3D velocity. In practice, the most commonly used input distribution is a bi-Maxwellian, where the following parameters are specified: bulk speed, temperature and direction. Direction can be specified in any of the three frames

described above. For science, either HCI or MSO is typically used, since those physical understanding of the plasma flows are relative to the Sun or Mercury. The FIPS spherical frame is also used, whenever there is a need to place the plasma flow very specifically in FIPS FOV. This is also useful for hypothesis testing to avoid the need to find periods with specific sequences of MESSENGER orientations, such as modeling the effect of plasma flow direction moving in and out of the FOV.

A1.2.3 Sampling phase space

Besides proper reference frames, the most fundamental requirement for the model was proper sampling of the distribution in phase space, $f(v_i, \theta, \phi)$, to produces counts (N_i) at E/q step i (v_i) over time Δt:

$$N_i = \frac{1}{\pi} f(v_i, \theta, \varphi)\, \Delta t\, \eta_i\, g\, \Delta\theta\, \Delta\varphi\, \sin\theta\, {v_i}^4. \qquad \text{(A1.1)}$$

Eq. (A.1.1) includes dependence on observed solid angle, $\Delta\theta\, \Delta\phi\, sin\theta$, and two instrument parameters, the effective geometric factor (g) and the efficiency at step i (η_i). Units are $s^3km^{-3}cm^{-3}$ for f, km s^{-1} for v_i, and s for Δt. All angles are in radians. This relation effectively weights counts at higher velocities more than those at lower velocities, in the same way that the instrument does in the process of measurement.

While it was clear how to transform between reference frames, it was less clear *when* to apply the transformations. For example, if modeling the solar wind defined in heliospheric frame, should that distribution be transformed into the instrument frame and then sampled? Or, should the FIPS FOV and energy sampling be transformed into the heliospheric frame then be compared against the input distribution? The problem with transforming everything into one frame is that things that are clear in their native frame, can often get quite confusing in another frame, especially if the rotations are time

dependent. FIPS instrument frame would trace out a complex shape in the heliospheric frame as MESSENGER attitude is continually adjusted to allow measurements by one instrument after another during an orbit. We decided to eliminate this problem by taking a hybrid approach, which keeps everything in its native frame. To find the phase space density at a particular location in FIPS FOV, the coordinate vector is rotated into the frame of the distribution. The phase space density at that point in the frame of the distribution is taken as the phase space density for the coordinate vector in FIPS FOV. Liouville's Theorem guarantees that phase space density does not depend on reference frame.

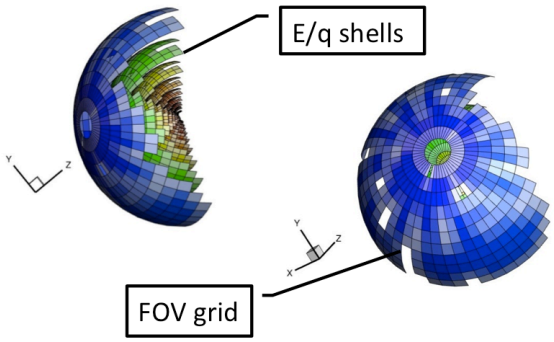

Figure A1.2. A graphical representation of FIPS FOV shown as spherical shell grids at several different radii. The grids represent the angle component, while each shell represents a different *E/q* value. The whitespace "bite" out of the right shell represents the portion of FIPS FOV which is blocked by the spacecraft. (Note: Individual white cells are an unintended feature in this figure and should be ignored.)

To make simulated measurements, the model must step through the FOV and add up counts from modeled distribution. For each *E/q* value, the model loops over bins in (θ, φ) (Figure A1.2), doing the following at each one:

1) The center (*E/q*, θ, φ) of the bin is converted to the frame of the distribution (RTN or MSO).

2) The phase space density at this point in RTN or MSO is calculated from the distribution function.

3) This phase space density is assigned to the (E/q, θ, φ) bin, added to the current value.

4) Counts are calculated from phase space density according to Equation 1.

After looping over all coordinates, the model outputs the synthetic data in the same histograms that are used during real data analysis: energy spectra, arrival direction histograms and 3D velocity distribution functions.

Sampling normalization in the model was tested using a flat field distribution as an input. This distribution returned the same phase space density (1) for all (E/q, θ, φ). Since the input distribution had the same value everywhere, any non-uniformity in the energy spectra or arrival histograms was used to identify problems with the sampling normalization, both in angle and in phase space.

A1.2.4 Switchable realism

As software, the FOV model performs ideally, whereas the real FIPS does not. In particular, two aspects of real instrument behavior have significant bearing on comparisons between instrument and model data: detection efficiencies and position spreading. Due to the internal workings of the FIPS, there is a probability (<1) of detection for any given particle which primarily depends on the mass and energy of the particle. For a given mass particle, the counts registered versus E/q are essentially a convolution of real flux and the detection efficiency at point. These efficiencies were measured in ground calibration, using known beam fluxes as input. There is also

spreading in the positions registered on the start MCP. Peak shapes in MCP coordinates were determined in ground calibration and fit to Gaussian functions.

Since these effects are not negligible, they are included in the model. This facilitates comparison with actual data and allows the user to focus on the effects of interest. These can be optionally switched off, which is especially useful in qualitative assessment of the limits of instrument measurements.

A1.3 Using the Model

The following example illustrates the effect in FIPS measurements of a distribution that becomes progressively hotter, with a correspondingly shrinking Mach number ($M=V/V_{th}$). Figure A1.3 shows three runs of the FIPS FOV model with a constant bulk velocity (V) stays and increasing thermal velocity (V_{th}). In the top row, the highly supersonic distribution (M=8.2) is narrowly focused both in E/q and in arrival direction, with E_{peak} at 0.9 keV/e, the expected value for a Maxwellian distribution with V=410 km/s. However, as Vth increases to 150 km/s, E_{peak} has shifted to 1.5 keV/e. By the time M=0.9 with V_{th}=450 km/s, E_{peak} has risen to ~5.8 keV. This reflects that fact that as M decreases, Vth becomes difficult to distinguish from V. Interpreting measurements of subsonic distributions (M<1) is quite different from highly supersonic distributions (M>5). Subsonic distributions are peaked, but the peak is not at the bulk convection speed, this is essentially due to the difficulty of separating bulk convection speed from thermal speed in energy spectra alone.

This example illustrates another fundamental point: the counts become very uniformly distributed with arrival direction once the distribution approaches M=1. Under these conditions, counts measured by FIPS do not depend strongly on its orientation.

This was evident in real data withing the magnosphere during M1 (Figure A1.1). We used this fact as the basis for the density & temperature recovery method, employed in previous chapters.

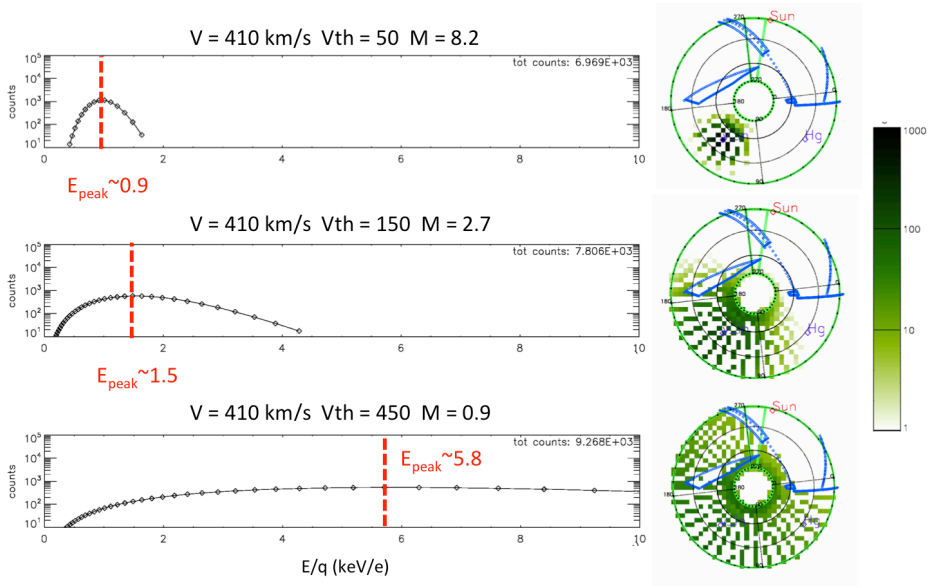

Figure A1.3. Sample model output for several bulk speed (V) and thermal speed (Vth) combinations. Mach number ($M=V/V_{th}$). Circular plots at right are arrival direction histograms in FIPS instrument frame, showing the FOV as if looking out of the instrument. Distance from the center is zenith angle, with rings every 20° in the 15°-75° FOV. Angular separation from the radial line on the right is azimuth angle (clockwise). Azimuth angle Superimposed on this view are spacecraft obstructions (blue lines), as well as the position of Mercury (Hg, in purple) and the Sun (red). Spaces between the cells are due to running with suboptimal angular steps to speed up the computation.

In order to explore the ability to similarly use the model to recover bulk and thermal speed in a subsonic distribution, we conducted a parameter study. We ran all combinations of a range of (V,V_{th}) pairs (the test set), then compared them to an *E/q* spectra from a known input (V,V_{th}), to see if the input (V,V_{th}) could be recovered. Figure A1.4 shows one such example. A test set of model *E/q* spectra were generated for all combinations of (V,V_{th}) shown, increments chosen so that *exact* input (V,V_{th}) pair was not in test set. The average error between each of test set spectra and the spectrum

generated from the input was calculated. The test set (V,V_{th}) pair which gave the minimum error when compared to the input was selected as the *recovered* pair. In this case, the input pair was (V=125.8 km/s, V_{th}=265.0 km/s). The recovered pair was found to be (V=71.4 km/s, V_{th}=270.0 km/s). The V_{th} matched exactly (within the 10 km/s step size) but V was estimated quite low.

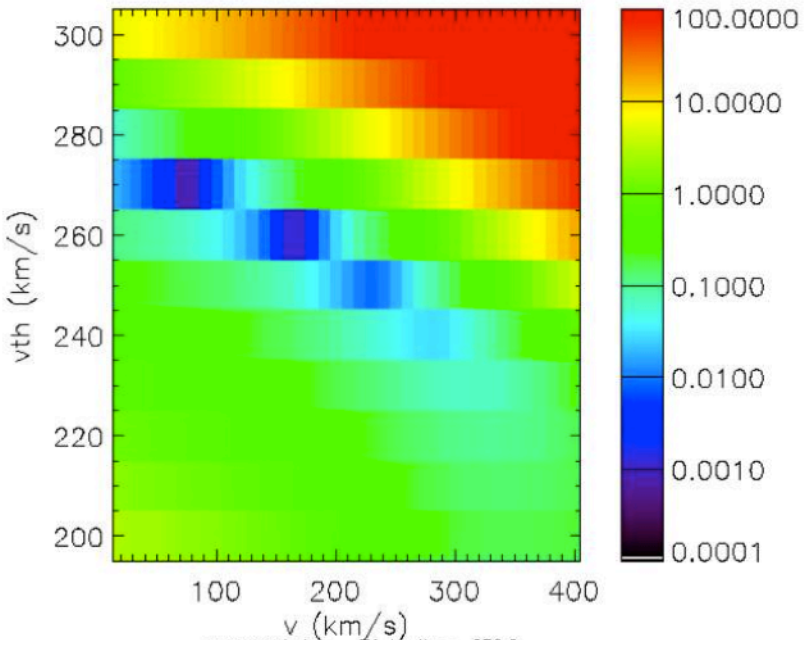

Figure A1.4. Relative error for model spectra test set (indicated (V,V_{th}) combinations) when compared to known input, (V=125.8 km/s, V_{th}=265.0 km/s). Recovered values were (V=71.4 km/s, V_{th}=270.0 km/s) [*Tracy,* 2010].

This test was run over a subset of the expected magnetospheric parameter space, so the results should be representative of recovery from Mercury magnetosphere data. Given the unknowns in that system, recovery even with these errors may be useful. Furthermore, it may be possible to improve the results by fitting arrival histograms as well as E/q spectra.

A1.4 Conclusions

Experience has shown that this model is an invaluable tool for understanding the measurements of the FIPS instrument and interpreting them in their physical context. It has also been an important tool for initial validation of instrument correction functions and data processing code at all levels, where it provides the powerful ability for validating behavior from known, realistic inputs.

Appendix 2

Observed Density from Counts

This appendix describes the calculation of observed density (zeroth order moment) from FIPS counts. Observed density is simply density calculated from the counts registered by FIPS, without any corrections for the portion of phase space not sampled by the instrument. It is used when the assumptions required for calculation of the true, ambient plasma density do not hold. The use of observed density is described in Chapter 5.

A2.1 Transformation to Phase Space Density

Counts (N_i) accumulated for time Δt at each E/q step i (v_i) are transformed to phase space density, $f(v_i, \theta, \phi)$, using an inverted form of the equation give in Appendix 1:

$$f(v_i, \theta, \varphi) = 2N_i \,/\, (\Delta t\, \eta_i\, g\, \Delta\theta\, \Delta\varphi \sin\theta\, {v_i}^4). \qquad \text{(A2.1)}$$

$$v_i = 439 \sqrt{\left(\frac{E}{q}\right)_i / \left(\frac{m}{q}\right)}. \qquad \text{(A2.2)}$$

Eq. (A2.1) includes dependence on observed solid angle, $\Delta\theta\, \Delta\phi\, sin\theta$, and two instrument parameters, the effective geometric factor (g) and the efficiency at step i (η_i). Units are $s^3km^{-3}cm^{-3}$ for f, km s^{-1} for v_i, and s for Δt. All angles are in radians. This relation effectively weights counts at higher velocities more than those at lower velocities, in the same way that the instrument does in the process of measurement. For this work, g was

set to 1.43 x 10^{-5} cm^2 sr (eV/eV). The accumulation time for counts collected in Survey mode was 0.95 s and 0.05 s for Burst mode. Equation A2.2 gives the velocity (v_i) for an ion of mass (m) and charge (q) measured at E/q step i. Units for m and q are amu and elementary charge (e), respectively.

A2.2 Calculation of Observed Density

From phase space density, $f(v_i, \theta, \phi)$, calculation of n_{obs} is accomplished via a simple discrete integral, where δv is the variable of integration (in km s^{-1}):

$$\delta v_i = |v_i - v_{i+i}|. \quad \text{(A2.3)}$$

$$n_{obs} = 10^{-15} \sum_i f(v_i, \theta, \phi) v_i^2 \delta v_i \quad \text{(A2.4)}$$

where the constant converts n_{obs} from km^{-3} to cm^{-3}.

A2.3 Validation of Observed Density

This procedure was validated by calculating the n_{obs} value for the first FIPS solar wind observation near 1 AU, on 15 April 2005. During this observation, MESSENGER was rotated so that the solar wind beam was entirely within FIPS FOV. In this case, n_{obs} is equivalent to the ambient density which was derived from measurements from the ACE spacecraft, as described in the appendix of Chapter 3.

References

Acton, C.H. (1996), Ancillary data services of NASA's Navigation and Ancillary Information Facility, *Planet. Space Sci.*, *44*, 65–70.

Alexeev, I. I., E. S. Belenkaya, S. Y. Bobrovnikov, J. A. Slavin, and M. Sarantos (2008), Paraboloid model of Mercury's magnetosphere, *J Geophys Res-Space*, *113*(A12).

Anderson, B. J., M. H. Acuna, D. A. Lohr, J. Scheifele, A. Raval, H. Korth, and J. A. Slavin (2007), The Magnetometer instrument on MESSENGER, *Space Sci. Rev.*, *131*(1-4), 417-450.

Anderson, B.J., M.H. Acuña, H. Korth, M.E. Purucker, C. L. Johnson, J.A. Slavin, S.C. Solomon, R.L. McNutt Jr., (2008), The structure of Mercury's magnetic field from MESSENGER's first flyby. *Science*, *321*, 82–85.

Anderson, B.J., Acuña, M.H., Korth, H., Slavin, J.A., Uno, H., Johnson, C.L., Purucker, M.E., Solomon, S.C., Raines, J.M., Zurbuchen, T.H., Gloeckler, G., McNutt Jr., R.L., (2010) The magnetic field of Mercury. *Space Sci. Rev.*, *152*, 307–339.

Anderson, B. J., C. L. Johnson, H. Korth, M. E. Purucker, R. M. Winslow, J. A. Slavin, S. C. Solomon, R. L. McNutt Jr., J. M. Raines, and T. H. Zurbuchen (2011), The global magnetic field of Mercury from MESSENGER orbital observations, *Science, 333*, 1859–1862, doi:10.1126/science.1211001.

Anderson, B. J., Slavin, J. A., Korth, H., Boardsen, S. A., Zurbuchen, T. H., Raines, J. M., Gloeckler, G., McNutt, R. L., Solomon, S. C., 2011. The dayside magnetospheric boundary layer at Mercury, *Planet. Space Sci.*, *59*, 2037-2050.

Anderson, B. J., C. L. Johnson, H. Korth, R. M. Winslow, J. E. Borovsky, M. E. Purucker, J. A. Slavin, S. C. Solomon, M. T. Zuber, and R. L. McNutt Jr. (2012), Low-degree structure in Mercury's planetary magnetic field, *J. Geophys. Res.*, (in press).

Andrews, G. B., T. H. Zurbuchen, B. H. Mauk, H. Malcom, L. A. Fisk, G. Gloeckler, G. C. Ho, J. S. Kelley, P. L. Koehn, T. W. Lefevere, S. S. Livi, R. A. Lundgren, and J. M. Raines (2007), The Energetic Particle and Plasma Spectrometer Instrument on the MESSENGER spacecraft, *Space Sci. Rev., 131*, 523–556, doi:10.1007/s11214-007-9272

Baker, D.N., D. Odstrcil, B.J. Anderson, C.N. Arge, M. Benna, G. Gloeckler, D. Schriver, J.A. Slavin, S.C. Solomon, R.M. Killen, T.H. Zurbuchen (2009), Space environment of Mercury at the time of the first MESSENGER flyby: solar wind and interplanetary magnetic field modeling of upstream conditions, *J. Geophys. Res.*, *114*, A10101, doi:10.1029/2009JA014287.

Baker, D.N., Odstrcil, D., Anderson, B.J., Arge, C.N., Benna, M., Gloeckler, G., Korth, H., Mayer, L.R., Raines, J.M., Schriver, D., Slavin, J.A., Solomon, Trávníček, P.M., Zurbuchen, T.H. (2011), The space environment of Mercury at the times of the second and third MESSENGER flybys. *Planet. Space Sci.*, *59*, 2066-2074, doi:10.1016/J.Pss.2011.01.018.

Baker, D. N., G. Poh, D. Odstrcil, C. N. Arge, M. Benna, C. Johnson, H. Korth, D. J. Gershman, G. C. Ho, W. E. McClintock, T. A. Cassidy, J. M. Raines, D. Schriver, J. A. Slavin, S. C. Solomon, P. M. Trávníček, R. Winslow, and T. H. Zurbuchen (2012),

Solar wind forcing at Mercury: WSA-ENLIL model results, *J. Geophys. Res.,* (in press).

Baumjohan, W., Paschmann, G., 1989. Average plasma properties in the central plasma sheet. *J. Geophys. Res.*, 94, 6597–6606.

Baumjohann, W., Paschmann, G., Sckopke, N, 1988. Average ion moments in the plasma sheet boundary layer. J Geophys. Res. 93, 11507–11520.

Baumjohann, W., A. Matsuoka, K.H. Glassmeier, C.T. Russell, T. Nagai, M. Hoshino, T. Nakagawa, A. Balogh, J.A. Slavin, R. Nakamura, W. Magnes (2006), The magnetosphere of Mercury and its solar wind environment: open issues and scientific questions, *Adv. Space Res.*, *38*, 604–609.

Baumgardner, J., J. Wilson, and M. Mendillo (2008), Imaging the sources and full extent of the sodium tail of the planet Mercury, *Geophys. Res. Lett., 35*, L03201, doi:10.1029/2007GL032337.

Baumgardner, J., and M. Mendillo (2009), The use of small telescopes for spectral imaging of low-light-level extended atmospheres in the Solar System, *Earth Moon Planets*, *105*, 107–113, doi:10.1007/s11038-009-9314-y.

Benna, M., B. J. Anderson, D. N. Baker, S. A. Boardsen, G. Gloeckler, R. E. Gold, G. C. Ho, R. M. Killen, H. Korth, S. M. Krimigis, M. E. Purucker, R. L. McNutt Jr., J. M. Raines, W. E. McClintock, M. Sarantos, J. A. Slavin, S. C. Solomon, and T. H. Zurbuchen (2010), Modeling of the magnetosphere of Mercury at the time of the first MESSENGER flyby, *Icarus, 209*, 3–10, doi:10.1016/j.icarus.2009.11.036.

Bida, T. A., R. M. Killen, and T. H. Morgan (2000), Discovery of calcium in Mercury's atmosphere, *Nature*, *404*(6774), 159-161.

Blewett, D. T., et al. (2011), Hollows on Mercury: MESSENGER Evidence for Geologically Recent Volatile-Related Activity, *Science*, *333*(6051), 1856-1859.

Boardsen, S. A., T. Sundberg, J. A. Slavin, B. J. Anderson, H. Korth, S. C. Solomon, and L. G. Blomberg (2010), Observations of Kelvin-Helmholtz waves along the dusk-side boundary of Mercury's magnetosphere during MESSENGER's third flyby, *Geophys. Res. Lett.*, *37*.

Broadfoot, A. L., S. Kumar, M. J. S. Belton, and M. B. McElroy (1974). Mercury's atmosphere from Mariner 10: Preliminary results, *Science, 185*, 166–169, doi:10.1126/science.185.4146.166.

Burger, M. H., R. M. Killen, W. E. McClintock, R. J. Vervack, A. W. Merkel, A. L. Sprague, and M. Sarantos (2012), Modeling MESSENGER observations of calcium in Mercury's exosphere, *J. Geophys. Res.-Planet*, *117*, E00L11.

Burger, M. H., R. M. Killen, R. J. Vervack, E. T. Bradley, W. E. McClintock, M. Sarantos, M. Benna, and N. Mouawad (2010), Monte Carlo modeling of sodium in Mercury's exosphere during the first two MESSENGER flybys, *Icarus*, *209*(1), 63-74.

Butler, B. J., D. O. Muhleman, and M. A. Slade (1993), Mercury - Full-Disk Radar Images and the Detection and Stability of Ice at the North-Pole, *J. Geophys. Res.-Planet*, *98*(E8), 15003-15023.

Cassidy, T. A., and R. E. Johnson (2005), Monte Carlo model of sputtering and other ejection processes within a regolith, *Icarus*, *176*(2), 499-507.

Chabot, N. L., C. M. Ernst, B. W. Denevi, J. K. Harmon, S. L. Murchie, D. T. Blewett, S. C. Solomon, and E. D. Zhong (2012), Areas of permanent shadow in Mercury's south

polar region ascertained by MESSENGER orbital imaging, *Geophys. Res. Lett.*, *39*, L09204.

Cheng, A. F., R. E. Johnson, S. M. Krimigis, and L. J. Lanzerotti (1987), Magnetosphere, exosphere and surface of Mercury, *Icarus, 71,* 430-440, 1987.

Delcourt, D. C., T. E. Moore, S. Orsini, A. Millilo, and J.-A. Sauvaud (2002), Centrifugal acceleration of ions near Mercury, *Geophys. Res. Lett., 29*, L01591, doi:10.1029/2001GL013829.

Delcourt, D. C., S. Grimald, F. Leblanc, J.-J. Berthelier, A. Millilo, A. Mura, S. Orsini, and T. E. Moore (2003), A quantitative model of the planetary Na^+ contribution to Mercury's magnetosphere, *Annal. Geophys., 21*, 1723–1736, doi:10.5194/angeo-21-1723-2003.

Delcourt, D. C., F. Leblanc, K. Seki, N. Terada, T. E. Moore, and M.-C. Fok (2007), Ion energization during substorms at Mercury, *Planet. Space Sci.*, *55*, 1502-1508.

Delcourt, D. C., K. Seki, N. Terada, and T. E. Moore (2012), Centrifugally stimulated exospheric ion escape at Mercury, *Geophys. Res. Lett.*, *39*.

DiBraccio, G. A., J. A. Slavin, S. A. Boardsen, B. J. Anderson, H. Korth, T. H. Zurbuchen, J. M. Raines, D. N. Baker, R. L. McNutt Jr., and S. C. Solomon (2013), MESSENGER observations of magnetopause structure and dynamics at Mercury, J. *Geophys. Res.-Space Phys.*, *118*, doi:10.1002/jgra.50123.

Domingue, D. L., P. L. Koehn, R. M. Killen, A. L. Sprague, M. Sarantos, A. F. Cheng, E. T. Bradley, and W. E. McClintock (2007), Mercury's atmosphere: A surface-bounded exosphere, *Space Sci. Rev., 131*, 161–186, doi:10.1007/s11214-007-9260-9.

Dungey, J. W. (1961), Interplanetary magnetic field and the auroral zones, *Phys. Rev. Lett., 6*, 47–48, doi:10.1103/PhysRevLett.6.47.

Erickson, G.M. and R.A. Wolf (1980), Is steady convection possible in the Earth's magnetotail?, *Geophys. Res. Lett*., *7*, 897–900.

Evans, L. G., et al. (2012), Major-element abundances on the surface of Mercury: Results from the MESSENGER Gamma-Ray Spectrometer, *J Geophys Res-Planet*, *117*.

Fairfield, H. (1971), Average and Unusual Locations of Earths Magnetopause and Bow Shock, *Journal of Geophysical Research*, 76(28), 6700.

Frank, L. A. (1971), Plasma in the Earth's polar magnetosphere, *J. Geophys. Res.* **76,** 5202.

Fränz, M., D. Harper (2002), Heliospheric coordinate systems, *Planet. Space Sci.*, *50*, 217–233.

Fujimoto, M., W. Baumjohann, K. Kabin, R. Nakamura, J.A. Slavin, N. Terada, L. Zelenyi, (2007), Hermean magnetosphere-solar wind interaction, *Space Sci. Rev.*, *132*, 529–550.

Gershman, D. J., T. H. Zurbuchen, L. A. Fisk, J. A. Gilbert, J. M. Raines, B. J. Anderson, C. W. Smith, H. Korth, and S. C. Solomon (2012), Solar wind alpha particles and heavy ions in the inner heliosphere, *J. Geophys. Res.*, *117*, A00M02, doi:10.1029/2012JA017829.

Goldsten, J. O., et al. (2007), The MESSENGER gamma-ray and neutron spectrometer, *Space Sci. Rev.*, *131*(1-4), 339-391.

Gurnett, D.A., Bhatacharjee, A., 2005. Introduction to Plasma Physics: With Space and Laboratory Applications. Cambridge University Press, Cambridge, 452 pp.

Haerendel, G., G. Paschmann, N. Sckopke, H. Rosenbauer (1978), The frontside boundary layer of the magnetosphere and the problem of reconnection, *J. Geophys. Res.* **83**, 3195.

Harmon, J. K., and M. A. Slade (1992), Radar Mapping of Mercury - Full-Disk Images and Polar Anomalies, *Science*, *258*(5082), 640-643.

Hartle, R. E. and G. E. Thomas (1974), Neutral and ion exosphere models for lunar hydrogen and helium, *J. Geophys. Res., 79*, 1519–1526, doi:10.1029/JA079i010p01519.

Hartle, R. E., S. A. Curtis, and G. E. Thomas (1975), Mercury's helium exosphere, *J. Geophys. Res., 80*, 3689–3692, doi:10.1029/JA080i025p03689.

Hartle**,** R. E., M. Sarantos, and E. C. Sittler Jr. (2011), Pickup ion distributions from three-dimensional neutral exospheres, *J. Geophys. Res., 116*, A10101, doi:10.1029/2011JA016859.

Hauck, S. et al. (2012), in *End of Primary Mission Briefing* by S. C. Solomon and P. D. Bedini.

Hauck, S., J.-L. Margot, S.C. Solomon, R.J. Phillips, C.L. Johnson, F.G. Lemoine, E. Mazarico, T.J. McCoy, S. Padovan, S.J. Peale, M.E. Perry, D.E. Smith, M.T. Zuber (2013), The curious case of Mercury's internal structure, *J. Geophys. Res.*, submitted.

Hawkins, S. E., J. D. Boldt, E. H. Darlington, R. Espiritu, R. E. Gold, B. Gotwols, M. P. Grey, C. D. Hash, J. R. Hayes, S. E. Jaskulek, C. J. Kardian, M. R. Keller, E. R. Malaret, S. L. Murchie, P. K. Murphy, K. Peacock, L. M. Prockter, R. A. Reiter, M. S. Robinson, E. D. Schaefer, R. G. Shelton, R. E. Sterner, H. W. Taylor, T. R. Watters,

and B. D. Williams (2007), The mercury dual imaging system on the MESSENGER spacecraft, *Space Sci. Rev.*, *131*(1-4), 247-338.

Head, J. W., S. L. Murchie, L. M. Prockter, M. S. Robinson, S. C. Solomon, R. G. Strom, C. R. Chapman, T. R. Watters, W. E. McClintock, D. T. Blewett, and J. J. Gillis-Davis (2008), Volcanism on Mercury: Evidence from the first MESSENGER flyby, *Science*, *321*(5885), 69-72.

Head, J. W., C. R. Chapman, R. G. Strom, C. I. Fassett, B. W. Denevi, D. T. Blewett, C. M. Ernst, T. R. Watters, S. C. Solomon, S. L. Murchie, L. M. Prockter, N. L. Chabot, J. J. Gillis-Davis, J. L. Whitten, T. A. Goudge, D. M. H. Baker, D. M. Hurwitz, L. R. Ostrach, Z. Y. Xiao, W. J. Merline, L. Kerber, J. L. Dickson, J. Oberst, P. K. Byrne, C. Klimczak, and L. R. Nittler (2011), Flood Volcanism in the Northern High Latitudes of Mercury Revealed by MESSENGER, *Science*, *333*(6051), 1853-1856.

Hesterberg, D. S. Moore, S. Monaghan, A. Clipson, R. Epstein, B. A. Craig and G. P. McCabe (2010), Bootstrap methods and permutation tests, in *Introduction to the Practice of Statistics*, 7th ed., edited by D. S. Moore, G. P. McCabe and B. A. Craig, W. H. Freeman, New York.

Hesterberg, T. (2011), Bootstrap, *Wiley Interdisciplinary Reviews: Computational Statistics, 3*, 497–526, doi:10.1002/wics.182.

Horwitz, J. L. (1984), Features of Ion Trajectories in the Polar Magnetosphere, *Geophys. Res. Lett.*, *11*(11), 1111-1114.

Horwitz, J. L., and M. Lockwood (1985), The Cleft Ion Fountain - a Two-Dimensional Kinetic-Model, *J Geophys Res-Space*, *90*(Na10), 9749-9762.

Huebner, W. F., J. J. Keady, and S. P. Lyon (1992), Solar Photo Rates for Planetary-Atmospheres and Atmospheric Pollutants, *Astrophys. Space Sci*, *195*(1), 1-&.

Hunten, D. M., T.H. Morgan, D. Shemansky (1988), The Mercury Atmosphere, in *Mercury*, ed. by F. Vilas, C.R. Chapman, M.S. Matthews (Univ. of Arizona Press, Tucson), 562–612.

Ip, W.-H. (1986), The sodium exosphere and magnetosphere of Mercury, *Geophys. Res. Lett., 13*, 423-426.

Kabin, K., T. I. Gombosi, D. L. DeZeeuw, and K. G. Powell (2000), Interaction of Mercury with the solar wind, *Icarus*, *143*(2), 397-406.

Killen, R. M. (2003), Depletion of sulfur on the surface of asteroids and the Moon, *Meteorit. Planet. Sci., 38*, 383–388, doi:10.1111/j.1945-5100.2003.tb00273.x.

Killen, R. M., A. E. Potter, and T. H. Morgan (1990). Spatial distribution of sodium vapor in the atmosphere of Mercury, *Icarus, 85*, 145-167, doi:10.1016/0019-1035(90)90108-L.

Killen, R. M., A. Potter, A. Fitzsimmons, and T. H. Morgan (1999), Sodium D2 line profiles: Clues to the temperature structure of Mercury's exosphere, *Planet. Space Sci., 47*, 1449–1458, doi:10.1016/S0032-0633(99)00071-9.

Killen, R. M., A. E. Potter, P. Reiff, M. Sarantos, B. V. Jackson, P. Hick, and B. Giles (2001), Evidence for space weather at Mercury, *J. Geophys. Res., 106*, 20,509–20,526, doi:10.1029/2000JE001401.

Killen, R. M., M. Sarantos, and P. H. Reiff (2004), Space weather at Mercury, *Adv. Space Res., 33*, 1899–1904, doi:10.1016/j.asr.2003.02.020.

Killen, R. M., T. A. Bida, and T. H. Morgan (2005), The calcium exosphere of Mercury, *Icarus, 173*, 300–311, doi:10.1016/j.icarus.2004.08.022.

Killen, R., G. Cremonese, H. Lammer, S. Orsini, A. E. Potter, A. L. Sprague, P. Wurz, M. L. Khodachenko, H. I. M. Lichtenegger, A. Milillo, and A. Mura (2007), Processes that promote and deplete the exosphere of Mercury, *Space Sci. Rev., 132*, 433–509, doi:10.1007/s11214-007-9232-0.

Killen, R., D. Shemansky, and N. Mouawad (2009), Expected Emission from Mercury's Exospheric Species, and Their Ultraviolet-Visible Signatures (Vol 181, Pg 351, 2009), *Astrophys. J. Suppl. S*, *182*(2), 667-667.

Killen, R. M., A. E. Potter, R. J. Vervack, E. T. Bradley, W. E. McClintock, C. M. Anderson, and M. H. Burger (2010), Observations of metallic species in Mercury's exosphere, *Icarus*, *209*(1), 75-87.

Koehn, P. L. (2002), "The development and testing of the Fast Imaging Plasma Spectrometer and its application in the plasma environment at Mercury", (PhD dissertation, University of Michigan).

Koutroumpa, D., R. Lallement, V. Kharchenko, A. Dalgarno, R. Pepino, V. Izmodenov, and E. Quémerais (2006), Charge-transfer induced EUV and soft X-ray emissions in the heliosphere, *Astron. Astrophys., 460*, 289–300, doi:10.1051/0004-6361:20065250.Lammer, H., P. Wurz, M. R. Patel, R. Killen, C. Kolb, S. Massetti, S. Orsini, and A. Milillo (2003), The variability of Mercury's exosphere by particle and radiation induced surface release processes, *Icarus*, *166*(2), 238-247.

Lammer, H., P. Wurz, M. R. Patel, R. Killen, C. Kolb, S. Massetti, S. Orsini, and A. Milillo (2003), The variability of Mercury's exosphere by particle and radiation induced surface release processes, *Icarus*, *166*(2), 238-247.

Lawrence, D. J., et al. (2013), Evidence for Water Ice Near Mercury's North Pole from MESSENGER Neutron Spectrometer Measurements, *Science*, *339*(6117), 292-296.

Leary, J. C., et al. (2007), The MESSENGER spacecraft, *Space Sci. Rev.*, *131*(1-4), 187-217.

Leblanc, F., and J. Y. Chaufray (2011), Mercury and Moon He exospheres: Analysis and modeling, *Icarus, 216*, 551–559, doi:10.1016/j.icarus.2011.09.028.

Leblanc, F., and R. E. Johnson (2003), Mercury's sodium exosphere, *Icarus*, *164*(2), 261-281.

Leblanc, F., and R. E. Johnson (2010), Mercury exosphere I. Global circulation model of its sodium component*, Icarus, 209*, 280–300, doi:10.1016/j.icarus.2010.04.020.

Leblanc, F., D. Delcourt, and R. E. Johnson (2003), Mercury's sodium exosphere: Magnetospheric ion recycling, *J. Geophys. Res., 108*, 5136-5147, doi:10.1029/2003JE002151.

Lockwood, M., M. O. Chandler, J. L. Horwitz, J. H. Waite, T. E. Moore, and C. R. Chappell (1985), The Cleft Ion Fountain, *J. Geophys. Res.-Space*, *90*(Na10), 9736-9748.

Lukyanov, A. V., O. Umnova, and S. Barabash (2001), Energetic neutral atom imaging of Mercury's magnetosphere, 1. Distribution of neutral particles in an axially symmetrical exosphere, *Planet. Space Sci., 49*, 1669–1675, doi:10.1016/S0032-0633(01)00105-2.

Lukyanov, A., S. Barabash, M. Holmström (2004), Energetic neutral atom imaging at Mercury, *Adv. Space Res.* **33**, 1890.

Madey, T. E., B. V. Yakshinskiy, V. N. Ageev, and R. E. Johnson (1998), Desorption of alkali atoms and ions from oxide surfaces: Relevance to origins of Na and K in atmospheres of Mercury and the Moon, *J. Geophys. Res.-Planet*, *103*(E3), 5873-5887.

Marsch, E., K.-H. Muehlhaeuser, R. Schwenn, H. Rosenbauer, W. Pilipp, F.M. Neubauer (1982), Solar wind protons: three-dimensional velocity distributions and derived plasma parameters measured between 0.3 and 1 AU, *J. Geophys. Res.*, *87*, 52–72.

Massetti, S., S. Orsini, A. Milillo, A. Mura, E. de Angelis, H. Lammer, and P. Wurz (2003), Mapping of the cusp plasma precipitation on the surface of Mercury, *Icarus, 166*, 229–237, doi:10.1016/j.icarus.2003.08.005.

Mazzotta, P., G. Mazzitelli, S. Colafrancesco, and N. Vittorio (1998), Ionization balance for optically thin plasmas: Rate coefficients for all atoms and ions of the elements H to Ni, *Astron. Astrophys. Sup.*, *133*(3), 403-409.

McAdams, J. V., R. W. Farquhar, A. H. Taylor, and B. G. Williams (2007), Messenger Mission Design and Navigation, *Space Sci. Rev.*, *131*(1-4), 219-246.

McClintock, W.E., and M.R. Lankton (2007), The Mercury Atmospheric and Surface Composition Spectrometer for the MESSENGER mission, *Space Sci. Rev.*, *131*, 481–521.

McClintock, W. E., E. T. Bradley, R. J. Vervack, R. M. Killen, A. L. Sprague, N. R. Izenberg, and S. C. Solomon (2008). Mercury's exosphere: Observations during MESSENGER's first Mercury flyby, *Science, 321*, 92–94, doi:10.1126/science.1159467.

McClintock, W. E., R. J. Vervack, E. T. Bradley, R. M. Killen, N. Mouawad, A. L. Sprague, M. H. Burger, S. C. Solomon, and N. R. Izenberg (2009), MESSENGER Observations of Mercury's Exosphere: Detection of Magnesium and Distribution of Constituents, *Science*, *324*(5927), 610-613.

McLain, J. L., A. L. Sprague, G. A. Grieves, D. Schriver, P. Travinicek, and T. M. Orlando (2011), Electron-stimulated desorption of silicates: A potential source for ions in Mercury's space environment, *J. Geophys. Res.-Planet*, *116*.

Milillo, A., P. Wurz, S. Orsini, D. Delcourt, E. Kallio, R. M. Killen, H. Lammer, S. Massetti, A. Mura, S. Barabash, G. Cremonese, I. A. Daglis, E. Angelis, A. M. Lellis, S. Livi, V. Mangano, and K. Torkar (2005), Surface-Exosphere-Magnetosphere System Of Mercury, *Space Sci. Rev.*, *117*, 397-443.

Misawa, H., A. Sonobe, A. Morioka, and S. Okano (2008), Investigation of local time dependence of Mercury's sodium exosphere based on a numerical simulation, *Planet. Space Sci., 56*, 1681-1687, doi:10.1016/j.pss.2008.07.029.

Möbius, E., M. Bzowski, S. Chalov, H. J. Fahr, G. Gloeckler, V. Izmodenov, R. Kallenbach, R. Lallement, D. McMullin, H. Noda, M. Oka, A. Pauluhn, J. Raymond, D. Rucinski, R. Skoug, T. Terasawa, W. Thompson, J. Vallerga, R. von Steiger, and M. Witte (2004), Synopsis of the interstellar He parameters from combined neutral gas, pickup ion and UV scattering observations and related consequences, *Astron. Astrophys.*, *426*(3), 897-907, Doi 10.1051/0004-6361:20035834.

Mukai, T., K. Ogasawara, Y. Saito (2004), An empirical model of the plasma environment around Mercury, *Adv. Space Res.*, *33*, 2166–2171.

Mura, A., S. Orsini, A. Milillo, D. Delcourt, S. Massetti, and E. De Angelis (2005), Dayside H+ circulation at Mercury and neutral particle emission, *Icarus*, *175*(2), 305-319.

Mura, A., A. Milillo, S. Orsini, and S. Massetti (2007), Numerical and analytical model of Mercury's exosphere: Dependence on surface and external conditions, *Planet. Space Sci., 55*, 1569-1583, doi:10.1016/j.pss.2006.11.028.

Ness, N. F., K. W. Behannon, R. P. Lepping, Y. C. Whang, and K. H. Schatten (1974), Magnetic-Field Observations near Mercury - Preliminary Results from Mariner-10, *Science*, *185*(4146), 151-160.

Ness, N. F., K. W. Behannon, R. P. Lepping, and Y. C. Whang (1976), Observations of Mercurys Magnetic-Field, *Icarus*, *28*(4), 479-488.

Neumann, G. A., et al. (2013), Bright and Dark Polar Deposits on Mercury: Evidence for Surface Volatiles, *Science*, *339*(6117), 296-300.

Nittler, L. R., et al. (2011), The Major-Element Composition of Mercury's Surface from MESSENGER X-ray Spectrometry, *Science*, *333*(6051), 1847-1850.

Ogilvie, K. W., J. D. Scudder, R. E. Hartle, G. L. Siscoe, H. S. Bridge, A. J. Lazarus, J. R. Asbridge, S. J. Bame, and C. M. Yeates (1974), Observations at Mercury encounter by the plasma science experiment on Mariner 10, *Science, 185*, 145-151, doi:10.1126/science.185.4146.145.

Ogilvie, K.W., J.D. Scudder, V.M. Vasyliunas, R.E. Hartle, G.L. Siscoe, G.L. (1977), Observations at the planet Mercury by the Plasma Electron Experiment: Mariner 10, *J. Geophys. Res.*, *82*, 1807–1824.

Paige, D. A., M. A. Siegler, J. K. Harmon, G. A. Neumann, E. M. Mazarico, D. E. Smith, M. T. Zuber, E. Harju, M. L. Delitsky, and S. C. Solomon (2013), Thermal Stability of Volatiles in the North Polar Region of Mercury, *Science*, *339*(6117), 300-303.

Potter, A. E. (1995), Chemical Sputtering Could Produce Sodium Vapor and Ice on Mercury, *Geophys. Res. Lett.*, *22*(23), 3289-3292.

Potter, A., and T. Morgan (1985), Discovery of Sodium in the Atmosphere of Mercury, *Science*, *229*(4714), 651-653.

Potter, A. E., and T. H. Morgan (1986), Potassium in the Atmosphere of Mercury, *Icarus*, *67*(2), 336-340.

Potter, A. E., and T. H. Morgan (1990), Evidence for magnetospheric effects on the sodium atmosphere of Mercury, *Science*, *248*, 835–838, doi:10.1126/science.248.4957.835.

Potter, A. E., and T. H. Morgan (1997), Evidence for suprathermal sodium on Mercury, *Adv. Space Res., 19*, 1571–1576, doi:10.1016/S0273-1177(97)00370-0.

Potter, A. E., R. M. Killen, and T. H. Morgan (1999), Rapid changes in the sodium exosphere of Mercury, *Planet. Space Sci., 47*, 1441–1448, doi:10.1016/S0032-0633(99)00070-7.

Potter, A. E., R. M. Killen, and T. H. Morgan (2002), The sodium tail of Mercury, *Meteorit. Planet. Sci., 37*, 1165–1172, doi:10.1111/j.1945-5100.2002.tb00886.x.

Potter, A. E., R. M. Killen, and M. Sarantos (2006), Spatial distribution of sodium on Mercury, *Icarus*, *181*(1), 1-12.

Potter, A. E., R. M. Killen, and T. H. Morgan (2007), Solar radiation acceleration effects on Mercury sodium emission, *Icarus, 186*, 571–580, doi:10.1016/j.icarus.2006.09.025.

Raines, J. M., J. A. Slavin, T. H. Zurbuchen, G. Gloeckler, B. J. Anderson, D. N. Baker, H. Korth, S. M. Krimigis, and R. L. McNutt Jr. (2011), MESSENGER observations of the plasma environment near Mercury, *Planet. Space Sci., 59*, 2004–2015, doi:10.1016/j.pss.2011.02.004.

Raines, J. M., et al. (2013), Distribution and compositional variatios of plasma ions in Mercury's space environment: The first three Mercury years of MESSENGER observations, *J. Geophys. Res.* (in press).

Raj, A., T. Phan, R.P. Lin, V. Angelopoulos (2002), Wind survey of high-speed bulk flow and field-aligned beams in the near-Earth plasma sheet, *J. Geophys. Res.*, *107*, 1419, doi:10.1029/2001JA007547.

Rosenbauer, H., H. Grünwaldt, M.D. Montgomery, G. Paschman, N. Sckopke (1975), Heos 2 plasma observations in the distant polar magnetosphere: the plasma mantle, *J. Geophys. Res.*, *80*, 2723–2737.

Russell, C. H., D. N. Baker, J. A. Slavin (1988), The magnetosphere of Mercury, in *Mercury*, edited by F. Vilas, C. R. Chapman, and M. S. Matthews, pp. 514-561, Univ. of Arizona Press, Tucson, Ariz.

Sarantos, M., P. H. Reiff, T. W. Hill, R. M. Killen, and A. L. Urquhart (2001), A B_x-interconnected magnetosphere model for Mercury, *Planet. Space Sci., 49*, 1629–1635, doi:10.1016/S0032-0633(01)00100-3.

Sarantos, M., R. M. Killen, and D. Kim (2007), Predicting the long-term solar wind ion-sputtering source at Mercury, *Planet. Space Sci., 55*, 1584–1595, doi:10.1016/j.pss.2006.10.011.

Sarantos, M., J. A. Slavin, M. Benna, S. A. Boardsen, R. M. Killen, D. Schriver, and P. Travnicek (2009), Sodium-ion pickup observed above the magnetopause during MESSENGER's first Mercury flyby: Constraints on neutral exospheric models, *Geophys. Res. Lett.*, *36*.

Sarantos, M., R. M. Killen, W. E. McClintock, E. T. Bradley, R. J. Vervack Jr., M. Benna, and J. A. Slavin (2011), Limits to Mercury's magnesium exosphere from MESSENGER second flyby observations, *Planet. Space Sci., 59*, 1992–2003, doi:10.1016/j.pss.2011.05.002.

Schlemm, C. E., et al. (2007), The x-ray spectrometer on the MESSENGER spacecraft, *Space Sci. Rev.*, *131*(1-4), 393-415.

Schmidt, C. A., J. Baumgardner, M. Mendillo, and J. K. Wilson (2012), Escape rates and variability constraints for high-energy sodium sources at Mercury, *J. Geophys. Res., 117*, A03301, doi:10.1029/2011JA017217.

Schriver, D., et al. (2011), Electron transport and precipitation at Mercury during the MESSENGER flybys: Implications for electron-stimulated desorption, *Planet. Space Sci.*, *59*(15), 2026-2036.

Shiokawa, K., W. Baumjohann, G. Haerendel (1997), Braking of high-speed flows in the near-Earth tail, *Geophys. Res. Lett.*, *24*, 1179–1182.

Shue, J. H., J. K. Chao, H. C. Fu, C. T. Russell, P. Song, K. K. Khurana, and H. J. Singer (1997), A new functional form to study the solar wind control of the magnetopause size and shape, *J Geophys Res-Space*, *102*(A5), 9497-9511.

Slade, M. A., B. J. Butler, and D. O. Muhleman (1992), Mercury Radar Imaging - Evidence for Polar Ice, *Science*, *258*(5082), 635-640.

Slavin, J. A. (2004), Mercury's magnetosphere, *Adv. Space Res., 33*, 1859–1874, doi:10.1016/j.asr.2003.02.019.

Slavin, J. A. and R. E. Holzer (1979), The effect of erosion on the solar wind stand-off distance at Mercury, *J. Geophys. Res., 84*, 2076-2082, doi:10.1029/JA084iA05p02076.

Slavin, J. A., S. M. Krimigis, M. H. Acuña, B. J. Anderson, D. N. Baker, P. L. Koehn, H. Korth, S. Livi, B. H. Mauk, S. C. Solomon, and T. H. Zurbuchen (2007), MESSENGER: Exploring Mercury's Magnetosphere, *Space Sci. Rev.*, *131*, 133-160.

Slavin, J.A., M. Acuña, B.J. Anderson, D.N. Baker, M. Benna, G. Gloeckler, R.E. Gold, G.C. Ho, R.M. Killen, H. Korth, S.M. Krimigis, R.L. McNutt Jr., L.R. Nittler, J.M. Raines, D. Schriver, S.C. Solomon, R.D. Starr, P. Trávníček, T.H. Zurbuchen (2008), Mercury's magnetosphere after MESSENGER's first flyby, *Science*, *321*, 85–88.

Slavin, J. A., M. H. Acuña, B. J. Anderson, D. N. Baker, M. Benna, S. A. Boardsen, G. Gloeckler, R. E. Gold, G. C. Ho, H. Korth, S. M. Krimigis, R. L. McNutt, J. M. Raines, M. Sarantos, D. Schriver, S. C. Solomon, P. Travnicek, and T. H. Zurbuchen (2009a), MESSENGER observations of magnetic reconnection in Mercury's magnetosphere, *Science, 324*, 606–610, doi:10.1126/science.1172011.

Slavin, J.A., B.J. Anderson, T.H. Zurbuchen, D.N. Baker, S.M. Krimigis, M. Acuña, M. Benna, S.A. Boardsen, G. Gloeckler, R.E. Gold, G.C. Ho, H. Korth, R.L. McNutt Jr., J.M. Raines, M. Sarantos, D. Schriver, S.C. Solomon, P. Trávníček (2009b), MESSENGER observations of Mercury's magnetosphere during northward IMF, *Geophys. Res. Lett.*, *36*, L02101, doi:10.1029/2008GL036158.

Slavin, J. A., B.J. Anderson, D.N. Baker, M. Benna, S.A. Boardsen, G. Gloeckler, R.E. Gold, G.C. Ho, H. Korth, S.M. Krimigis, R.L. McNutt, Jr, L.R. Nittler, J.M. Raines, M.

Sarantos, D. Schriver, S.C. Solomon, R.D. Starr, P.M. Trávníček, T.H. Zurbuchen (2010), MESSENGER Observations of Extreme Loading and Unloading of Mercury's Magnetic Tail, *Science*, *329*, 665-668.

Slavin, J. A., S. M. Imber, S. A. Boardsen, G. A. DiBraccio, T. Sundberg, M. Sarantos, T. Nieves-Chinchilla, A. Szabo, B. J. Anderson, H. Korth, T. H. Zurbuchen, J. M. Raines, C. L. Johnson, R. M. Winslow, R. M. Killen, R. L. McNutt, and S. C. Solomon (2012), MESSENGER observations of a flux-transfer-event shower at Mercury, *J. Geophys. Res.-Space*, *117*, A00M06, Doi 10.1029/2012ja017926.

Smith, M. F., and M. Lockwood (1996), Earth's magnetospheric cusps, *Rev. Geophys.*, *34*(2), 233-260.

Smyth, W. H., and M. L. Marconi (1995), Theoretical Overview and Modeling of the Sodium and Potassium Atmospheres of the Moon, *Astrophys J*, *443*(1), 371-392.

Snodgrass, H.B. and R.K. Ulrich (1990), Rotation of Doppler features in the solar photosphere, *Astrophys. J.*, *351*, 309–316.

Solomon, S. C., R. L. McNutt Jr., R. E. Gold, and D. L. Domingue (2007), MESSENGER mission overview, *Space Sci. Rev., 131*, 3–39, doi:10.1007/s11214-007-9247-6.

Sprague, A. L. (1992), Mercurys Atmospheric Bright Spots and Potassium Variations - a Possible Cause, *J. Geophys. Res.-Planet*, *97*(E11), 18257-18264.

Sprague, A. L., and T. L. Roush (1998), Comparison of laboratory emission spectra with Mercury telescopic data, *Icarus*, *133*(2), 174-183.

Sprague, A. L., D. M. Hunten, and K. Lodders (1995), Sulfur at Mercury, Elemental at the Poles and Sulfides in the Regolith, *Icarus*, *118*(1), 211-215.

Sprague, A. L., R. W. H. Kozlowski, D. M. Hunten, N. M. Schneider, D. L. Domingue, W. K. Wells, W. Schmitt, and U. Fink (1997), Distribution and abundance of sodium in Mercury's atmosphere, 1985-1988, *Icarus, 129*, 506–527, doi:10.1006/icar.1997.5784.

Sprague, A. L., W. J. Schmitt, and R. E. Hill (1998), Mercury: Sodium atmospheric enhancements, radar-bright spots, and visible surface features, *Icarus, 136*, 60–68, doi:10.1006/icar.1998.6009.

Spreiter, J. R., A. L. Summers, and A. Y. Alksne (1966), Hydromagnetic flow around the magnetosphere, *Planet. Space Sci., 14,* 223–253, doi:10.1016/0032-0633(66)90124-3.

Sundberg, T., S. A. Boardsen, J. A. Slavin, L. G. Blomberg, and H. Korth (2010), The Kelvin-Helmholtz instability at Mercury: An assessment, *Planet. Space Sci.*, *58*(11), 1434-1441.

Sundberg, T., S. A. Boardsen, J. A. Slavin, B. J. Anderson, H. Korth, T. H. Zurbuchen, J. M. Raines, and S. C. Solomon (2012), MESSENGER orbital observations of large-amplitude Kelvin-Helmholtz waves at Mercury's magnetopause, *J. Geophys. Res.-Space*, *117*, (in press).

Sundberg, T., J. A. Slavin, S. A. Boardsen, B. J. Anderson, H. Korth, G. C. Ho, D. Schriver, V. M. Uritsky, T. H. Zurbuchen, J. M. Raines, D. N. Baker, S. M. Krimigis, R. L. McNutt, and S. C. Solomon (2012), MESSENGER observations of dipolarization events in Mercury's magnetotail, *J. Geophys. Res.-Space*, *117*, (in press), doi:10.1029/2012ja017756.

Tracy, P. (2010), Mercury’s Magnetosphere Environment: As Seen by FIPS, private communication.

Vervack, R. J., W. E. McClintock, R. M. Killen, A. L. Sprague, B. J. Anderson, M. H. Burger, E. T. Bradley, N. Mouawad, S. C. Solomon, and N. R. Izenberg (2010), Mercury's Complex Exosphere: Results from MESSENGER's Third Flyby, *Science*, *329*(5992), 672-675.

von Steiger, R., N. A. Schwadron, L. A. Fisk, J. Geiss, G. Gloeckler, S. Hefti, B. Wilken, R. F. Wimmer-Schweingruber, and T. H. Zurbuchen (2000), Composition of quasi-stationary solar wind flows from Ulysses/Solar Wind Ion Composition Spectrometer, *J. Geophys. Res-Space*, *105*(A12), 27217-27238.

Wallace, R. A., W. H. Blume, N. D. Hulkower, and C. L. Yen (1985), Interplanetary Missions for the Late 20th-Century, *J. Spacecraft Rockets*, *22*(3), 316-324.

Wetherill, G. W. (1986), Accumulation of the terrestrial planets and implications concerning lunar origin, in *Origin of the Moon*, eds. W. K. Hartmann, R. J. Phillips, and G. J. Taylor (Houston Lunar and Planetary Inst.), 519-550.

Wilson, J. K., S. M. Smith, J. Baumgardner, and M. Mendillo (1999), Modeling an enhancement of the lunar sodium tail during the Leonid meteor shower of 1998, *Geophys. Res. Lett.*, *26*(12), 1645-1648.

Winslow, R. M., C. L. Johnson, B. J. Anderson, H. Korth, J. A. Slavin, M. E. Purucker, and S. C. Solomon (2012), Observations of Mercury's northern cusp region with MESSENGER's Magnetometer, *Geophys. Res. Lett.*, *39,* (in press).

Wurz, P., J. A. Whitby, U. Rohner, J. A. Martin-Fernandez, H. Lammer, and C. Kolb (2010), Self-consistent modelling of Mercury's exosphere by sputtering, micro-meteorite impact and photon-stimulated desorption, *Planet. Space Sci.*, *58*(12), 1599-1616.

Tarantola, A., 1987, Inverse Problem Theory: Methods for Data Fitting and Model Parameter Estimation, Elsevier, Amsterdam, 630 pp.

Terasawa, T., M. Fujimoto, T. Mukai, I. Shinohara, Y. Saito, T. Yamamoto, S. Machida, S. Kokubun, A.J. Lazarus, J.T. Steinberg, R.P. Lepping (1997), Solar wind control of density and temperature in the near-Earth plasma sheet: WIND/GEOTAIL collaboration, *Geophys. Res. Lett.*, *24*, 935-938.

Trávníček, P.M., P. Hellinger, D. Schriver, D. Herčík, J.A. Slavin, B.J. Anderson (2009), Kinetic instabilities in Mercury's magnetosphere: three-dimensional simulation results, *Geophys. Res. Lett.*, *36*, L07104, doi:10.1029/2008GL036630.

Trávníček, P.M., D. Schriver, P. Hellinger, D. Herčík, B.J. Anderson, M. Sarantos, J.A. Slavin (2010), Mercury's magnetosphere-solar wind interaction for northward and southward interplanetary magnetic field: hybrid simulations results, *Icarus*, *209*, 11–22.

Yakshinskiy, B. V., and T. E. Madey (1999), Photon-stimulated desorption as a substantial source of sodium in the lunar atmosphere, *Nature*, *400*(6745), 642-644.

Yakshinskiy, B. V., T. E. Madey, and V. N. Ageev (2000), Thermal desorption of sodium atoms from thin SiO2 films, *Surf. Rev. Lett.*, *7*(1-2), 75-87.

Yagi, M., K. Seki, Y. Matsumoto, D. C. Delcourt, and F. Leblanc (2010), Formation of a sodium ring in Mercury's magnetosphere, *J. Geophys. Res., 115*, A10253, doi:10.1029/2009JA015226.

Ziegler, J. F. (2004), SRIM-2003, *Nucl. Instrum. Methods Phys. Res. B*, *219*, 1027–1036, doi:10.1016/j.nimb.2004.01.208.

Ziegler, J. F., Ziegler, M. D., and J. P. Biersack (2010), SRIM - The stopping and range of ions in matter (2010), *Nucl. Instrum. Methods Phys. Res. B*, *268*, 1818–1823, doi:10.1016/j.nimb.2010.02.091.

Zurbuchen, T. H., G. Gloeckler, J. C. Cain, S. E. Lasley, and W. Shanks (1998), A low-weight plasma instrument to be used in the inner heliosphere, in *Conference on Missions to the Sun II*, edited by C. M. Korendyke, Proceedings of the Society of Photo-Optical Instrumentation Engineers, vol. 3442, pp. 217–224.

Zurbuchen, T. H., P. Koehn, L. A. Fisk, T. Gombosi, G. Gloeckler, and K. Kabin (2004), On the space environment of Mercury, *Adv. Space Res., 33*, 188–1889, doi:10.1016/j.asr.2003.04.048.

Zurbuchen, T. H., J. M. Raines, G. Gloeckler, S. M. Krimigis, J. A. Slavin, P. L. Koehn, R. M. Killen, A. L. Sprague, R. L. McNutt Jr., and S. C. Solomon (2008), MESSENGER observations of the composition of Mercury's ionized exosphere and plasma environment, *Science, 321*, 90–92, doi:10.1126/science.1159314.

Zurbuchen, T. H., J. M. Raines, J. A. Slavin, D. J. Gershman, J. A. Gilbert, G. Gloeckler, B. J. Anderson, D. N. Baker, H. Korth, S. M. Krimigis, M. Sarantos, D. Schriver, R. L. McNutt Jr., and S. C. Solomon (2011), MESSENGER observations of the spatial distribution of planetary ions near Mercury, *Science, 333*, 1862–1865, doi:10.1126/science.1211302.